Supplement: "An Isolated Mass-gap Black Hole or Neutron Star Detected with Astrometric Microlensing" (2022, ApJL, 933, L23)

Casey Y. Lam[1] , Jessica R. Lu[1] , Andrzej Udalski[2,17] , Ian Bond[3,18], David P. Bennett[4,5,18] , Jan Skowron[2,17] ,
Przemek Mróz[2,17] , Radek Poleski[2,17] , Takahiro Sumi[6,18], Michał K. Szymański[2,17] , Szymon Kozłowski[2,17] ,
Paweł Pietrukowicz[2,17] , Igor Soszyński[2,17] , Krzysztof Ulaczyk[2,7,17] , Łukasz Wyrzykowski[2,17] , Shota Miyazaki[6,18],
Daisuke Suzuki[6,18], Naoki Koshimoto[4,5,8,18], Nicholas J. Rattenbury[9,18] , Matthew W. Hosek, Jr.[10] , Fumio Abe[11,18],
Richard Barry[4,18], Aparna Bhattacharya[4,5,18], Akihiko Fukui[12,13,18], Hirosane Fujii[11,18], Yuki Hirao[6,18], Yoshitaka Itow[11,18],
Rintaro Kirikawa[6,18], Iona Kondo[6,18], Yutaka Matsubara[11,18], Sho Matsumoto[6,18], Yasushi Muraki[11,18], Greg Olmschenk[4,18],
Clément Ranc[14,18] , Arisa Okamura[6], Yuki Satoh[6], Stela Ishitani Silva[4,15,18], Taiga Toda[6,18], Paul J. Tristram[16,18],
Aikaterini Vandorou[4,5,18], Hibiki Yama[6,18], Natasha S. Abrams[1] , Shrihan Agarwal[1] , Sam Rose[1] , and Sean K. Terry[1]

[1] Department of Astronomy, University of California, Berkeley, Berkeley, CA 94720, USA; casey_lam@berkeley.edu
[2] Astronomical Observatory, University of Warsaw, Al. Ujazdowskie 4,00-478 Warszawa, Poland
[3] School of Mathematical and Computational Sciences, Massey University, Private Bag 102-904, North Shore Mail Centre, Auckland 0745, New Zealand
[4] Code 667, NASA Goddard Space Flight Center, Greenbelt, MD 20771, USA
[5] Department of Astronomy, University of Maryland, College Park, MD 20742, USA
[6] Department of Earth and Space Science, Graduate School of Science, Osaka University, Toyonaka, Osaka 560-0043, Japan
[7] Department of Physics, University of Warwick, Gibbet Hill Road, Coventry, CV4 7AL, UK
[8] Department of Astronomy, Graduate School of Science, The University of Tokyo, 7-3-1 Hongo, Bunkyo-ku, Tokyo 113-0033, Japan
[9] Department of Physics, University of Auckland, Private Bag 92019, Auckland, New Zealand
[10] Department of Astronomy, University of California, Los Angeles, Los Angeles, CA 90095, USA
[11] Institute for Space-Earth Environmental Research, Nagoya University, Nagoya 464-8601, Japan
[12] Department of Earth and Planetary Science, Graduate School of Science, The University of Tokyo, 7-3-1 Hongo, Bunkyo-ku, Tokyo 113-0033, Japan
[13] Instituto de Astrofísica de Canarias, Vía Láctea s/n, E-38205 La Laguna, Tenerife, Spain
[14] Zentrum für Astronomie der Universität Heidelberg, Astronomiches Rechen-Institut, Mönchhofstr. 12-14, D-69120 Heidelberg, Germany
[15] Department of Physics, The Catholic University of America, Washington, DC 20064, USA
[16] University of Canterbury Mount John Observatory, P.O. Box 56, Lake Tekapo 8770, New Zealand

Abstract

This supplement provides supporting material for Lam et al. We briefly summarize past gravitational microlensing searches for black holes (BHs) and present details of the observations, analysis, and modeling of five BH candidates observed with both ground-based photometric microlensing surveys and Hubble Space Telescope astrometry and photometry. We present detailed results for four of the five candidates that show no or low probability for the lens to be a BH. In these cases, the lens masses are $<2\,M_\odot$, and two of the four are likely white dwarfs or neutron stars. We also present detailed methods for comparing the full sample of five candidates to theoretical expectations of the number of BHs in the Milky Way ($\sim 10^8$).

1. Supplemental Introduction

This paper is a supplement to Lam et al. (2022), in which we present results from a search for stellar-mass black holes (BHs) in the Milky Way using gravitational microlensing. Lam et al. (2022) and this supplement describe our analysis of five Milky Way BH candidates, which constitute a sufficient sample to place preliminary constraints on the number of isolated BHs in the Milky Way.

This supplement is organized as follows. In Section 2, we present a detailed review of past microlensing searches for BHs. In Section 3, the data sets and reduction processes for our BH search are described, and in Section 4, the photometric and astrometric analysis of the Hubble Space Telescope (HST) data

is explained. In Section 5, the microlensing modeling and fitting procedure are described in detail, while Section 6 describes how to combine the high-resolution imaging and results of the microlensing modeling to constrain the lens's luminosity. Section 7 presents the results of the modeling for the five candidates. Note that results for the single mass-gap BH or neutron star (NS) candidate are presented in the main paper (Lam et al. 2022). Details on constraints on the Milky Way BH population and future BH microlensing searches are discussed in Section 8.

2. Past Microlensing Searches for Black Holes

The advent of ground-based microlensing surveys provided a new avenue to search for isolated BHs. Notable BH candidates identified with photometric microlensing include MACHO-96-BLG-5, MACHO-98-BLG-6 (Bennett et al. 2002), and MACHO-99-BLG-22/OGLE-1999-BUL-32 (Mao et al. 2002). Poindexter et al. (2005) found that MACHO-99-BLG-22 is likely a BH, MACHO-96-BLG-5 is possibly a BH, and MACHO-98-BLG-6 is most likely not a BH, with BH lens

---

[17] OGLE Collaboration.
[18] MOA Collaboration.

Table 1
Target Summary

Short Name	OGLE Alert Name	MOA Alert Name	R.A. (J2000.0)	Decl. (J2000.0)
MB09260	⋯	MOA-2009-BLG-260	17:58:28.561	−26:50:20.88
MB10364	⋯	MOA-2010-BLG-364	17:57:05.401	−34:27:05.01
OB110037	OGLE-2011-BLG-0037	MOA-2011-BLG-039	17:55:55.83	−30:33:39.7
OB110310	OGLE-2011-BLG-0310	MOA-2011-BLG-332	17:51:25.39	−30:24:35.0
OB110462	OGLE-2011-BLG-0462	MOA-2011-BLG-191	17:51:40.19	−29:53:26.3

probabilities of 78%, 37%, and 2%, respectively. On the other hand, Abdurrahman et al. (2021) found that MACHO-96-BLG-5 and MACHO-98-BLG-6 are still good BH candidates, ruling out non-BH lenses for source−lens relative proper motions larger than 2.5 mas yr^{-1}. However, mass estimates for these lensing events cannot be made without invoking a Galactic model. These candidates only had photometric microlensing observations, which alone cannot constrain the mass of the lens, unless rare higher-order effects such as finite-source effects are detected.

As mentioned briefly at the end of Paczynski (1986), microlensing also has an astrometric signature, in which the centroid of the image is displaced from the source's true position (Hog et al. 1995; Miyamoto & Yoshii 1995; Walker 1995). In contrast to the now-routine measurements of photometric microlensing, detections of astrometric microlensing are still at the forefront of our technical capabilities. Typical astrometric shifts toward the Bulge are $O(0.01−1)$ mas, and few existing facilities are currently capable of the astrometric precision to perform this measurement. Only a handful of astrometric measurements of the gravitational deflection of light have ever been made, all for nearby (<10 pc) lenses that were astrometrically anticipated (Eddington 1919; Sahu et al. 2017; Zurlo et al. 2018). However, a combination of photometric and astrometric microlensing together can determine the mass of the lensing object, making detection of astrometric microlensing important for BH searches.

To date, there have been two endeavors to measure lens masses by combining photometric and astrometric microlensing. Lu et al. (2016) attempted a measurement with Keck laser guide star adaptive optics (LGS AO), but no detections of astrometric microlensing were made. Kains et al. (2017) reported a detection of astrometric microlensing made with HST, but the signal was very weak and no lens masses were well constrained. The currently operating Gaia mission is also anticipated to make measurements of astrometric microlensing, which can be searched for once per-epoch astrometry is released (McGill et al. 2020, and references therein). A handful of these deflections should be due to BHs (Rybicki 2018).

3. Observations in Detail

3.1. Targets and Selection Criteria

Five BH candidate microlensing events[19] were selected from the OGLE Early Warning System[20] (Udalski et al. 2015) and MOA Alerts[21] to be imaged with HST. These targets were selected to have long ($t_E > 200$ days) duration, no light contribution from the lens, and high magnifications to allow

detection of parallax signals, making them good isolated BH candidates (Sahu 2009). Preliminary results by Sahu (2017) reported that all five candidates were low-mass (<0.5 $M_\odot$) stars, with no BH detections in the sample. We chose to reanalyze these targets in order to use both BH detections and nondetections in the sample to constrain the total number of BHs in the Milky Way.

Three of the targets, OGLE-2011-BLG-0037/MOA-2011-BLG-039, OGLE-2011-BLG-0310/MOA-2011-BLG-332, and OGLE-2011-BLG-0462/MOA-2011-BLG-191 (hereafter OB110037, OB110310, and OB110462), were alerted by both OGLE and MOA. The other two targets, MOA-2009-BLG-260 and MOA-2010-BLG-364 (hereafter MB09260 and MB10364), were only alerted by MOA. Table 1 lists their coordinates. Figure 1 shows images of the five observed fields, centered on the target. Figure 2 shows the color magnitude diagrams (CMDs) of each field. Figures 3–8 show the light curves of the targets.

3.2. MOA

The MOA-II survey is carried out with a 1.8 m telescope at Mount John University Observatory in New Zealand (Hearnshaw et al. 2006; Sumi 2008). The seeing at the site ranges from ∼1″8 to 3″5, with the median seeing being ∼2″5. The telescope has a 2.2 deg^2 field of view (FOV), with a 10-chip CCD camera with a plate scale of 0″57 pixel^{-1}. The main observations are taken using the MOA-Red (630−1000 nm) filter (Bond et al. 2001).

MOA data for MB09260 and MB10364 were reduced as described in Bond et al. (2017).[22] The MOA light curves are photometrically calibrated to the OGLE-III I- band.

3.3. OGLE

The OGLE-IV survey is carried out at the 1.3 m Warsaw telescope at Las Campanas Observatory in Chile (Udalski et al. 2015). The seeing at the site ranges from ∼1″0 to 2″0, with the median seeing being ∼1″3. The telescope has a 1.4 deg^2 FOV, with a 32-chip CCD camera with a plate scale of 0″26 pixel^{-1}. The main observations are taken using the OGLE I filter, which is similar to Cousins I band. The data were reduced using the Difference Image Analysis technique as implemented by Wozniak (2000). In addition, we rescaled the photometric uncertainties of OB110462 according to the method described in Skowron et al. (2016).

OGLE data are only available for OB110037, OB110310, and OB110462. The magnification of MB09260 was not observed by OGLE, as it occurred during the upgrade from OGLE-III to OGLE-IV. MB10364 is located in a gap in the detectors of the OGLE camera.

---

[19] Three additional targets were initially observed with HST but dropped from the target list after a year (Sahu 2012).
[20] http://ogle.astrouw.edu.pl/ogle4/ews/ews.html
[21] https://www.massey.ac.nz/~iabond/moa/alerts/

[22] OB110037, OB110310, and OB110462 also have MOA light curves. For simplicity we only present the OGLE light-curve fits for those events, since the seeing at OGLE is better.
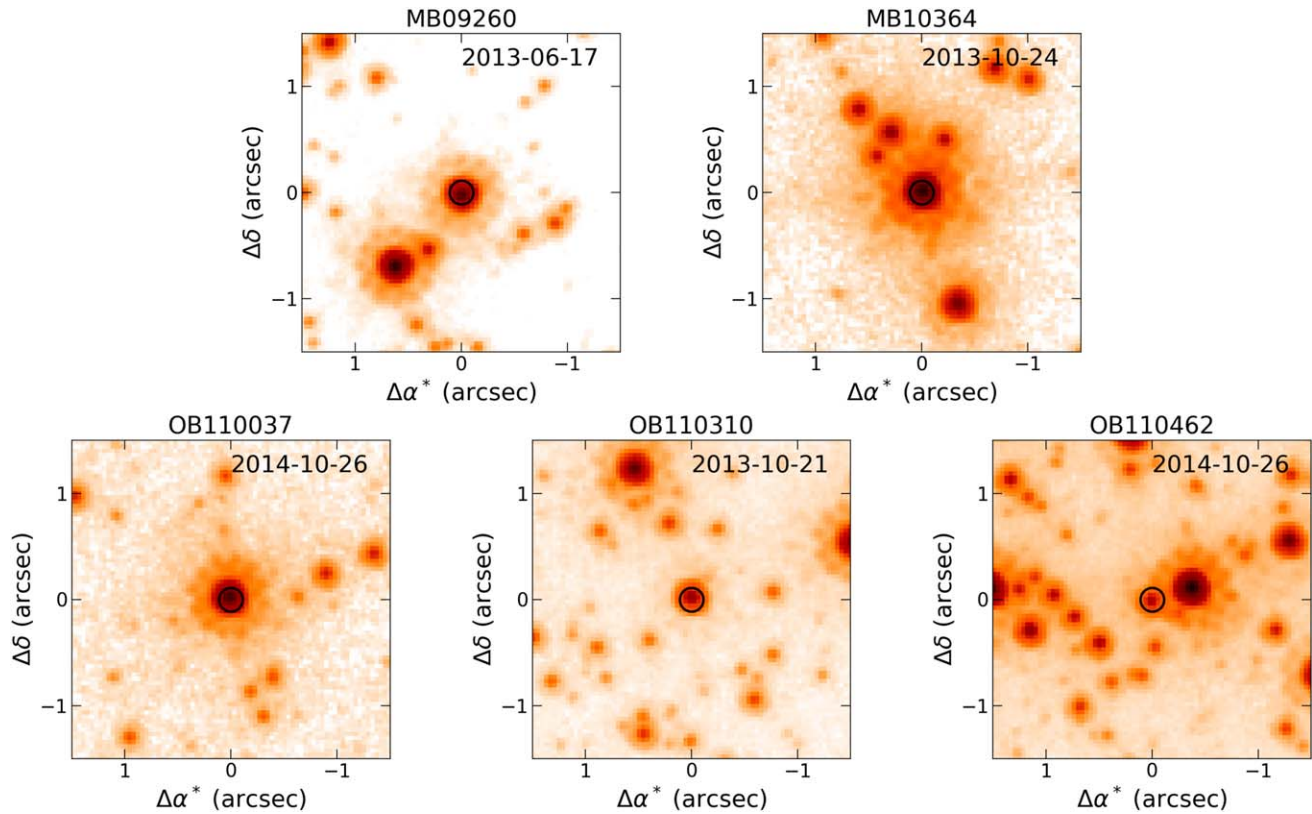
Figure 1. Central $3'' \times 3''$ of HST WFC3-UVIS F814W combined images of the observed fields, centered on the target (circled). These images are of the target at or near baseline, i.e., unmagnified. The color stretch is logarithmic. Note that the color scale is not the same across panels.
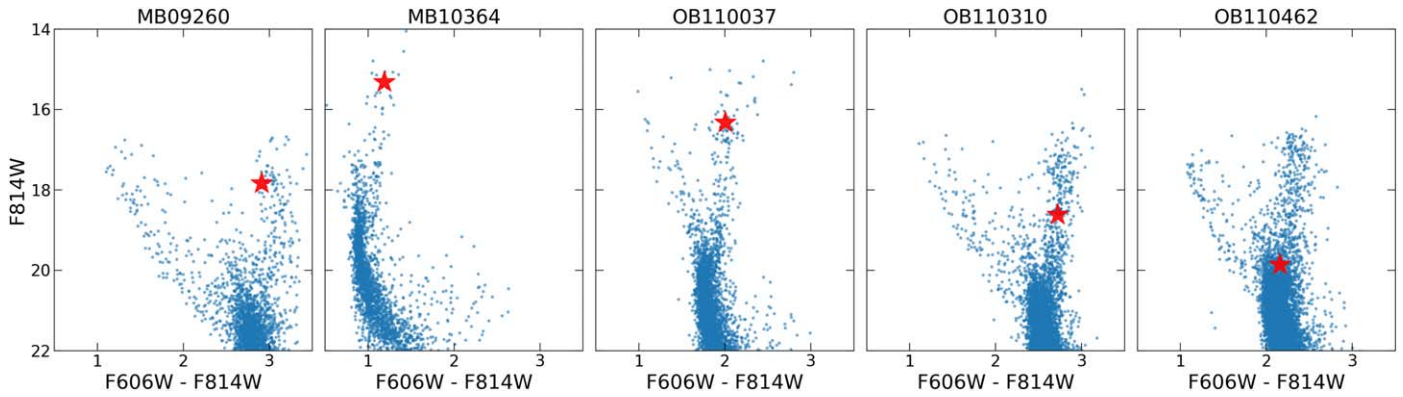
Figure 2. CMDs for each field. The target at baseline magnitude and color is marked as a red star.

3.4. HST

HST observations come from a multiyear campaign following up these five targets (GO-11707, GO-12322, GO-12670, GO-12986, GO-13458, GO-14783; PI: K. C. Sahu). Observations were taken with the UVIS channel on the Wide Field Camera 3 (WFC3) in two different wide-band filters, F606W (V band) and F814W (I band). Table 2 summarizes the HST observations.

The WFC3-UVIS channel is composed of two $2k \times 4k$ CCDs and has a $162'' \times 162''$ FOV with a plate scale of $0\rlap{.}''04\,\mathrm{pixel}^{-1}$. WFC3-UVIS supports subarraying, in which only a portion of the entire detector is read out, which can reduce data volume or exposure time and increase observational efficiency. All observations prior to 2011 July 22 were taken with the UVIS1-2K4-SUB subarray mode. Beginning HST Cycle 18, more subarray sizes

were made available, and observations after 2011 July 22 were taken with the UVIS2-2K2C-SUB subarray mode, a $2k \times 2k$ subarray.

Additional observations of OB110462 commenced in Cycle 29 (GO-16760; PI: C. Lam). These were taken in as similar a configuration as possible to the later epochs of the archival program, using WFC3-UVIS in UVIS2-2K2C-SUB subarraying mode, with observations in F606W and F814W filters. The first set of observations from this program was taken in 2021 October and is presented here; an additional set of observations is anticipated to be taken in the fall of 2022 (Lam & Lu 2021).

3.5. Gaia

Gaia is an all-sky scanning astrometric space mission (Gaia Collaboration et al. 2016). All of the targets, with the
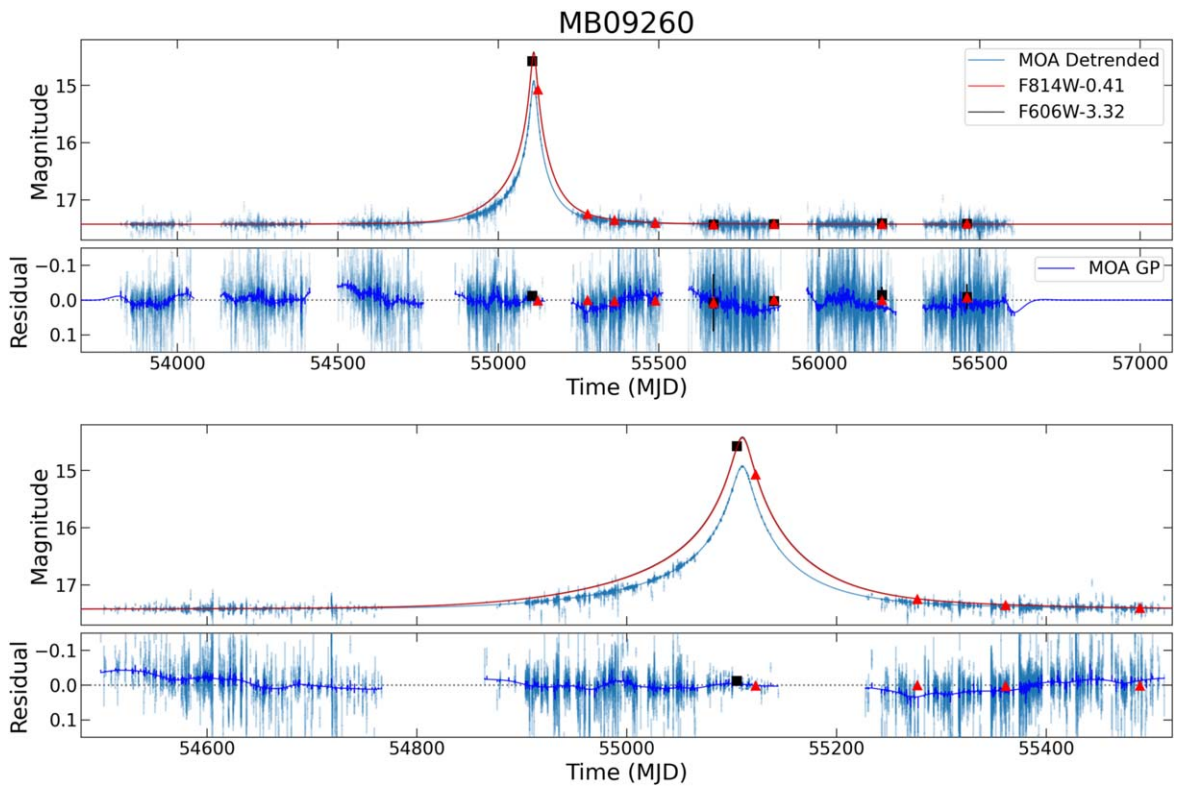
MB09260

Figure 3. Top panel: detrended MB09260 light curve, as seen by MOA and HST F814W and F606W. The MLE model (described in Section 7) is plotted over the data. Second from top panel: the residuals to the MLE model. The Gaussian process (GP) model is plotted on top of the residual. We emphasize that the residual is not independently fit by the GP but is simultaneously fit with the model parameters; this is purely to visualize the data (also see Golovich et al. 2022). See Section 5 for more details about the fitting procedure. Second from bottom panel: same as the top panel, but zoomed in to the three most magnified years. Bottom panel: same as the second from top panel, but zoomed in to the three most magnified years.
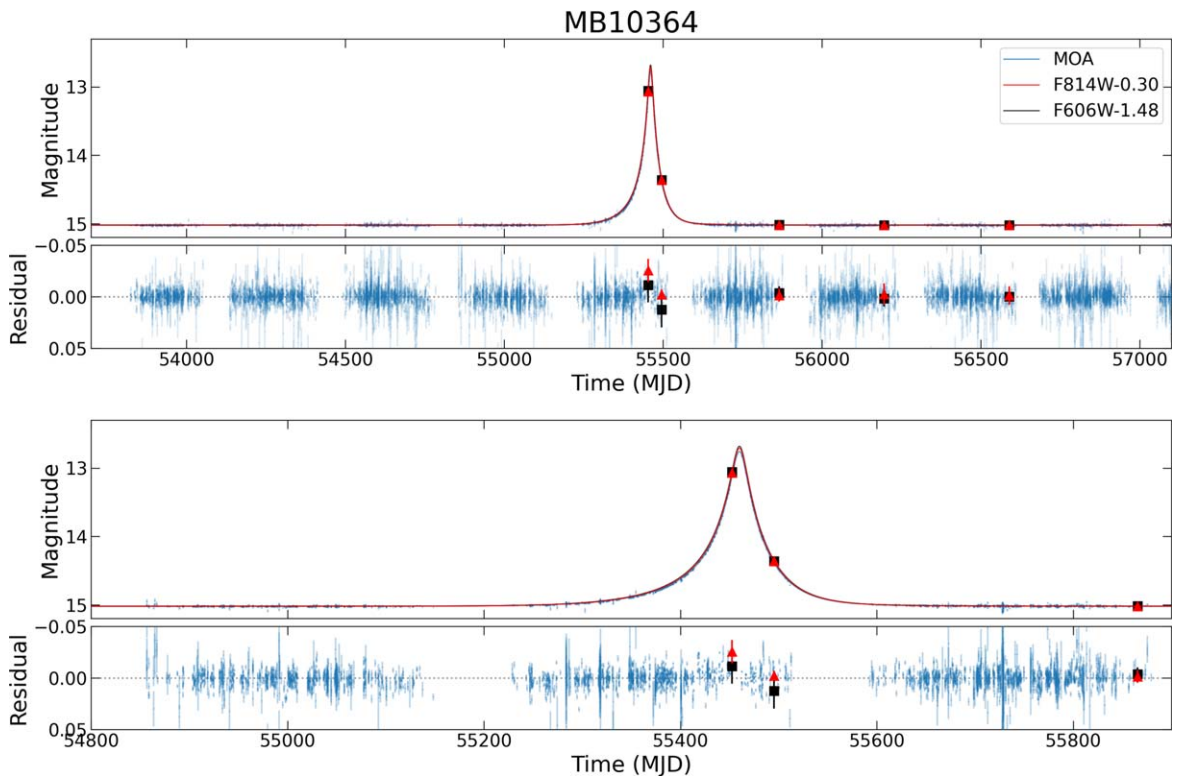
MB10364

Figure 4. Same as Figure 3, but for MB10364. Note that we do not include GP in the MB10364 fit.
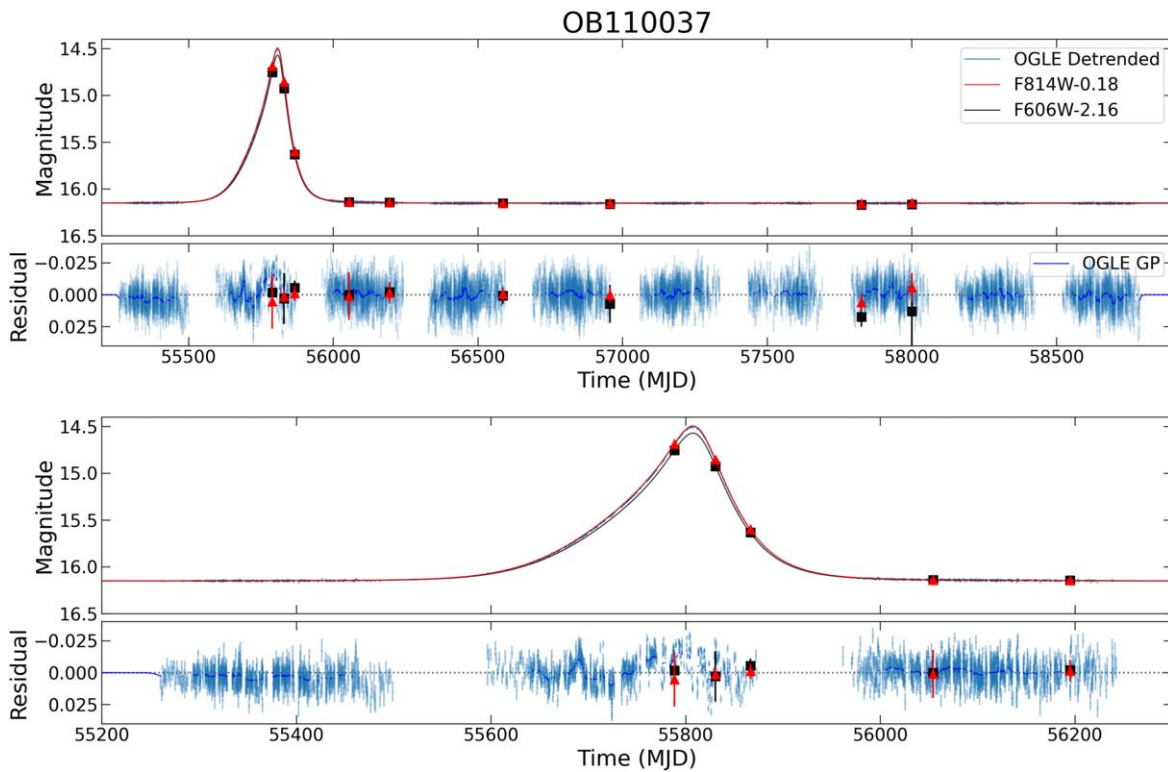
Figure 5. Same as Figure 3, but for OB110037. Instead of MOA data, the blue data are OGLE data.
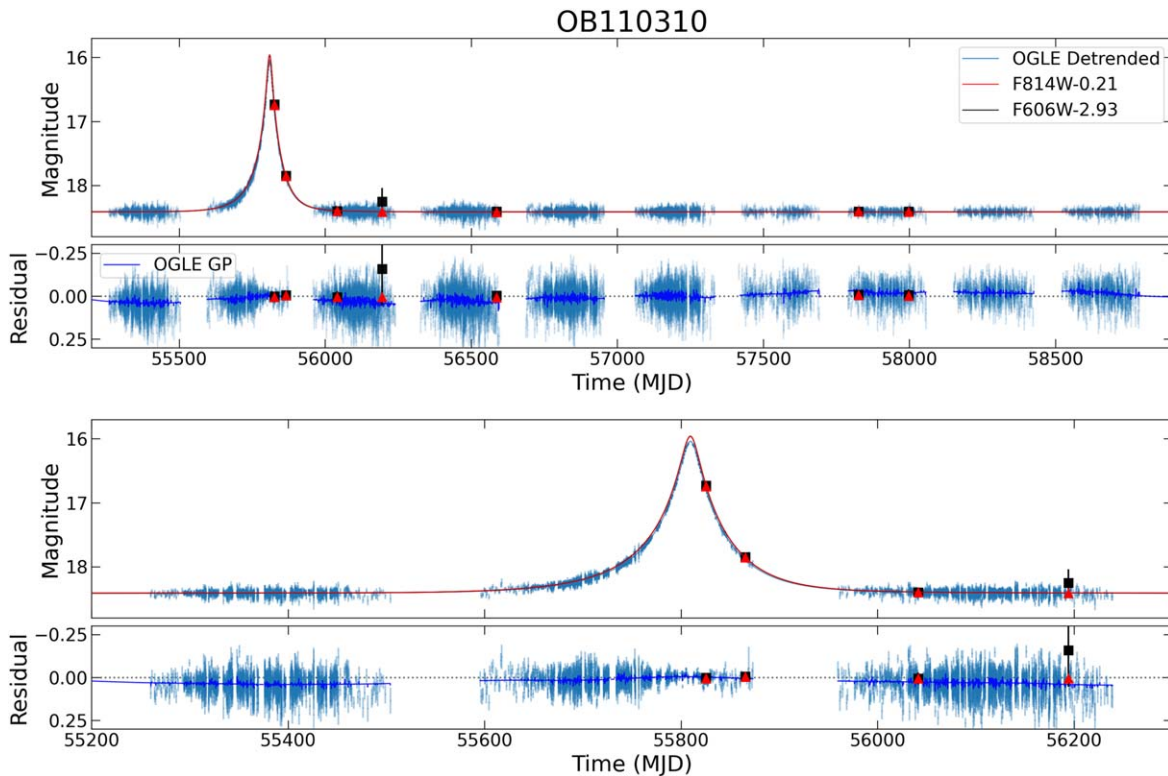
Figure 6. Same as Figure 5, but for OB110310.

exception of OB110462, are found in Gaia Early Data Release 3 (EDR3; Table 3). Gaia EDR3 covers the period from 2014 July 25 to 2017 May 28 (Gaia Collaboration et al. 2021). MB10364, OB110037, and OB110310 have proper motions and parallaxes, while MB09260 does not.

OB110462 was not in Gaia, as it is too faint. We note that there is a Gaia source located $\sim 0\rlap{.}''35$ away from OB110462 (Gaia EDR3 Source ID 4056442477683080960), which coincides with the bright star directly west of the target seen in the HST images (Figure 1).

4. HST Data Analysis

4.1. Reduction

The HST archival data were accessed from the Mikulski Archive for Space Telescopes[23] (MAST) in 2021 June. The Cycle 29 data were accessed in 2021 October. For the following analysis, we employed the calibrated, flat-fielded, individual exposures corrected for charge transfer efficiency (CTE; HST files with suffix `_flc`[24]). The archival data were processed with version 3.6.0 (2020 December 31) of the `calwf3` pipeline, using version 2.0 of the CTE correction algorithm.

CTE can alter astrometry at the milliarcsecond level; hence, it is important to use `_flc` files. However, even the `_flc` files do not necessarily fix all problems associated with CTE (Kuhn & Anderson 2021). Other methods of CTE correction will be explored in future work. At the present we mitigate CTE effects via other methods (Section 4.2.2) and validate our astrometry to ensure that it is not distorted by CTE.

Images were converted into calibrated star lists via the following steps:

1. *Star list extraction from individual frames.* Star lists were extracted from the individual `_flc` exposures by modeling the point-spread functions (PSFs) of sources with `hst1pass`, an updated version of the software described in Anderson & King (2006). Empirical filter-dependent PSF models as described in Anderson (2016) and geometric distortion solutions as described in Bellini et al. (2011) were used when performing source extraction with `hst1pass`.

2. *Combined star list for one epoch.* Within a single epoch and filter, multiple star lists were aligned to a common coordinate system in an iterative manner using `xym2mat` and `xym2bar` (Anderson & King 2006), which include the distortion solution for the WFC3 camera and filters (Bellini et al. 2011) to produce a single matched star list.

3. *Photometric calibration.* Lastly, a zero-point is applied to the star lists to convert from instrumental to Vega magnitudes. Star lists were calibrated against photometrically calibrated star lists on the Hubble Legacy Archive, Data Release 10 (HLA DR10). A magnitude offset is applied later during the astrometric alignment (Section 4.3) to obtain more precise relative photometry.

Note that data taken in F606W and F814W filters are treated as independent measurements. That is, observations taken on the same date are treated as distinct epochs and are not combined into a single star list, as the importance of filter dependence in astrometry is not well established. See Section 4.2.5 and Appendix H for further details.

Certain epochs were excluded from the analysis; these are marked with an asterisk in Table 2. The reason for their exclusion is detailed as follows.

1. *Epochs with only a single frame.* Observations with only a single frame per filter cannot produce any useful photometric or astrometric constraints using `hst1pass`. This is the case for the MB09260 2009 October 1 F814W and 2009 October 19, 2010 March 22, and 2010 June 14

F606W epochs. In the MB09260 2010 October 20 F606W epoch, a cosmic ray in one of the exposures interfered with the extraction of the target, effectively leaving only a single usable frame.

2. *Multiple exposure times.* Although in principle mixing multiple exposure times in a single epoch is possible, in practice most of the data were obtained with several long exposures and only a single frame with a shorter exposure. Rather than analyze the few short frames with different detection thresholds, PSF reference stars, and astrometric reference stars, which can lead to systematic errors, we choose to only use frames with the same exposure times within an epoch. For this reason, some frames from the MB09260 2009 October 1 F606W, MB10364 2010 September 13 F814W, OB110037 2011 August 15 F814W, OB110310 2013 October 21 F814W, and OB110462 2011 August 8 F606W and F814W epochs were not used.

3. *Saturation of target.* No useful astrometric limits can be placed when the target is saturated. The target is saturated in both filters in the MB10364 2011 April 13 and 2011 July 22 epochs.

4. *Telescope-pointing issues.* The observations of OB110462 on 2017 August 11 suffered a telescope drifting issue, resulting in streaked images.

5. *Astrometric alignment systematics.* Although there are no standalone issues with the observations of OB110462 on 2013 May 13, astrometric systematics are apparent in the reference stars when this epoch is astrometrically aligned along with the other epochs using the methodology described in Section 4.2. This is due to the difference in position angle of the observations taken, as the 2013 May 13 epoch was taken at $PA = 99°.9$, while all the other epochs were taken with a PA different by $\sim 180°$, with $PA = 255°.2–276°.1$. Thus, the 2013 May 13 epoch is left out of the analysis. The other targets (MB09260, OB110037, OB110310) with $\sim 180°$ differences in PA across observations do not suffer this same problem, as there are multiple observations at each PA. This allows the systematics due to the $\sim 180°$ PA flip to be calibrated out during the astrometric alignment.

4.2. HST Astrometric Analysis

The positional measurements extracted from the different epochs of HST data (Section 4.1) must be transformed into a common reference frame in order to derive the motion of the target. This is an iterative process, with multiple "passes" at refining the reference frame, allowing for the best relative astrometry possible to be extracted. We follow a similar procedure to that described in Section 4.2 of Lu et al. (2016).

4.2.1. Alignment Procedure

Following standard image processing techniques, a 2D polynomial transformation of the form

$$x' = a_0 + a_1 x + a_2 y + a_3 x^2 + a_4 xy + a_5 y^2 + ... \quad (1)$$

$$y' = b_0 + b_1 x + b_2 y + b_3 x^2 + b_4 xy + b_5 y^2 + ... \quad (2)$$

is applied to the images in order to match them to a reference image. A first-order 2D polynomial transformation
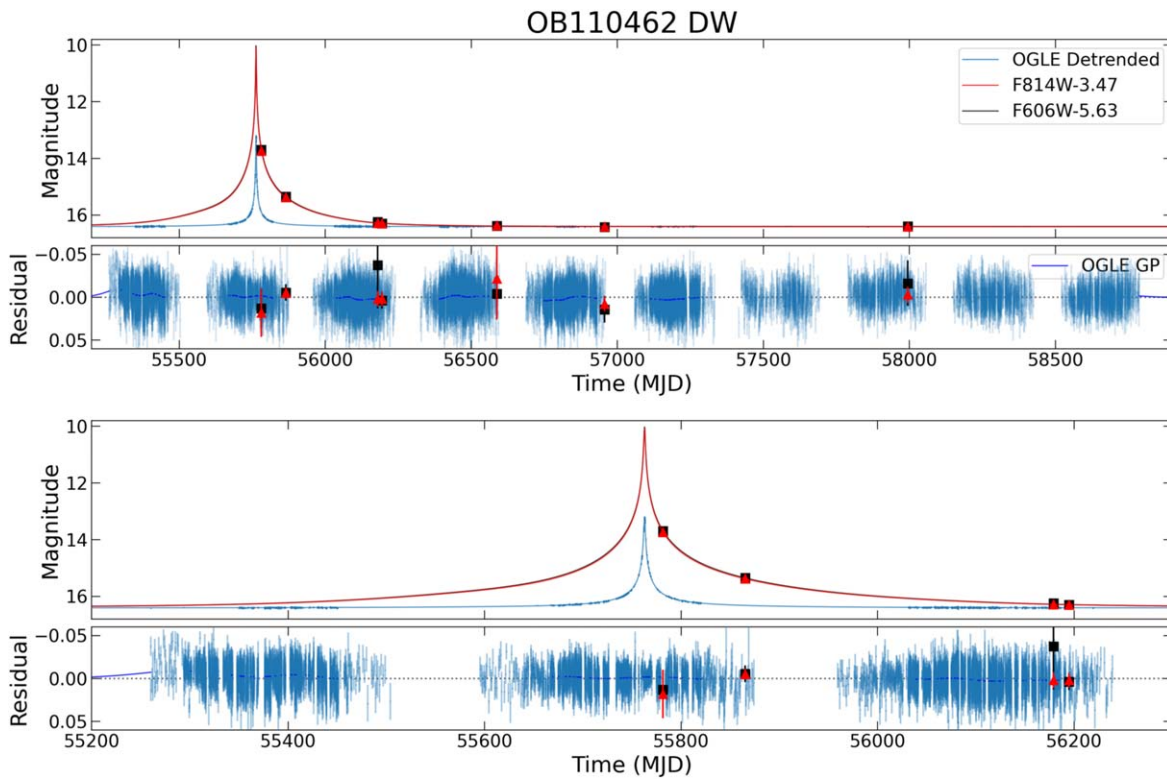

Figure 7. Same as Figure 5, but for OB110462. This MLE model was calculated using the default weighted likelihood described in Section 5.3.
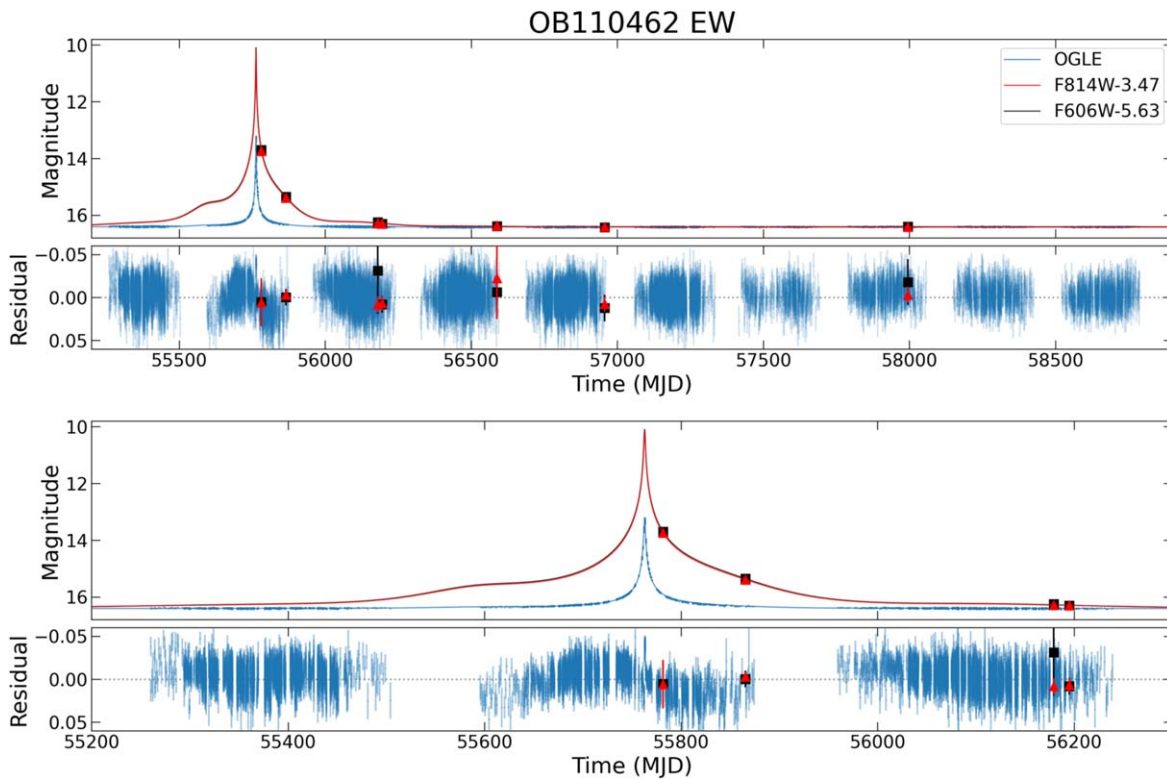

Figure 8. Same as Figure 5, but for OB110462. This MLE model was calculated using the equal weight likelihood described in Section 5.3.

Table 2
HST WFC3-UVIS Observations

Target	Epoch (UT) (yyyy-mm-dd)	PA (deg)	Filter	T_{exp} (s)	N_{im}
MB09260	2009-10-01	275.0	F606W	10.0	4*
				100.0	2
			F814W	20.0	1*
	2009-10-19	275.0	F606W	310.0	1*
			F814W	72.0	6
	2010-03-22	95.0	F606W	300.0	1*
			F814W	280.0	5
	2010-06-14	95.0	F606W	200.0	1*
			F814W	275.0	5
	2010-10-20	270.0	F606W	275.0	2*
			F814W	275.0	4
	2011-04-19	90.0	F606W	275.0	2
			F814W	275.0	4
	2011-10-24	270.0	F606W	275.0	2
			F814W	275.0	4
	2012-09-25	270.0	F606W	275.0	2
			F814W	275.0	4
	2013-06-17	105.5	F606W	275.0	2
			F814W	275.0	4
MB10364	2010-09-13	270.0	F606W	1.0	1
				2.0	1
			F814W	3.0	5
				1.0	1*
	2010-10-26	277.4	F606W	12.0	2
			F814W	12.0	6
	2011-04-13	90.0	F606W	260.0	2*
			F814W	120.0	4*
	2011-07-22	260.5	F606W	160.0	4*
			F814W	90.0	4*
	2011-10-31	278.8	F606W	30.0	5
			F814W	30.0	6
	2012-09-25	270.9	F606W	30.0	5
			F814W	30.0	6
	2013-10-24	277.0	F606W	40.0	5
			F814W	40.0	6
OB110037	2011-08-15	245.0	F606W	30.0	4
			F814W	40.0	4
				20.0	3*
	2011-09-26	270.8	F606W	30.0	5
			F814W	20.0	6
	2011-11-01	276.1	F606W	50.0	5
			F814W	30.0	5
	2012-05-07	98.1	F606W	80.0	4
			F814W	60.0	5
	2012-09-25	270.8	F606W	80.0	4
			F814W	60.0	5
	2013-10-21	274.3	F606W	80.0	4
			F814W	60.0	6
	2014-10-26	275.1	F606W	60.0	4
			F814W	55.0	6
	2017-03-13	90.0	F606W	60.0	3
			F814W	55.0	6
	2017-09-04	256.9	F606W	60.0	3
			F814W	55.0	6
OB110310	2011-09-21	270.0	F606W	75.0	4
			F814W	75.0	5
	2011-10-31	276.5	F606W	280.0	3
			F814W	200.0	4
	2012-04-24	96.0	F606W	280.0	3
			F814W	230.0	4
	2012-09-24	271.3	F606W	280.0	3
			F814W	230.0	4

Table 2
(Continued)

Target	Epoch (UT) (yyyy-mm-dd)	PA (deg)	Filter	T_{exp} (s)	N_{im}
	2013-10-21	274.8	F606W	280.0	3
			F814W	68.0	1*
				230.0	4
	2017-03-14	90.4	F606W	270.0	3
			F814W	230.0	4
	2017-09-01	268.4	F606W	270.0	3
			F814W	230.0	4
OB110462	2011-08-08	270.0	F606W	60.0	1*
				75.0	3
			F814W	120.0	1*
				60.0	1*
				75.0	3
	2011-10-31	276.1	F606W	280.0	3
			F814W	200.0	4
	2012-09-09	269.5	F606W	290.0	3
			F814W	190.0	4
	2012-09-25	271.3	F606W	280.0	3
			F814W	200.0	4
	2013-05-13	99.9	F606W	280.0	3*
			F814W	200.0	4*
	2013-10-22	274.6	F606W	285.0	3
			F814W	285.0	4
	2014-10-26	275.2	F606W	265.0	3
			F814W	265.0	4
	2017-08-11	255.2	F606W	250.0	3*
			F814W	250.0	4*
	2017-08-29	268.3	F606W	250.0	3
			F814W	250.0	4
	2021-10-01	272.0	F606W	407.0	5
			F814W	307.0	6

Note. An asterisk indicates observations excluded from analysis.

($x' = a_0 + a_1 x + a_2 y$; $y' = b_0 + b_1 x + b_2 y$) is an affine transformation,[25] which can be used to model translation, rotation, scaling, and shearing introduced by the camera. A higher-order polynomial can correct for additional distortions, but going beyond second order generally does not improve results, as the number of free parameters quickly increases and results in overfitting.

In the first pass, the HST images are aligned to the absolute reference frame of Gaia with a first-order 2D polynomial transformation to roughly establish the transformation. The Gaia EDR3 catalog is matched to the HST catalog using the pattern matching algorithm of Groth (1986).

In subsequent passes, the HST images are aligned to themselves, using a 2D polynomial transformation going up to second order. It is empirically determined that making three to four passes gives optimal results. In each successive pass, the HST images are aligned to the reference frame derived in the previous pass, which continually refines the reference frame and derived proper motions.

To calculate the optimal transformation, a set of reference stars $r_{ref}^R(t_0)$ are selected from the stars in reference frame $R(t_0)$ observed at time t_0. The reference stars $r_{ref}^R(t_0)$ are

---

[25] An affine transformation maps points to points, lines to lines, planes to planes, and so on. Affine transformations preserve collinearity and ratios of distances. Parallel lines also remain parallel after an affine transformation.

Table 3
Gaia EDR3 Values

Parameter	MB09260	MB10364	OB110037	OB110310
Source ID	4064007633015639552	4042290560398692096	4056117808133831936	4056344036933003264
R.A. (deg)	$269.619073405 \pm 7.3e{-}07$	$269.272538687 \pm 1.9e{-}08$	$268.982636391 \pm 3.0e{-}08$	$267.855757518 \pm 2.3e{-}07$
Decl. (deg)	$-26.839323825 \pm 5.9e{-}07$	$-34.451415987 \pm 1.5e{-}08$	$-30.561059419 \pm 2.5e{-}08$	$-30.409776355 \pm 1.7e{-}07$
$\mu_{\alpha*}$ (mas yr^{-1})	⋯	-7.43 ± 0.08	2.40 ± 0.13	-2.08 ± 1.12
μ_{δ} (mas yr^{-1})	⋯	-6.80 ± 0.05	-3.91 ± 0.09	-6.75 ± 0.58
π (mas)	⋯	0.40 ± 0.08	0.15 ± 0.13	0.54 ± 1.16
ZP-corrected π (mas)	⋯	0.43	0.19	0.53*
G (mag)	19.216 ± 0.004	16.086 ± 0.002	17.477 ± 0.001	20.051 ± 0.010
RP (mag)	⋯	14.929 ± 0.009	16.323 ± 0.010	⋯
BP (mag)	⋯	16.557 ± 0.011	19.049 ± 0.032	⋯
ipd_gof_harmonic_amplitude	0.089	0.064	0.036	0.042
ipd_frac_multi_peak	0	15	0	0
ipd_frac_odd_win	18	0	0	55
ruwe	⋯	1.388	0.971	0.981
astrometric_excess_noise (mas)	1.241	0.406	0.000	0.894
astrometric_excess_noise_sig	2.657	12.020	0.000	0.332
astrometric_params_solved	3	95	31	95
phot_bp_rp_excess_factor	⋯	1.69	1.39	⋯

Note. Magnitude uncertainties are estimated from the Gaia reported flux errors. Zero-point (ZP) correction comes from Lindegren et al. (2021a); an asterisk indicates values that are extrapolations. For full descriptions we refer the reader to Gaia EDR3 documentation (van Leeuwen et al. 2021), Section 13.1.1 gaia_source. OB110462 is not in Gaia.

matched to corresponding stars $u_{\mathrm{ref}}^U(t)$ in the untransformed $U(t)$ frame observed at time t. The transformation $T: U(t) \rightarrow R(t)$ is found by least-squares minimization of the x and y position residuals from the alignment

$$x_{\mathrm{res}} = \sum_i w_{x,i}(x_{r,i}^R(t) - T(x_{u,i}^U(t)))^2 \qquad (3)$$

$$y_{\mathrm{res}} = \sum_i w_{y,i}(y_{r,i}^R(t) - T(y_{u,i}^U(t)))^2, \qquad (4)$$

where $w_{(x,y),i}$ is the weight for the ith reference star and $(x^R(t)_{r,i}, y^R(t)_{r,i})$ and $(x_{u,i}^U(t), y_{u,i}^U(t))$ are the positions of the stars in the reference $R(t)$ and untransformed $U(t)$ frames at time t. The positions of the reference stars $r_{\mathrm{ref}}^R(t)$ in the reference frame R at time t are propagated from time t_0 using the proper motions

$$x_{r,i}^R(t) = x_{r,i}^R(t_0) + v_{x,r,i}^R(t - t_0) \qquad (5)$$

$$y_{r,i}^R(t) = y_{r,i}^R(t_0) + v_{y,r,i}^R(t - t_0), \qquad (6)$$

where $v_{(x,y),r,i}^R$ are the proper motions of the ith reference stars in reference frame R. After the transformation T is derived, it is applied to all the stars u^U in the U frame to obtain a transformed star list $u^R(t) = T(u^U(t))$, where the stars $u^R(t)$ are now in the frame R. This yields star lists for all N epochs $u_1^R(t_1),...,u_N^R(t_N)$, where the positions of all the stars are now in the same reference frame R. For each star j, a proper motion is derived by finding the best-fit straight line via nonlinear least squares through the $n \leqslant N$ observations.[26]

Lu et al. (2016) examined several different weighting schemes and showed that the resulting astrometry is not affected. We choose to use weights $w_{(x,y),i} = 1/\sigma_{(x,y),i}$, where $\sigma_{(x,y),i}$ are the positional uncertainties of the stars in the

untransformed frame. For the positional uncertainties, instead of using the rms values σ_{RMS} directly returned by hst1pass, we follow Hosek et al. (2015) and use the error on the mean $\sigma_{\mathrm{rms}}/\sqrt{N}$, where N is the number of frames the source is detected in, with an additional empirical additive error. The uncertainties, as well as the procedure used to determine them, are detailed in Appendix A. The additive error term dominates over the $\sigma_{\mathrm{rms}}/\sqrt{N}$ term for bright stars, which makes the positional errors more uniform across epochs and magnitude as would be expected for systematic errors.

As we are interested in the astrometry of the target, the target itself is not used to establish the transformation into a common reference frame (Section 4.2.2) or to judge the quality of the final transformation (Figure 9).

4.2.2. Reference Star Selection

Reference stars are stars assumed to have linear proper motions, which are used to derive the reference frame transformation and the motions of the other stars. The selection of reference stars depends on multiple considerations, such as the stellar density, amount of geometric distortion, instrumental systematics, and number and brightness of targets of interest, to name a few. The goal is to balance having enough stars to establish the reference frame, while excluding stars that would produce a nonstable reference frame. The criteria for reference star selection for each target are summarized in Table 4. We choose reference stars with brightness similar to the target, and relatively large radial separations from our target of interest, and we exclude likely foreground stars. The target itself is also excluded from being a reference star. We detail the reasoning for these choices below.

Brightness range: Due to the nature of CTE, there are strong magnitude-dependent astrometric residuals, even when using the latest CTE-corrected _flc images. However, this is not unexpected (Kuhn & Anderson 2021). For this reason, stars

---

[26] Some stars are not detected in all epochs, which is why it is possible to have $n < N$ observations.
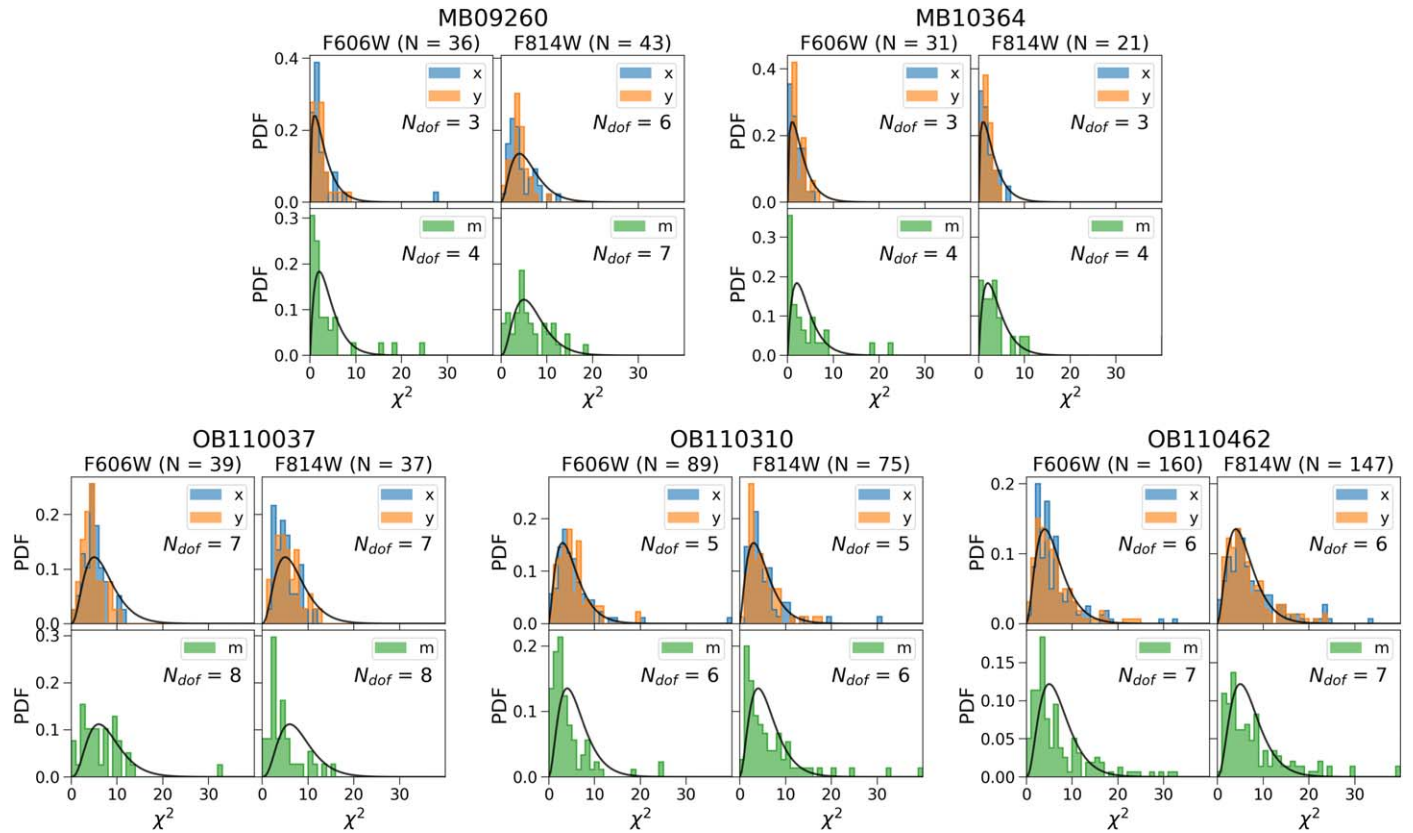
Figure 9. Histogram of χ^2 residual values to the linear fits with no parallax for the reference stars of each target (Table 4). In each panel, the left column shows the distributions for reference stars in F606W, while the right column shows F814W. The number of reference stars is listed as *N*. In each panel, the top row shows the χ^2 distribution of residuals of a linear fit to positions vs. time in $x \equiv$ R.A. and $y \equiv$ decl. The bottom row shows the χ^2 distribution of residuals of a constant fit to magnitude vs. time. The expected χ^2 distributions are shown in black, with the number of degrees of freedom listed as $N_{\rm dof}$.

are chosen to be in a brightness range similar to the one spanned by the target as narrow as possible. For OB110310 and OB110462, which are relatively faint and where there are many stars of similar brightness, all stars falling within ± 0.1 mag of the target's brightest and faintest in the HST data are used. MB09260, on the other hand, is brighter, with less stars of similar brightness, so the range is larger, with all stars falling within ± 1 mag of the target's brightest and faintest in the HST data being used. MB10364 is so bright that many stars of comparable brightness are saturated in the longer exposures. Because of this, only bright (F814W < 18.0, F606W < 19.2) and unsaturated stars were selected; the bright limit on the magnitude range differs between epochs because of the different exposure times.

Spatial separation: Only reference stars within $30''$, or $20''$ for the denser field around OB110462, are used as reference stars. This minimizes the impact of geometric distortion residuals and spatially dependent PSF variations.

Foreground stars: A key assumption in the astrometric alignment process is that reference stars have linear proper motions, and parallax effects are ignored. For a typical bulge star 8 kpc from Earth, this is a reasonable assumption, as the parallax will be $1/8000'' = 0.125$ mas, below our achievable astrometric precision. However, for nearby stars, ignoring parallax is an issue when trying to derive an accurate transformation. As all the target fields are toward the highly extincted Galactic bulge, bright blue stars as identified on a CMD (Figure 2) are likely to be nearby and have a nonnegligible parallax, and they are excluded from the set of

reference stars. The color–magnitude exclusion criteria are listed in the last column of Table 4. For MB10364, no bright blue stars were removed as reference stars, as all the observations came from within 6 weeks of the same time of year. Hence, any type of yearly parallax signal would be negligible within this time span.

Number of detections: We require reference stars to be detected in most, if not all, epochs. If there are $N_{\rm ep}$ total epochs, we require reference stars to be detected in $N_{\rm ep,detect} = N_{\rm ep} - 2$ epochs. Lastly, as the motion of the target is the quantity we are interested in, we do not use it as a reference star.

4.2.3. Derived Stellar Proper Motions

To evaluate the goodness of the fits of the derived stellar proper motions, we consider the χ^2 distributions of the position residuals

$$\chi^2_x = \sum_t \left(\frac{x_t - x_{t,\rm fit}}{\sigma_{x_t}} \right)^2 \qquad (7)$$

$$\chi^2_y = \sum_t \left(\frac{y_t - y_{t,\rm fit}}{\sigma_{y_t}} \right)^2, \qquad (8)$$

where $x \equiv$ R.A., $y \equiv$ decl., $(x, y)_t$ are the positions in the data, $(x, y)_{t,\rm fit}$ are the positions as derived from the linear motion fit, and $\sigma_{(x,y),t}$ are the positional uncertainties at time *t*. The distributions of χ^2_x and χ^2_y for the reference stars detected in all epochs $N_{\rm ep}$ are shown in Figure 9, with the expected χ^2

Table 4
Reference Star Criteria

Target	Magnitude Range	Radius	$N_{\mathrm{ep,detect}}$	Excluded Bright Blue Stars
MB09260	Target range ±1 mag: 14.5 < F814W < 18.8 16.9 < F606W < 21.7	30″	11	F606W–F814W < 2.6 & F814W < 20.6
MB10364	2010-09-13: 12.5 < F814W < 18.0 11.5 < F606W < 19.2 2010-10-26: 15.1 < F814W < 18.0 13.4 < F606W < 19.2 2011-10-31: 15.8 < F814W < 18.0 14.4 < F606W < 19.2 2012-09-25: 16.0 < F814W < 18.0 14.5 < F606W < 19.2 2013-10-24: 16.1 < F814W < 18.0 14.7 < F606W < 19.2	30″	8	None excluded
OB110037	Target range ±0.5 mag: 14.4 < F814W < 16.9 16.4 < F814W < 18.8	30″	12	F606W–F814W < 1.75 & F814W < 19.6
OB110310	Target range ±0.1 mag: 16.9 < F814W < 18.7 19.6 < F606W < 21.4	30″	12	F606W–F814W < 2.4 & F814W < 21.0
OB110462	Target range ±0.1 mag: 17.1 < F814W < 20.0 19.2 < F606W < 22.1	20″	14	F606W–F814W < 1.9 & F814W < 20.6

Note. These are the criteria for the last pass.

distribution overplotted on top. The distributions for the positions in F814W and F606W are shown separately. The expected residual distribution has N_{ep} −2 degrees of freedom, as there are two free parameters in the linear motion fit (initial position and proper motion). Note that, unlike Gaia, this linear model fit does not include parallax. Parallax is only included when modeling the microlensing event.

4.2.4. OB110462 Bias Correction

There is a bright star ("the neighbor") ∼10 pixels (∼0″.4) west of OB110462. The neighbor is ∼3 mag brighter than OB110462 at baseline (F814W = 16.7 mag, F606W = 19.0 mag). Because of its proximity and high contrast, the neighbor's PSF might "leak" onto OB110462 and alter its astrometry and photometry. We perform injection and recovery tests to ascertain the reliability of faint source extraction near a bright source, in order to determine whether the astrometry and photometry of OB110462 as determined in Sections 4.2 and 4.3 is biased by the bright neighbor.

The methodology and results of the injection and recovery analysis are detailed in Appendix B. In summary, the positional bias is negligible when the target is highly magnified and of similar brightness to the neighbor. However, in epochs where the target is no longer magnified, the bright star biases the position of the target. In F814W, where the resolution is lower, the measured position of the target is biased toward the neighbor by ∼0.4 mas along the target–neighbor separation vector. In F606W, where the resolution is higher, the bias is

less (∼0.25 mas), with the direction of bias more randomly oriented. Similarly, the photometric bias is larger when the contrast is large, with the bright neighbor causing the extracted photometry of OB110462 to be brighter than the injected values. The effect is again more severe in F814W than in F606W because of the lower resolution.

Using the results of the injection and recovery analysis, we calculate a bias correction to apply to OB110462 astrometry and photometry (Table 16). The values in the table are added to astrometry and photometry derived in Sections 4.2 and 4.3; the uncertainties are added in quadrature to the uncertainties in Sections 4.2 and 4.3.

We only perform this analysis for OB110462, as it is the only faint target near a bright companion. All the other targets are either bright with faint companions, isolated, or both bright and isolated.

4.2.5. Astrometric Color Offset

As mentioned in Section 4.1, the data taken in F606W and F814W filters are treated as independent measurements. For OB110037 and OB110462, the astrometric measurements in F606W and F814W do not agree within the uncertainties.

For OB110037, although the 2011 and 2012 epochs show good agreement, the 2013–2017 epochs become increasingly discrepant as time goes on. We attribute this difference to binarity (Section 7.4).

In contrast, for OB110462 the astrometry in the F606W and F814W are discrepant in all data sets, but the difference appears

Table 5
Gaia vs. HST Proper Motions

Target	$\mu_{\mathrm{HST},L}$ (mas yr^{-1})	$\mu_{\mathrm{HST},S}$ (mas yr^{-1})	μ_{Gaia} (mas yr^{-1})
MB10364	$(-5.11^{+1.62}_{-1.10}, -7.78^{+0.58}_{-0.89})$	$(-7.56^{+0.12}_{-0.12}, -6.49^{+0.11}_{-0.11})$	$(-7.43 \pm 0.08, -6.80 \pm 0.05)$
OB110037	$(6.27^{+1.27}_{-1.20}, -6.56^{+0.77}_{-0.81})$	$(2.19^{+0.24}_{-0.24}, -3.87^{+0.20}_{-0.20})$	$(2.40 \pm 0.13, -3.91 \pm 0.09)$
OB110310	$(-0.02^{+1.93}_{-1.16}, -4.68^{+2.39}_{-2.13})$	$(-2.41^{+0.12}_{-0.12}, -7.26^{+0.08}_{-0.08})$	$(-2.08 \pm 1.12, -6.75 \pm 0.58)$

Note. The source and lens proper motions here have been transformed into the absolute Gaia proper-motion frame, which is offset to the HST proper-motion frame as described in Appendix C. The uncertainties on μ_L and μ_S also reflect the uncertainty in the Gaia to HST proper-motion transformation; the standard error on the mean of that transformation was added in quadrature to the uncertainties from the proper-motion fits. For this reason, the uncertainties for μ_L and μ_S in this table do not match those in Tables 10–12.

to be a relatively constant offset with time. This is true both before and after applying the bias correction in Section 4.2.4. Because the nature of the color difference appears to be a constant offset, we apply a constant shift to the OB110462 F606W astrometry

$$\Delta_x = \frac{\sum_t w_{x,t}(x_{\mathrm{F814W},t} - x_{\mathrm{F606W},t})}{\sum_t w_{x,t}} \qquad (9)$$

$$\Delta_y = \frac{\sum_t w_{y,t}(y_{\mathrm{F814W},t} - y_{\mathrm{F606W},t})}{\sum_t w_{y,t}}, \qquad (10)$$

where

$$w_{x,t} = (\sigma^2_{x,\mathrm{F814W},t} + \sigma^2_{x,\mathrm{F606W},t})^{-1/2} \qquad (11)$$

$$w_{y,t} = (\sigma^2_{y,\mathrm{F814W},t} + \sigma^2_{y,\mathrm{F606W},t})^{-1/2}. \qquad (12)$$

and t indexes the observation times. Thus, the modified astrometry for F606W is

$$x_{\mathrm{F606W},t'} = x_{\mathrm{F606W},t} + \Delta_x \qquad (13)$$

$$y_{\mathrm{F606W},t'} = y_{\mathrm{F606W},t} + \Delta_y. \qquad (14)$$

The values of the offset are $\Delta_x = -0.57$ mas and $\Delta_y = 0.39$ mas. Note that these offsets are calculated using the bias-corrected astrometry.[27] See Appendix H for further details and justification.

We also investigate stars nearby to determine whether any of them show similar behavior. For the 70 stars within 3″ of OB110462, we calculate the average positional offset between F814W and F606W in R.A. and decl. using Equations (9) and (10). We then search for stars where the average positional uncertainty in F814W and F606W (whichever is larger) is smaller than the average positional offset to determine which differences are significant. There are four stars where the average positional offset is greater than the average positional uncertainty in R.A., and an additional four stars have an average offset greater than the average positional uncertainty in decl. Hence, a total of 8 out of the 70 stars near the target also show these significant offsets. Thus, this effect is seen for roughly 10% of the stars and so is not very unusual. Although we currently have no explanation for its significance, it appears random, and thus we include the astrometric offset when analyzing the data, although it may be attributed to binarity (see Section 7.4 and Section 4.1 in the main paper). See Appendix H for additional details.

---

[27] Note that even before the bias correction of Section 4.2.4 is applied, this color offset is still present. In fact, it is slightly larger, with $\Delta_x = -0.79$ mas and $\Delta_y = 0.52$ mas. The bias correction is not the source of the color-dependent astrometric offset; rather, it helps to slightly decrease the offset.

### 4.2.6. Comparison to Gaia Proper Motions and Parallaxes

For the three targets with astrometric solutions in Gaia EDR3 (MB10364, OB110037, and OB110310; Table 3), the Gaia proper motions and parallaxes are compared to the fit proper motions and parallaxes presented in Section 7 and Tables 10–12. Direct comparisons are made in Table 5 and Figures 10 and 11. Note that we fit a proper motion and parallax to the source and lens along with an astrometric microlensing model. On the other hand, Gaia fits a proper motion and parallax to the source and lens (the "target"), as they are unresolved, and assumes that the target is a single star with parallax. The effect of astrometric lensing in Gaia on the proper motions is negligible (Appendix D). Additional details about the various Gaia metrics discussed are in Appendix E and Lindegren et al. (2021a).

To make proper-motion comparisons between Gaia and HST, the proper motions from the HST frame in which the fitting was performed need to be transformed into the absolute Gaia frame, as the iterative astrometric alignment procedure described in Section 4.2 produces a reference frame that is at rest with the average proper motion of the aligned stars (Lu et al. 2016). See Appendix C on how the proper-motion offset between the HST and Gaia frames is calculated. The source and lens proper motion in the Gaia frame, as well as the Gaia target proper motions, are listed in Table 5 for MB10364, OB110037, and OB110310. The vector point diagram for all stars from the HST observations transformed to the Gaia frame, along with the $1\sigma - 2\sigma - 3\sigma$ contours from the source and lens fit, are shown in Figure 10. For MB10364, OB110037, and OB110310 the target proper motion from Gaia is also included.

MB10364.—MB10364's proper motion in Gaia is $(-7.43 \pm 0.08, -6.80 \pm 0.05)$ mas yr^{-1}. The fit from HST for the lens is $(-5.11^{+1.62}_{-1.10}, -7.78^{+0.58}_{-0.89})$ mas yr^{-1}, inconsistent with Gaia in R.A. and decl. at $\sim 2\sigma$. The fit from HST for the source is $(-7.56^{+0.12}_{-0.12}, -6.49^{+0.11}_{-0.11})$ mas yr^{-1}, inconsistent with Gaia in decl. at $\sim 2\sigma$. MB10364 has parallax $\pi = 0.43 \pm 0.08$ in Gaia. The source and lens parallax from the MB10364 fits are $\pi_S = 0.11^{+0.02}_{-0.02}$, $\pi_L = 0.24^{+0.08}_{-0.06}$, neither of which is consistent with the Gaia value. The Gaia fit for MB10364 has a large renormalized unit weight error (RUWE = 1.388) and a large astrometric excess noise ($\epsilon = 0.406$ mas) with high significance ($D = 12.020$), indicating that the single-star model is not providing a good fit. This mismatch is not due to astrometric microlensing (Appendix D). The most likely explanation for the discrepancies is crowding—there are several stars close to MB10364 that would cause confusion (Figures 1 and 12). As the source and lens are not resolvable, the fact that 15% of the image parameter determination (IPD) algorithm has identified a double peak is likely due to confusion. This means that the
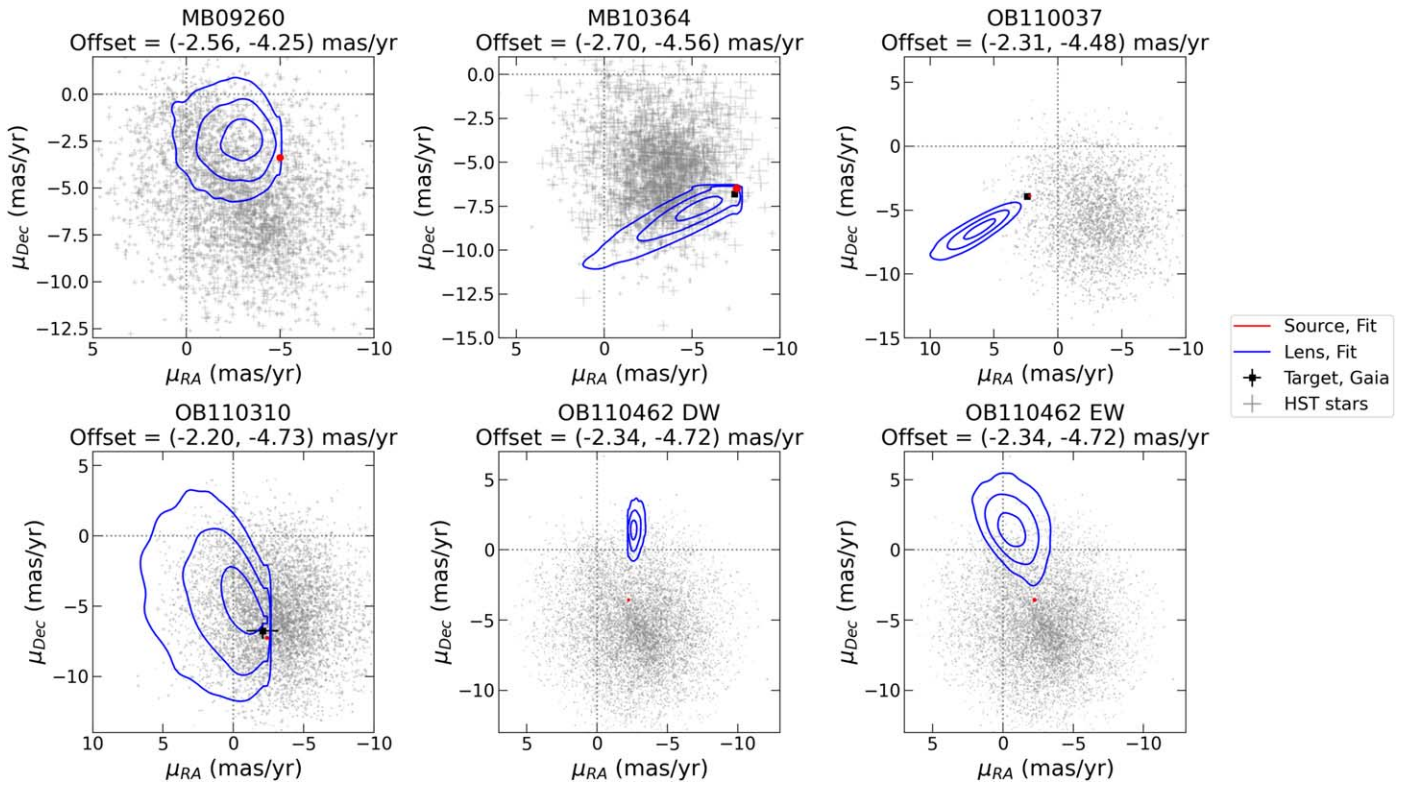
Figure 10. Proper motions for stars in the field of the target. The proper motions derived from F814W HST observations for stars within 30″ of the target are shown in gray with 1σ uncertainties. Only stars with F814W < 23 for MB09260, OB110310, and OB110462 and F814W < 22 for MB10364 and OB110037 are shown. For OB110462 there are two models depending on the likelihood used (default weighted "DW" or equal weighted "EW"; see Section 5.3 for details). As the alignment procedure places the stars in a reference frame where the relative motion is zero, a constant offset must be added to obtain proper motions in the original Gaia absolute reference frame. This offset is calculated by matching the stellar positions in HST to those in Gaia with `astrometric_excess_noise_sig < 2` and then calculating the 3σ clipped average weighted by the uncertainty in their difference. The offset value is given in the title for each field. For targets in Gaia where a single-star proper motion is estimated (MB10364, OB11037, OB110310), they are plotted as black squares. The lens and source proper motion as determined from fitting the HST data with a microlensing model is shown in blue and red $1\sigma - 2\sigma - 3\sigma$ contours, respectively. Note that the red contours are extremely small.
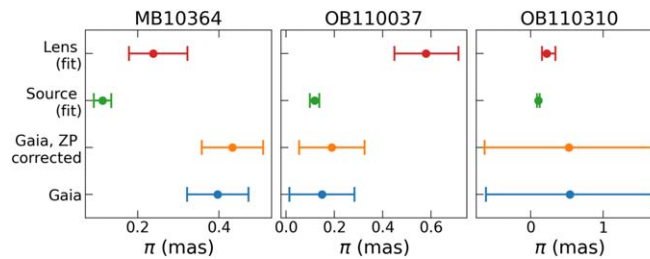
Figure 11. Comparison of Gaia parallaxes with the fit lens and source parallax.

Gaia measurement is not reliable. See Appendix E for further discussion.

OB110037.—OB110037's proper motion in Gaia is $(2.40 \pm 0.13, -3.91 \pm 0.09)$ mas yr^{-1}. The fit from HST for the lens is $(6.27^{+1.27}_{-1.20}, -6.56^{+0.77}_{-0.81})$ mas yr^{-1}, inconsistent with Gaia in both R.A. and decl. at $\sim 3\sigma$. The fit from HST for the source is $(2.19^{+0.24}_{-0.24}, -3.87^{+0.20}_{-0.20})$ mas yr^{-1}, consistent with Gaia. The caveat to this is that the fit to the HST F606W astrometry is poor (Figure 17). However, the astrometric lensing model is mostly independent of the proper-motion model, hence the proper-motion value can still be believed. OB110037 is very well measured and behaved in Gaia (it is the only target with a five-parameter solution; see Table 3). Additionally from the image (Figures 1 and 12), OB110037 is relatively bright and isolated. The fact that the fit source and Gaia proper motions are consistent would indicate that the lens

is dim in comparison to the star in Gaia G band. This makes sense, as the astrometric shift for OB110037 is undetectable by the time Gaia begins observing.

OB110037 is well modeled in Gaia by a single source with parallax. Although the microlensing model is a poor fit to the astrometry owing to a time-dependent color offset, the proper motions from our model are in good agreement with Gaia. OB110037 has parallax $\pi = 0.19 \pm 0.13$ in Gaia. The source and lens parallax from the OB110037 fits are $\pi_S = 0.12^{+0.02}_{-0.02}$, $\pi_L = 0.58^{+0.14}_{-0.13}$. The source parallax is consistent with the Gaia value. We note that the source may appear well behaved in Gaia because the astrometry is in a single filter. The multiband HST astrometry may be useful in identifying binary companions. See Appendix E for further discussion.

OB110310.—OB110310's proper motion in Gaia is $(-2.08 \pm 1.12, -6.75 \pm 0.58)$ mas yr^{-1}. The fit from HST for the lens is
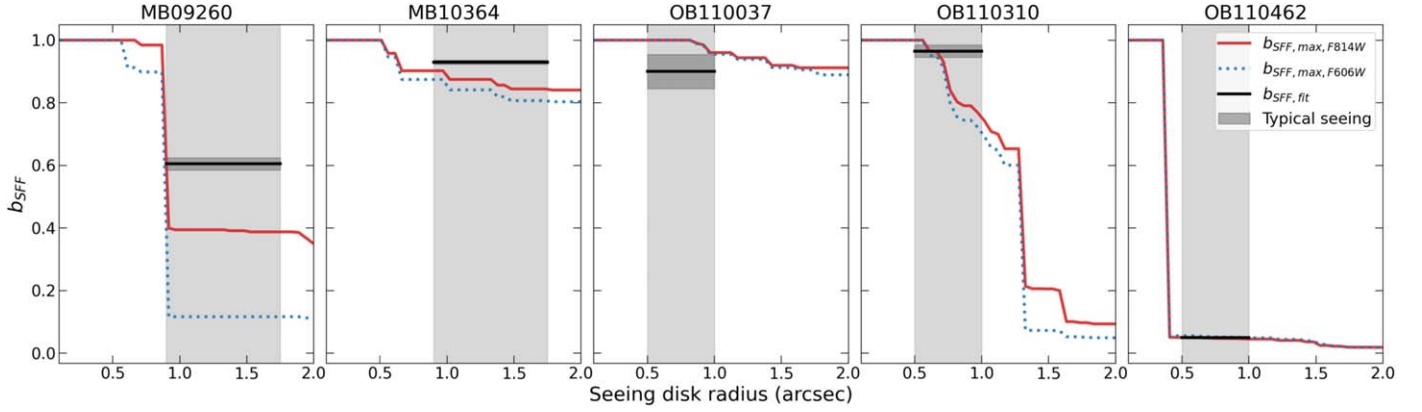
Figure 12. Comparison of b_{SFF} inferred from fitting microlensing events, as compared to upper limits inferred from the high-resolution HST images. The typical seeing disk *radius* ranges are shown in light gray for MOA (MB09260, MB10364) and OGLE (OB110037, OB110310, OB110462). The inferred value of b_{SFF} from fitting each microlensing event is shown as a black line, with uncertainties in dark gray. The upper limits on blending $b_{\mathrm{SFF,max}}$ as a function of aperture radius, as estimated using the method described in Section 7.7, are shown as the solid red line (F814W) and the dotted blue line (F606W). For the three OGLE targets, at the relevant seeing disk radii, the inferred values of b_{SFF} from the fit are at or below $b_{\mathrm{SFF,max}}$ as inferred from the HST images. For the two MOA targets, the inferred values of b_{SFF} are higher than the maximum value as inferred from the HST images. In the case of MB09260, this is likely due to the bright star around $1\farcs0$ from the target, which causes an abrupt change in b_{SFF} around that radius; proper convolution with a PSF would likely resolve the difference. In the case of MB10364, the difference is minimal and likely just due to the imperfect nature of the comparison (e.g., lack of proper PSF convolution, and F814W not exactly matching the red filter in MOA/OGLE).

$(-0.02^{+1.93}_{-1.16}, -4.68^{+2.39}_{-2.13})$ mas yr^{-1}, consistent with Gaia owing to large uncertainties in both Gaia and the fit. The fit from HST for the source is $(-2.41^{+0.12}_{-0.12}, -7.26^{+0.08}_{-0.08})$ mas yr^{-1}, consistent with Gaia. OB110310 has parallax $\pi = 0.53 \pm 1.16$ in Gaia (note that the OB110310 zero-point correction is an extrapolation), consistent with nondetection of parallax. The source and lens parallaxes from the OB110310 fit are $\pi_S = 0.10^{+0.02}_{-0.02}$, $\pi_L = 0.22^{+0.12}_{-0.07}$, which are both consistent within the very wide uncertainties of Gaia. The fact that the source and Gaia proper motions are consistent would indicate that the lens is dim in comparison to the star in Gaia G band; blending in F814W and F606W also suggests a dark lens (Table 12). The fact that in the IPD 55% of transits have either truncation or multiple gates flagged in one or more windows indicates likely contamination. OB110310 is not very bright and is in a somewhat crowded region (Figures 1 and 12). The astrometric noise is large ($\epsilon = 0.894$ mas), but the value is insignificant ($D = 0.332$). Together these explain why the Gaia measurement does not produce very good constraints. See Appendix E for further discussion.

4.3. HST Photometric Analysis

To obtain precise relative photometry, for each epoch a small constant magnitude offset is applied to the stars. The offset is calculated by assuming that the reference stars have constant brightness in time, which we define as the 3σ clipped mean. As with the positional uncertainties, for the magnitude uncertainties we used the error on the mean, with an additional additive error empirically determined during the astrometric alignment process; details are in Appendix A.

Analogous to the positional transformation, we evaluate the magnitude transformation by checking how well a constant magnitude describes the stars

$$\chi^2_m = \sum_i \left(\frac{m_i - m_0}{\sigma_{m_i}} \right)^2, \tag{15}$$

where m_i are the calibrated magnitudes, m_0 is the constant magnitude fit, and σ_{m_i} is the uncertainty on the calibrated

magnitude. The χ^2 distributions for the magnitude residuals of the reference stars detected in all N_{ep} epochs are shown in the bottom panels of Figure 9. The expected residual distribution has $N_{\mathrm{ep,detect}} - 1$ degrees of freedom, as there is one free parameter in the constant magnitude fit.

The final positions and magnitudes of the targets resulting from the analysis in this section are presented in Table 6. The photometry is shown in Figures 3–8, and the astrometry is shown in Figures 13–18.

5. Microlensing Modeling

The mass of the lens M_L in a microlensing event is given by

$$M_L = \frac{\theta_{\mathrm{E}}}{\kappa \pi_{\mathrm{E}}}, \tag{16}$$

where θ_{E} is the angular Einstein radius (Equation (17)), π_{E} is the microlensing parallax (Equation (21)), and $\kappa = 4G/(1AU \cdot c^2) = 8.14$ mas$/M_\odot$ is a constant. Densely sampled photometric microlensing observations constrain π_{E}, while astrometric microlensing observations constrain θ_{E}.[28]

To measure these quantities of interest, we simultaneously fit the ground-based photometry and HST photometry and astrometry with a point-source point-lens (PSPL) microlensing model with parallax. We do not consider models involving either binary lenses or sources, nor higher-order effects beyond parallax; these are beyond the scope of this work. Discussion of the need for models more complex than PSPL with parallax can be found in Section 7.

Throughout this section and the remainder of the paper, we report vector quantities decomposed into their R.A. and decl. components, subscripted by "α^*" and "δ." Because we work solely in the equatorial coordinate system, we also equivalently refer to R.A. as east and decl. as north, subscripted by "E" and "N," where R.A. increases to the east and decl. increases to the north.

---

[28] Theoretically, astrometric microlensing observations should also be able to constrain π_{E}, but due to the cadence of observations, this is currently unachievable.
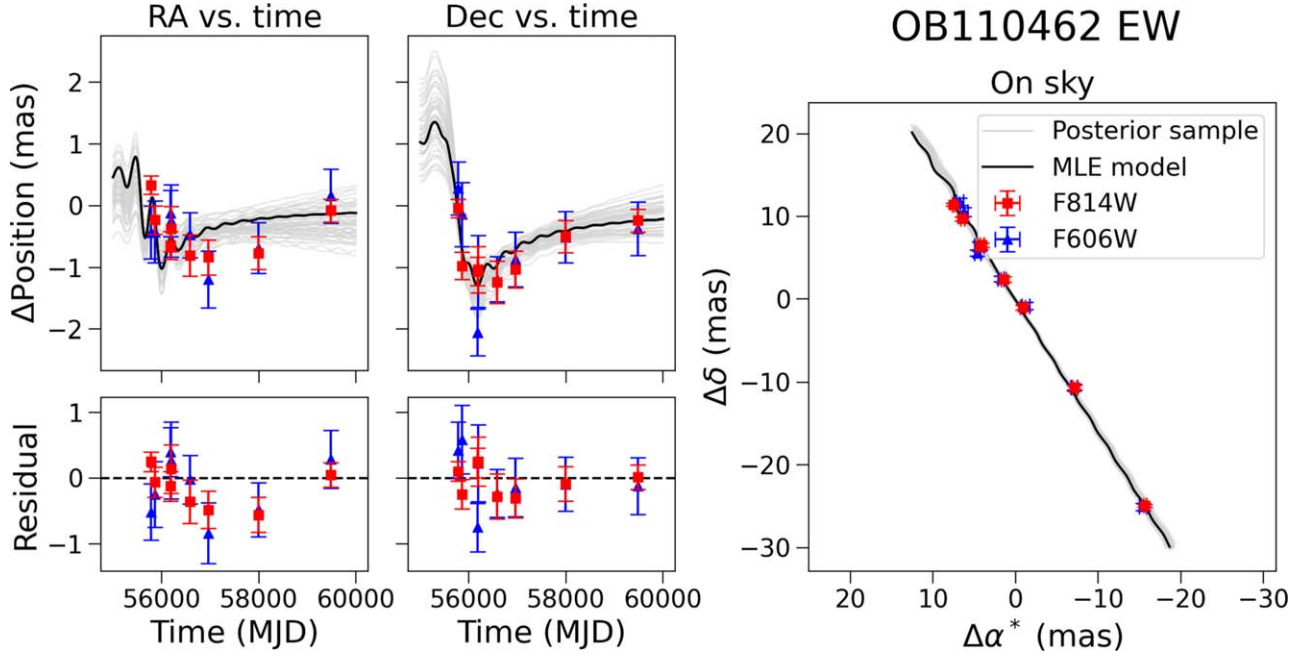
Figure 13. OB110462 astrometry, using the equally weighted likelihood. Left column, top to bottom: R.A. vs. time with MLE unlensed source motion model subtracted; residuals to the MLE model for R.A. vs. time fit. HST F814W astrometry data are shown in red; HST F606W astrometry data are shown in blue. The MLE model is shown in black. Fifty random draws from the posterior distribution are shown in light gray. Middle column, top to bottom: same as the left column, except decl. instead of R.A. Right panel: astrometry as seen on sky, in the barycentric frame. OB110462 shows a strong >1 mas astrometric microlensing signal.
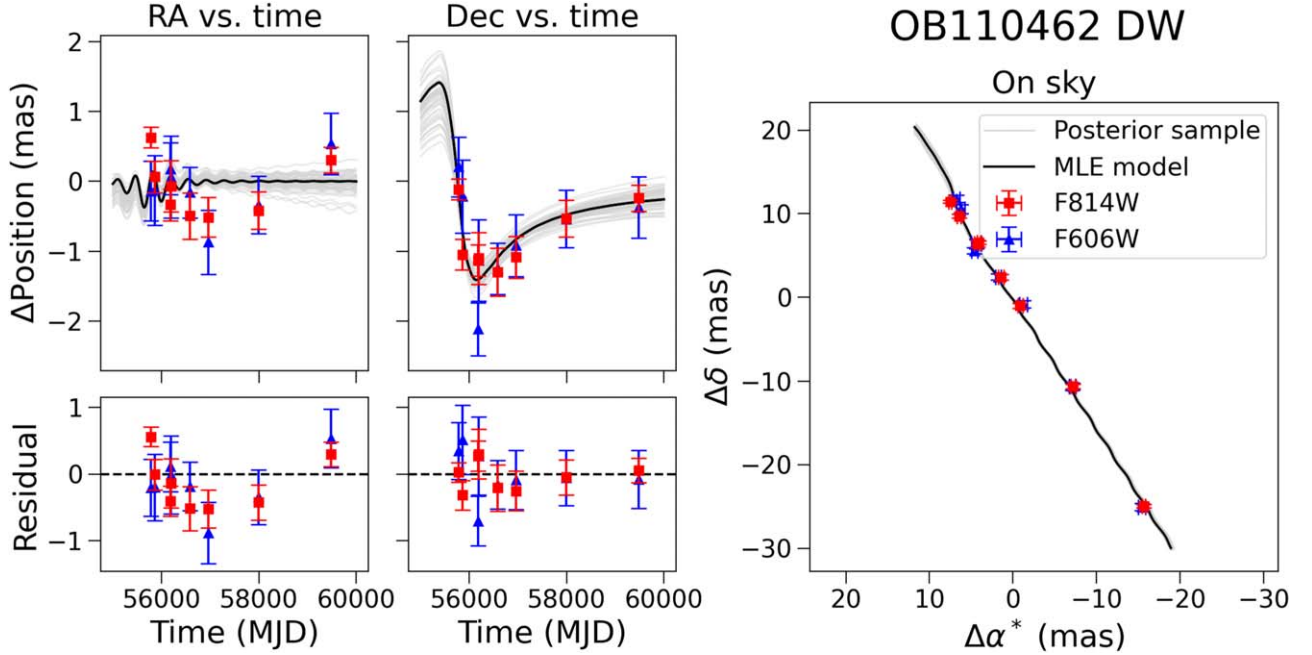
Figure 14. Same as Figure 13, but using the default weighted likelihood for OB110462.

5.1. Microlensing Definitions

All microlensing quantities defined in the following section are in the heliocentric reference frame.

By rearranging the terms in Equation (16), the Einstein radius, which sets the angular scale of the microlensing event, can be written as

$$\theta_E = \sqrt{\kappa \pi_{\rm rel} M_L}, \qquad (17)$$

where $\pi_{\rm rel} = \pi_L - \pi_S$ is the relative parallax of the lens and source.

The Einstein crossing time t_E, the time it takes for the source to traverse the angular radius of the lens and that sets the timescale of the events, is given by

$$t_E = \frac{\theta_E}{\mu_{\rm rel}}, \qquad (18)$$

where $\mu_{\rm rel}$ is the lens−source proper motion $|\boldsymbol{\mu}_S - \boldsymbol{\mu}_L|$.

The source−lens separation on sky $\boldsymbol{\theta}_S - \boldsymbol{\theta}_L$ normalized by the Einstein radius is denoted $\boldsymbol{u}(t)$. The minimum separation is denoted $\boldsymbol{u}(t_0) = \boldsymbol{u}_0$. The impact parameter u_0 is the scalar quantity associated with $\boldsymbol{u}_0$. We follow the convention of
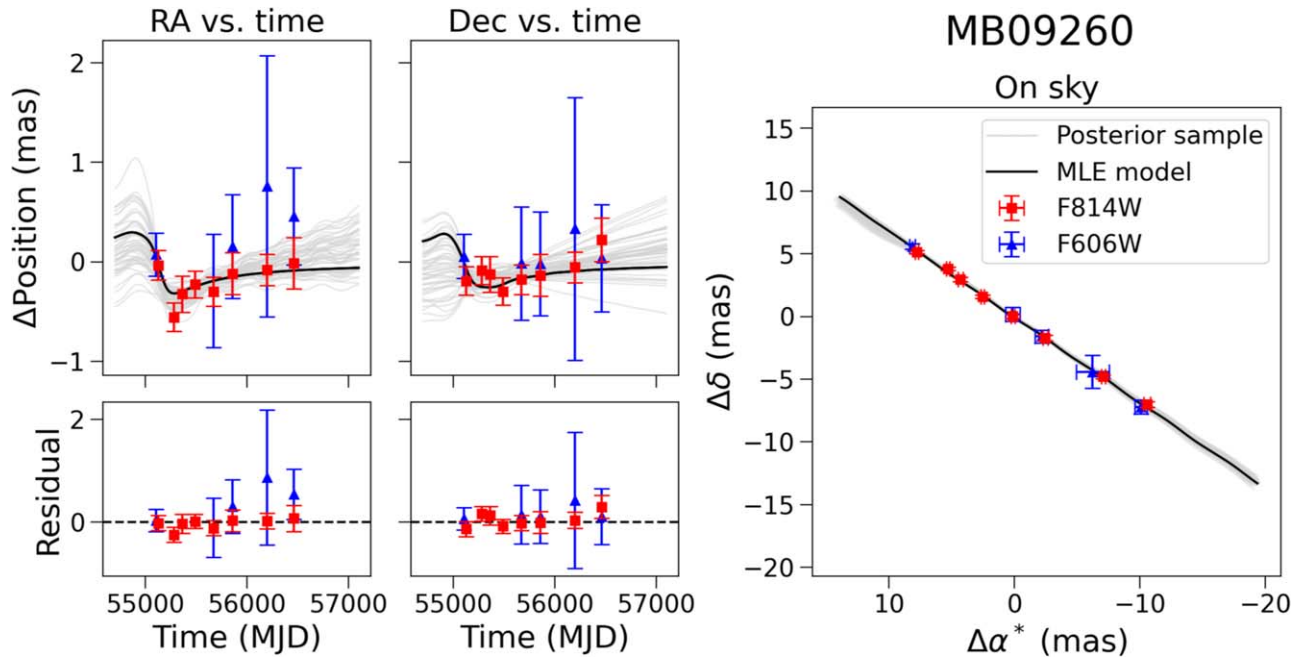
Figure 15. MB09260 astrometry. Same as Figure 13, but for MB09260. The astrometric signal is small and around the limit of the precision of the F814W measurements.
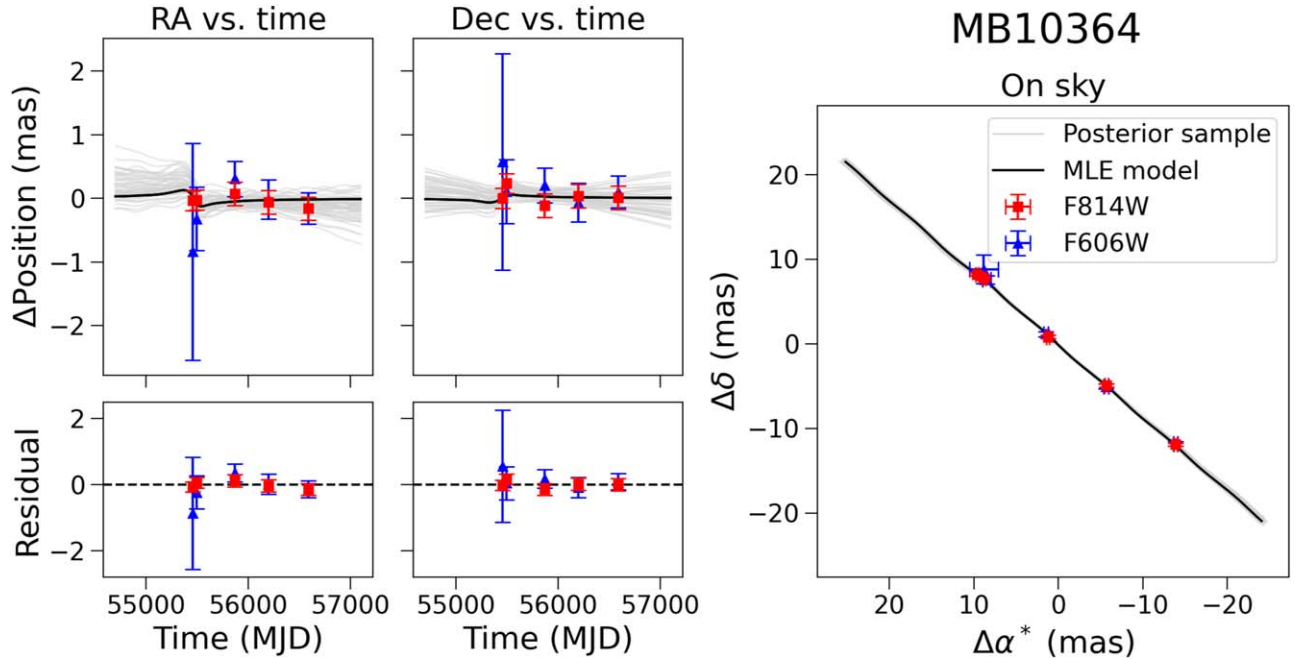
Figure 16. Same as Figure 13, but for MB10364. The astrometric signal is small, at or below the limit of the precision of the F814W measurements.

Gould (2004) where if $u_{0,E} > 0$, the source is to the east of the lens and $u_0 > 0$, and if $u_{0,E} < 0$, the source is to the west of the lens, and $u_0 < 0$.[29] If rectilinear motion is assumed, the lens

−source separation is given by

$$\boldsymbol{u}(t) = \boldsymbol{u}_0 + \frac{t - t_0}{t_E} \hat{\boldsymbol{\mu}}_{\text{rel}}. \quad (19)$$

However, an Earth observer's perspective of the lensing event is modulated by Earth's motion around the Sun. For events with long duration ($t_E \gtrsim 3$ months), Earth's orbital motion violates this rectilinear assumption and must be taken into account. This modifies $\boldsymbol{u}(t)$ to

$$\boldsymbol{u}(t) = \boldsymbol{u}_0 + \frac{t - t_0}{t_E} \hat{\boldsymbol{\mu}}_{\text{rel}} - \pi_E \boldsymbol{P}(t), \quad (20)$$

---

[29] Note that we define our coordinate system differently than Gould (2004). Gould (2004) works in a system where the position of the source relative to the lens is defined in a coordinate system that is right-handed in the relative proper motion and minimum separation vector. However, we work in a system where the coordinate system is consistent on the sky; this means that a coordinate system based on the relative proper motion and minimum separation vector does not always preserve handedness.
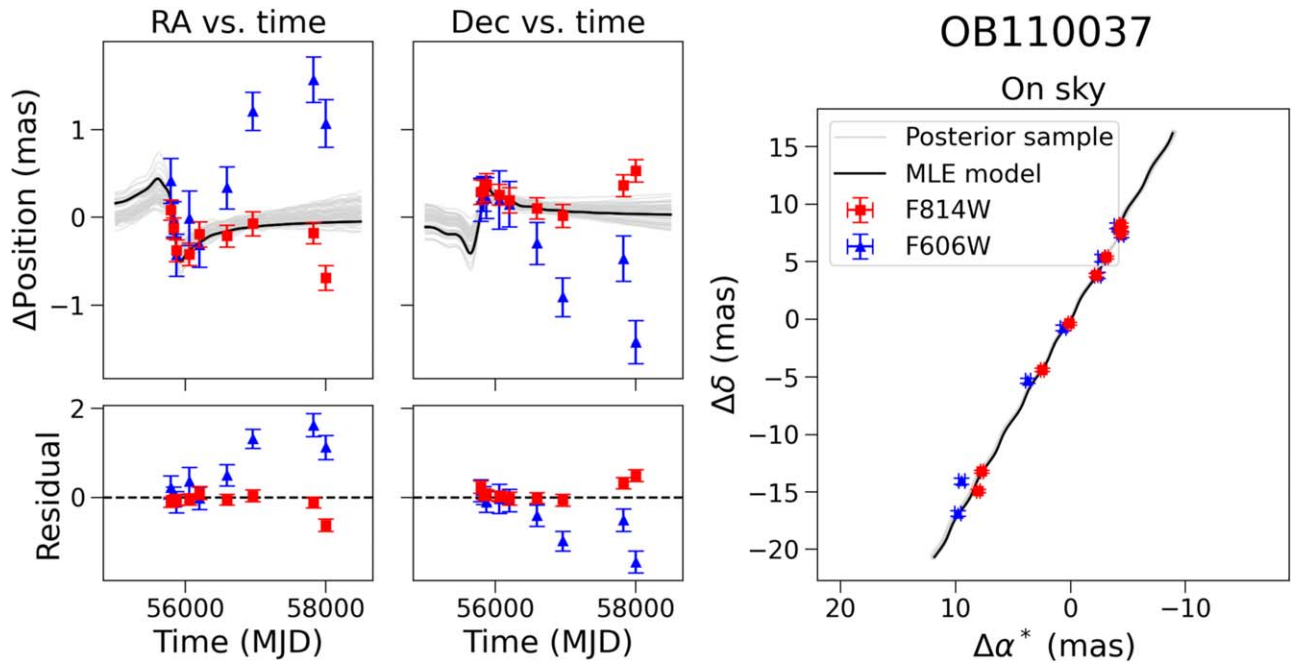
Figure 17. Same as Figure 13, but for OB110037. The photometry and astrometry seem to indicate that this object is a binary.
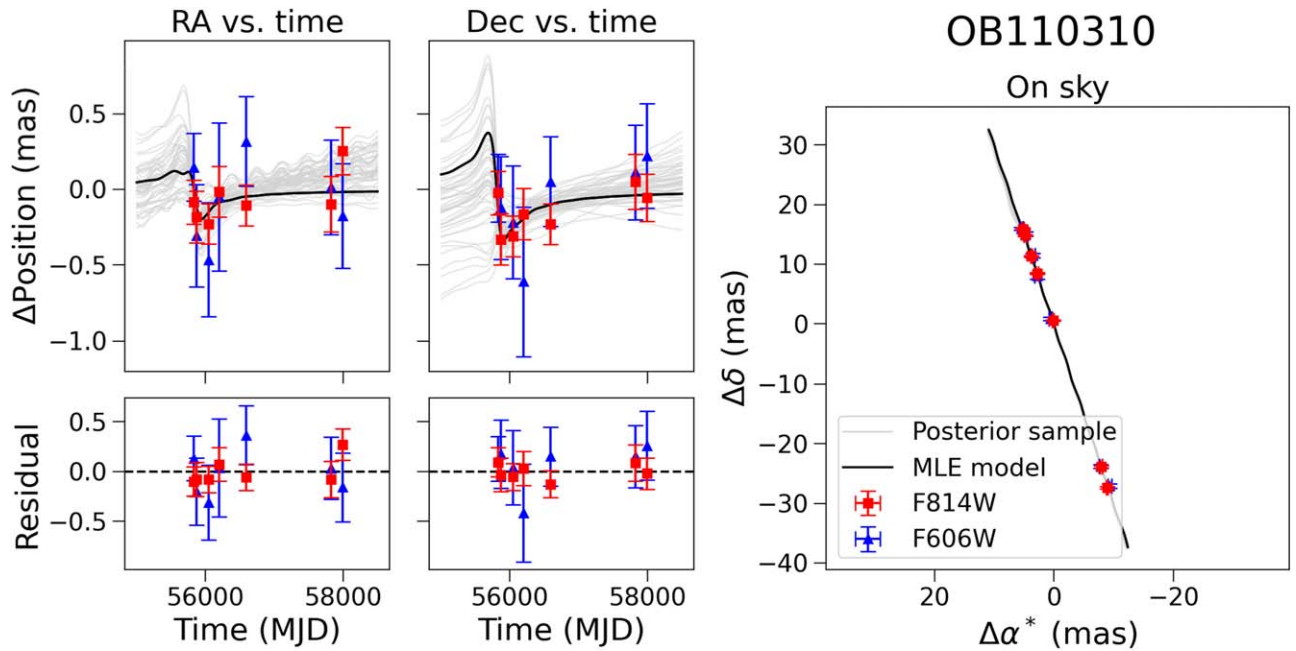
Figure 18. Same as Figure 13, but for OB110310. The astrometric signal is small and around the limit of the precision of the F814W measurements.

where

$$\pi_{\rm E} = \frac{\pi_{\rm rel}}{\theta_{\rm E}} \qquad (21)$$

is the microlensing parallax and $\boldsymbol{P}(t)$ is the parallax vector, defined to be the Sun–Earth separation vector normalized by 1 au. The microlensing parallax vector $\boldsymbol{\pi}_{\rm E}$ (not to be confused with the parallax vector $\boldsymbol{P}(t)$) encodes the magnitude of the microlensing parallax and the direction of the relative source−lens proper motion:

$$\boldsymbol{\pi}_{\rm E} = \pi_{\rm E}\, \hat{\boldsymbol{\mu}}_{\rm rel}. \qquad (22)$$

The photometric brightening of the source is given by

$$A(u) = \frac{u^2 + 2}{u\sqrt{u^2 + 4}}, \qquad (23)$$

where the total flux $F(t)$ in the telescope aperture is

$$F(t) = A(t)F_S + F_L + F_N \qquad (24)$$

where F_S, F_L, and F_N are the fluxes of the source, lens, and neighboring unlensed stars in the aperture of the telescope, respectively. The source flux fraction is

$$b_{\text{SFF}} = \frac{F_S}{F_S + F_L + F_N} \qquad (25)$$

and quantifies the fraction of light lensed in an observed microlensing event. Note that b_{SFF} depends on the observing wavelength and seeing/aperture. The nonsource flux $F_L + F_N$ is also called blend flux. Blend flux decreases b_{SFF} and dilutes the magnitude of both the photometric amplification and astrometric shift.

A PSPL photometric microlensing event is characterized by five geometric parameters: t_0, u_0, t_E, and π_E. For each telescope that observes this event, two additional parameters, m_{base} and b_{SFF}, are needed to describe each light curve; these depend on the seeing and camera filter. As all photometric microlensing observable quantities are normalized by θ_E, the lens mass cannot be determined.

In contrast, astrometric microlensing provides a direct measurement of θ_E. The apparent position of the source, i.e., the centroid of the lensed source images $\boldsymbol{\theta}_{S,c}$, is given by

$$\boldsymbol{\theta}_{S,c}(u, \theta_E) = \frac{(u^2 + 3)\boldsymbol{u}\theta_E}{u^2 + 2}. \qquad (26)$$

Assuming no blended light, the difference between the source's apparent and true positions, i.e., the astrometric shift, is given by

$$\boldsymbol{\delta}_c(u, \theta_E) = \frac{\boldsymbol{u}\theta_E}{u^2 + 2}. \qquad (27)$$

The astrometric shift δ_c is maximized at $u = \sqrt{2}$. This corresponds to the value of the maximum astrometric shift

$$\delta_{c,\text{max}} = \frac{\theta_E}{\sqrt{8}}, \qquad (28)$$

which is directly proportional to the Einstein radius.

Note that Equation (27) is for an unblended event, i.e., $b_{\text{SFF}} = 1$. If an event has $b_{\text{SFF}} < 1$, the nonsource light would dilute the astrometric shift (see Equations (11) and (12) in Lam et al. 2020). For the five candidates analyzed here, $b_{\text{SFF}} \sim 1$ in the HST filters, so assuming that the astrometry is unblended in HST is valid.

5.2. Modeling Framework

We perform parameter estimation using a Bayesian framework. Bayes's theorem

$$\pi(\boldsymbol{\Theta})\mathcal{L}(\boldsymbol{y}|\boldsymbol{\Theta}) = \mathcal{Z}(\boldsymbol{y})\mathcal{P}(\boldsymbol{\Theta}|\boldsymbol{y}) \qquad (29)$$

relates the prior π and likelihood $\mathcal{L}$ to the evidence $\mathcal{Z}$ and posterior $\mathcal{P}$. The goal of parameter estimation is to calculate $\mathcal{P}$. The likelihood $\mathcal{L}(\boldsymbol{y}|\boldsymbol{\Theta})$ is presented in Appendix F, and the priors $\pi(\boldsymbol{\Theta})$ are discussed in Appendix G.

The data are fit using MultiNest (Feroz et al. 2009), an implementation of the nested sampling algorithm (Skilling 2004). Nested sampling produces an estimate of the evidence $\mathcal{Z} = \int \pi(\boldsymbol{\Theta})\mathcal{L}(\boldsymbol{\Theta}) d\boldsymbol{\Theta}$ and, as a by-product, the posterior $\mathcal{P}$. In contrast to methods such as Markov Chain Monte Carlo, nested sampling is designed to better explore

multimodal likelihood spaces; however, care must still be taken to ensure that all local minima are explored.

5.3. Likelihood Weighting

There is a question of how best to combine the photometry and astrometry data sets, as they represent two different types of measurements. In particular, the question is how much weight each data set should receive given that there are several orders of magnitude more ground-based data points than HST data points. Thus, the ground-based photometry has an outsized effect on the likelihood. It can be argued that each data point should contribute equally to the likelihood. We consider this to be "default weight" (hereafter abbreviated as DW) likelihood, i.e.,

$$\log \mathcal{L}_{\text{tot}} = \log \mathcal{L}_{O,\text{phot}} + \log \mathcal{L}_{H,\text{phot}} + \log \mathcal{L}_{H,\text{ast}}, \qquad (30)$$

where $\mathcal{L}_{O,\text{phot}}$, $\mathcal{L}_{H,\text{phot}}$, and $\mathcal{L}_{H,\text{ast}}$ are the likelihoods of the OGLE or MOA photometry, HST photometry, and HST astrometry, respectively.

However, it could also be argued that each data set is independent, and so should each contribute equally to the likelihood. We call this the "equal weight" (hereafter abbreviated as EW) likelihood, i.e.,

$$\log \mathcal{L}_{\text{tot}} = \frac{\log \mathcal{L}_{O,\text{phot}}}{n_{O,\text{phot}}} + \frac{\log \mathcal{L}_{H,\text{phot}}}{n_{H,\text{phot}}} + \frac{\log \mathcal{L}_{H,\text{ast}}}{n_{H,\text{ast}}} \qquad (31)$$

where $n_{O,\text{phot}}$, $n_{H,\text{phot}}$, and $n_{H,\text{ast}}$ are the number of data points in in the OGLE photometry, HST photometry, and HST astrometry, respectively.

These different likelihoods are essentially giving the different data sets different weights, in the case in which they are inconsistent with each other. For all targets, we fit using the default weight likelihood; for OB110462 we additionally fit using the equal weight likelihood.

6. Constraining the Nature of the Lens

By modeling photometric and astrometric microlensing data as described in Section 5, the lens's mass can be measured. However, a mass measurement alone cannot distinguish the difference between a $5\,M_\odot$ stellar lens and a $5\,M_\odot$ BH. Additional information about the lens's brightness is needed, which can be estimated using the source flux fractions in the high-resolution HST filters. By calculating the brightest star allowed by the inferred source flux fractions, we can determine whether a luminous lens (i.e., stellar lens) or dark lens (i.e., compact object lens) scenario is more likely.

We follow a procedure similar to Wyrzykowski et al. (2016) in order to calculate the probability of a dark lens. The two main differences between the analysis of Wyrzykowski et al. (2016) and ours are that they work with photometric data only and must invoke a Galactic model to obtain lens masses and distances, while in our case astrometric data allow us to fit lens masses and distances. This greatly simplifies the analysis, as we do not need to calculate the Jacobian to transform the probability density functions between different variables. In addition, we use realistic stellar and Galactic models to determine the lens luminosities, instead of relying on simple mass–luminosity scaling relations.

From fitting the microlensing data, we have posterior distributions for the lens mass M_L, distance d_L, baseline magnitude m_{base}, and source flux fraction b_{SFF}. In the following

Table 6
HST Calibrated Data for Each Target

Target	Filter	Date (yyyy-mm-dd)	R.A. (mas)	Decl. (mas)	Mag (Vega)
MB09260	F814W	2009-10-19	7.80 ± 0.15	5.15 ± 0.14	15.484 ± 0.005
		2010-03-22	5.31 ± 0.14	3.80 ± 0.14	17.656 ± 0.005
		2010-06-14	4.31 ± 0.18	2.97 ± 0.18	17.760 ± 0.007
		2010-10-20	2.54 ± 0.14	1.60 ± 0.14	17.812 ± 0.014
		2011-04-19	0.12 ± 0.15	0.01 ± 0.15	17.838 ± 0.018
		2011-10-24	−2.44 ± 0.21	−1.71 ± 0.21	17.833 ± 0.005
		2012-09-25	−7.07 ± 0.15	−4.80 ± 0.15	17.836 ± 0.007
		2013-06-17	−10.57 ± 0.26	−7.02 ± 0.22	17.829 ± 0.011
	F606W	2009-10-01	8.15 ± 0.22	5.57 ± 0.22	17.899 ± 0.013
		2011-04-19	0.13 ± 0.57	0.17 ± 0.57	20.750 ± 0.083
		2011-10-24	−2.17 ± 0.52	−1.59 ± 0.52	20.748 ± 0.007
		2012-09-25	−6.23 ± 1.31	−4.41 ± 1.32	20.733 ± 0.023
		2013-06-17	−10.10 ± 0.49	−7.21 ± 0.54	20.738 ± 0.036
MB10364	F814W	2010-09-13	9.61 ± 0.16	8.24 ± 0.16	13.366 ± 0.011
		2010-10-26	8.76 ± 0.16	7.72 ± 0.15	14.657 ± 0.005
		2011-10-31	1.23 ± 0.19	0.81 ± 0.18	15.315 ± 0.006
		2012-09-25	−5.70 ± 0.19	−4.89 ± 0.19	15.315 ± 0.010
		2013-10-24	−13.90 ± 0.18	−11.89 ± 0.18	15.316 ± 0.009
	F606W	2010-09-13	8.81 ± 1.70	8.81 ± 1.70	14.538 ± 0.017
		2010-10-26	8.46 ± 0.50	7.59 ± 0.50	15.842 ± 0.017
		2011-10-31	1.47 ± 0.28	1.13 ± 0.28	16.498 ± 0.006
		2012-09-25	−5.66 ± 0.31	−4.99 ± 0.31	16.504 ± 0.008
		2013-10-24	−13.89 ± 0.25	−11.79 ± 0.25	16.502 ± 0.008
OB110037	F814W	2011-08-15	−4.35 ± 0.11	8.24 ± 0.14	14.864 ± 0.021
		2011-09-26	−4.33 ± 0.12	7.82 ± 0.12	15.029 ± 0.005
		2011-11-01	−4.34 ± 0.12	7.52 ± 0.12	15.774 ± 0.006
		2012-05-07	−3.10 ± 0.13	5.40 ± 0.12	16.315 ± 0.019
		2012-09-25	−2.22 ± 0.14	3.86 ± 0.14	16.321 ± 0.009
		2013-10-21	0.10 ± 0.12	−0.36 ± 0.12	16.327 ± 0.005
		2014-10-26	2.45 ± 0.14	−4.36 ± 0.13	16.328 ± 0.006
		2017-03-13	7.74 ± 0.12	−13.21 ± 0.12	16.334 ± 0.007
		2017-09-04	8.05 ± 0.14	−14.90 ± 0.13	16.322 ± 0.011
	F606W	2011-08-15	−4.02 ± 0.25	8.15 ± 0.24	16.916 ± 0.011
		2011-09-26	−4.23 ± 0.20	7.79 ± 0.20	17.086 ± 0.020
		2011-11-01	−4.39 ± 0.24	7.36 ± 0.23	17.794 ± 0.005
		2012-05-07	−2.69 ± 0.31	5.34 ± 0.33	18.301 ± 0.016
		2012-09-25	−2.34 ± 0.26	3.81 ± 0.26	18.306 ± 0.006
		2013-10-21	0.65 ± 0.24	−0.76 ± 0.24	18.314 ± 0.006
		2014-10-26	3.73 ± 0.22	−5.29 ± 0.22	18.320 ± 0.015
		2017-03-13	9.48 ± 0.26	−14.04 ± 0.26	18.331 ± 0.008
		2017-09-04	9.80 ± 0.27	−16.84 ± 0.24	18.326 ± 0.027
OB110310	F814W	2011-09-21	5.20 ± 0.14	15.95 ± 0.14	16.945 ± 0.013
		2011-10-31	4.86 ± 0.17	14.85 ± 0.17	18.058 ± 0.004
		2012-04-24	3.79 ± 0.13	11.35 ± 0.13	18.602 ± 0.013
		2012-09-24	2.82 ± 0.17	8.47 ± 0.17	18.616 ± 0.011
		2013-10-21	0.14 ± 0.13	0.59 ± 0.14	18.621 ± 0.005
		2017-03-14	−7.92 ± 0.18	−23.84 ± 0.18	18.608 ± 0.005
		2017-09-01	−8.88 ± 0.16	−27.36 ± 0.16	18.613 ± 0.012
	F606W	2011-09-21	5.43 ± 0.22	15.98 ± 0.22	19.663 ± 0.018
		2011-10-31	4.73 ± 0.34	15.06 ± 0.34	20.780 ± 0.007
		2012-04-24	3.55 ± 0.38	11.44 ± 0.37	21.329 ± 0.034
		2012-09-24	2.79 ± 0.49	8.02 ± 0.49	21.180 ± 0.212
		2013-10-21	0.56 ± 0.30	0.87 ± 0.30	21.339 ± 0.007
		2017-03-14	−7.81 ± 0.31	−23.78 ± 0.31	21.333 ± 0.022
		2017-09-01	−9.31 ± 0.34	−27.08 ± 0.35	21.335 ± 0.034
OB110462	F814W	2011-08-08	7.53 ± 0.15	11.45 ± 0.15	17.209 ± 0.028
		2011-10-31	6.44 ± 0.23	9.71 ± 0.22	18.849 ± 0.006
		2012-09-09	4.08 ± 0.23	6.55 ± 0.23	19.756 ± 0.009
		2012-09-25	4.25 ± 0.37	6.42 ± 0.37	19.767 ± 0.008
		2013-10-22	1.43 ± 0.33	2.40 ± 0.34	19.839 ± 0.048
		2014-10-26	−0.87 ± 0.29	−1.00 ± 0.30	19.881 ± 0.009
		2017-08-29	−7.18 ± 0.27	−10.61 ± 0.26	19.874 ± 0.009

Table 6
(Continued)

Target	Filter	Date (yyyy-mm-dd)	R.A. (mas)	Decl. (mas)	Mag (Vega)
		2021-10-01	-15.67 ± 0.19	-24.93 ± 0.19	19.865 ± 0.020
	F606W	2011-08-08	6.76 ± 0.43	11.77 ± 0.43	19.313 ± 0.023
		2011-10-31	6.25 ± 0.50	10.54 ± 0.52	20.974 ± 0.010
		2012-09-09	4.60 ± 0.37	5.57 ± 0.37	21.867 ± 0.050
		2012-09-25	4.38 ± 0.59	6.40 ± 0.59	21.920 ± 0.010
		2013-10-22	1.76 ± 0.37	2.45 ± 0.36	22.011 ± 0.015
		2014-10-26	-1.22 ± 0.46	-0.83 ± 0.44	22.042 ± 0.015
		2017-08-29	-7.10 ± 0.41	-10.62 ± 0.41	22.017 ± 0.027
		2021-10-01	-15.44 ± 0.44	-25.06 ± 0.44	22.021 ± 0.017

Note. Relative positions and magnitude of the target by epoch and filter.

Table 7
99.73% Credible Intervals/Upper Limits

Parameter	θ_E (mas)	$\delta_{c,\mathrm{max}}$ (mas)	$M_L(M_\odot)$	π_E
MB09260	<2.42	<0.85	$1.37^{+2.72}_{-1.16}$	$0.09^{+0.13}_{-0.03}$
MB10364	<1.76	<0.62	$0.21^{+0.61}_{-0.18}$	$0.27^{+0.02}_{-0.01}$
OB110037	$1.24^{+1.10}_{-0.90}$	$0.44^{+0.39}_{-0.32}$	$0.41^{+0.37}_{-0.30}$	$0.37^{+0.02}_{-0.02}$
OB110310	<2.75	<0.97	$0.78^{+2.98}_{-0.68}$	$0.13^{+0.20}_{-0.08}$
OB110462 (EW)	$4.13^{+2.98}_{-3.02}$	$1.46^{+1.05}_{-1.07}$	$2.15^{+3.50}_{-1.43}$	$0.24^{+0.11}_{-0.16}$
OB110462 (DW)	$3.89^{+1.69}_{-1.61}$	$1.37^{+0.60}_{-0.57}$	$3.79^{+2.17}_{-1.64}$	$0.12^{+0.03}_{-0.04}$

Note. There are two entries for OB110462, one based on a fit with "default weighting" (OB110462 DW) and one based on a fit with "equal weighting" (OB110462 EW). See Section 5.3 for details.

Table 8
Lens Type Probabilities in Percent

Target	Star	BD	WD	NS	BH
MB09260	4	0	38	44	14
MB10364	36	29	35	0	0
OB110037	74	0	26	0	0
OB110310	5	3	65	22	5
OB110462 DW	0	0	0	0	100
OB110462 EW	0	0	6	50	44

Note. The star probabilities are upper limits, while the BD, WD, NS, and BH probabilities are lower limits. This is because the luminous lens probabilities are upper limits and the dark lens probabilities are lower limits; see Section 6 for details. Note that there are two entries for OB110462, one based on a fit with "default weighting" (OB110462 DW) and one based on a fit with "equal weighting" (OB110462 EW). See Section 5.3 for details.

analysis we reassign any fit values with $b_{\mathrm{SFF}} \geqslant 1$ to instead be equal to 0.999999. This is because values of $b_{\mathrm{SFF}} \geqslant 1$ would result in an infinite lens magnitude (Equation (32)).[30]

We draw a random sample of 1000 stars from our posterior. For each star we calculate (1) the brightest lens allowed by b_{SFF} and m_{base} and (2) the brightest star allowed by M_L and d_L.

To calculate (1), by assuming that there are no contaminating neighbor stars, $b_{\mathrm{SFF}} = F_S/(F_S + F_L)$, an upper limit can be

placed on the brightness of the lens:

$$m_L = m_{\mathrm{base}} - 2.5 \log_{10}(1 - b_{\mathrm{SFF}}). \qquad (32)$$

We denote this $m_L(b_{\mathrm{SFF}}, m_{\mathrm{base}})$.

To calculate (2), we use the simple stellar population synthesis code SPISEA (Hosek et al. 2020) to generate a suite of simple stellar populations (SSPs) to simulate the possible lens population. We use the MISTv1.2 solar-metallicity isochrones (Choi et al. 2016), get_merged_atmosphere atmosphere model,[31] Damineli et al. (2016) reddening law, and Kroupa (2001) initial mass function (IMF) over the mass range $0.1\ M_\odot < M < 120\ M_\odot$. Each cluster is $10^4\ M_\odot$, in order to reduce stochastic effects in the sampling of the IMF.

SSPs are generated at the distances spanned by each target's lens distance posteriors, sampled every 0.25 kpc. SSPs of ages 7.0–10.0 $\log_{10}$ yr in increments of 0.5 $\log_{10}$ yr are simulated at each sampled distance in order to cover the age range of disk and bulge stars. The stellar age distribution as a function of distance is drawn from the Galaxia Milky Way stellar simulation (Sharma et al. 2011), which implements a version of the Besançon Galactic model of Robin et al. (2003). As our target sight lines are toward the bulge, most of the stars are old, with $\gtrsim$85% of stars being at least 9.0 $\log_{10}$ yr old, although younger stars tend to be at closer distances as disk stars dominate. To calculate the simulated stars' apparent magnitudes, we use the 3D extinction map of Marshall et al. (2006), accessed via the dustmaps software package (Green 2018), to obtain an A_{K_s} value for each distance.

For each sample from the posterior, we sample one of the SSPs at the corresponding distance at a particular stellar age from the Galactic distribution. All stars in the simulated SSP with masses within 10% of the sampled posterior mass are identified, and the brightest apparent magnitude of the star in this group is denoted $m_L(M_L, D_L, \star)$. If no stars are found within 10% of the sampled posterior mass, this indicates that stars of that mass have all died and formed compact objects.

If $m_L(M_L, D_L, \star) < m_L(b_{\mathrm{SFF}}, m_{\mathrm{base}})$, a star with the inferred stellar mass from stellar evolution models would be too bright to be hidden in the blended light allowed by the fit. This means that the lens is not a star. We take this to mean that the lens is a compact object and hence a dark lens. Thus, the lower limit on the probability of a dark lens in the observed filter is the

---

[30] One might worry that this could bias the results. However, a visual check comparing the posteriors (both individual and joint) for lens mass and distance do not show a change when excluding fits with $b_{\mathrm{SFF}} > 1$. In particular, the lens masses and distances are nearly independent of the lens magnitude. In addition, if the true value of b_{SFF} is 1, we would expect some scatter around that value, including unphysical >1 values.

[31] This is a combination of the ATLAS9 (Castelli & Kurucz 1994), PHOENIX v16 (Husser et al. 2013), BTSettl (Baraffe et al. 2015), and Koester10 (Koester 2010) models. For further details see Appendix B of Hosek et al. (2020).

Table 9
MB09260 Fit Values, Modes

Parameter	Mode 1			Mode 2		
	Med$^{+1\sigma}_{-1\sigma}$	MAP	MLE	Med$^{+1\sigma}_{-1\sigma}$	MAP	MLE
t_0 (MJD)	$55{,}099.19^{+1.40}_{-1.37}$	$55{,}099.27$	$55{,}099.27$	$55{,}099.33^{+1.26}_{-1.25}$	$55{,}099.99$	$55{,}099.99$
u_0	$-0.09^{+0.02}_{-0.04}$	-0.07	-0.07	$0.02^{+0.03}_{-0.06}$	-0.0002	-0.0002
t_E (days)	$143.16^{+3.35}_{-2.95}$	141.71	141.71	$142.37^{+3.43}_{-2.89}$	141.64	141.64
$\log_{10}(\theta_E/\mathrm{mas})$	$0.03^{+0.14}_{-0.20}$	0.24	0.24	$0.008^{+0.15}_{-0.21}$	0.06	0.06
π_S (mas)	$0.10^{+0.02}_{-0.02}$	0.12	0.12	$0.10^{+0.02}_{-0.02}$	0.09	0.09
$\pi_{E,E}$	$-0.08^{+0.010}_{-0.009}$	-0.08	-0.08	$-0.08^{+0.009}_{-0.009}$	-0.07	-0.07
$\pi_{E,N}$	$-0.02^{+0.03}_{-0.04}$	-0.005	-0.005	$-0.04^{+0.04}_{-0.06}$	-0.06	-0.06
$x_{S0,E}$ (mas)	$236.25^{+0.13}_{-0.12}$	236.43	236.43	$236.20^{+0.13}_{-0.11}$	236.30	236.30
$x_{S0,N}$ (mas)	$-692.07^{+0.11}_{-0.10}$	-692.15	-692.15	$-692.01^{+0.12}_{-0.13}$	-691.91	-691.91
$\mu_{S,E}$ (mas yr^{-1})	$-5.00^{+0.05}_{-0.05}$	-5.07	-5.07	$-4.99^{+0.05}_{-0.05}$	-5.05	-5.05
$\mu_{S,N}$ (mas yr^{-1})	$-3.38^{+0.04}_{-0.05}$	-3.34	-3.34	$-3.39^{+0.05}_{-0.05}$	-3.44	-3.44
$b_{SFF,M}$	$0.61^{+0.02}_{-0.02}$	0.60	0.60	$0.60^{+0.02}_{-0.02}$	0.61	0.61
$m_{base,M}$ (mag)	$17.43^{+0.003}_{-0.003}$	17.43	17.43	$17.43^{+0.003}_{-0.003}$	17.42	17.42
$b_{SFF,H8}$	$1.00^{+0.02}_{-0.03}$	0.99	0.99	$0.99^{+0.02}_{-0.03}$	1.00	1.00
$m_{base,H8}$ (mag)	$17.84^{+0.003}_{-0.004}$	17.83	17.83	$17.84^{+0.003}_{-0.003}$	17.84	17.84
$b_{SFF,H6}$	$1.03^{+0.02}_{-0.03}$	1.02	1.02	$1.02^{+0.02}_{-0.03}$	1.02	1.02
$m_{base,H6}$ (mag)	$20.75^{+0.007}_{-0.007}$	20.75	20.75	$20.75^{+0.006}_{-0.007}$	20.75	20.75
M_L ($M_\odot$)	$1.44^{+0.74}_{-0.59}$	2.70	2.70	$1.30^{+0.74}_{-0.58}$	1.44	1.44
π_L (mas)	$0.20^{+0.05}_{-0.04}$	0.25	0.25	$0.20^{+0.06}_{-0.04}$	0.20	0.20
π_{rel} (mas)	$0.09^{+0.04}_{-0.04}$	0.14	0.14	$0.10^{+0.05}_{-0.04}$	0.11	0.11
$\mu_{L,E}$ (mas yr^{-1})	$-2.62^{+1.18}_{-0.93}$	-0.61	-0.61	$-2.88^{+1.15}_{-0.94}$	-2.82	-2.82
$\mu_{L,N}$ (mas yr^{-1})	$-2.63^{+0.98}_{-0.91}$	-3.04	-3.04	$-2.40^{+1.09}_{-1.12}$	-1.49	-1.49
$\mu_{rel,E}$ (mas yr^{-1})	$-2.40^{+0.95}_{-1.17}$	-4.46	-4.46	$-2.11^{+0.94}_{-1.16}$	-2.23	-2.23
$\mu_{rel,N}$ (mas yr^{-1})	$-0.73^{+0.89}_{-1.01}$	-0.31	-0.31	$-1.01^{+1.15}_{-1.09}$	-1.95	-1.95
θ_E (mas)	$1.07^{+0.41}_{-0.40}$	1.73	1.73	$1.02^{+0.41}_{-0.39}$	1.15	1.15
π_E	$0.09^{+0.02}_{-0.01}$	0.08	0.08	$0.09^{+0.04}_{-0.01}$	0.10	0.10
$\delta_{c,max}$ (mas)	$0.38^{+0.15}_{-0.14}$	0.61	0.61	$0.36^{+0.15}_{-0.14}$	0.41	0.41
$\sum w_i$		0.42			0.58	
$\log \mathcal{Z}$		$31{,}613.22$			$31{,}613.55$	

Note. The columns list the median $\pm 1\sigma$ (68%) credible intervals, MAP solution, and MLE estimator solution for the microlensing parameters of MB09260. The posterior is multimodal (primarily in u_0); it has been split, and the parameters for each mode are reported separately. The fractions that each mode contributes to the whole posterior ($\sum w_i$) and log evidence ($\log \mathcal{Z}$) are listed for each mode at the end of the table.

fraction of samples where $m_L(M_L, D_L, \star) < m_L(b_{SFF}, m_{base})$ or no mass match is found.

Objects with $m_L(M_L, D_L, \star) > m_L(b_{SFF}, m_{base})$ are samples where a luminous stellar lens is consistent with the inferred amount of blending. Note that $m_L(b_{SFF}, m_{base})$ is an upper limit on the brightness of the lens, as we assumed that all the blended flux in Equation (32) is due to the lens; it could be due to unresolved unrelated neighbor stars. Thus, the upper limit on the probability of a stellar lens in the observed filter is thus the fraction of samples where $m_L(M_L, D_L, \star) > m_L(b_{SFF}, m_{base})$.

For dark lenses (i.e., any objects where $m_L(M_L, D_L, \star) < m_L(b_{SFF}, m_{base})$ or no star of the same mass was found in the simulated SSP), we categorize them as brown dwarfs (BD), white dwarfs (WD), NSs, or BHs by simplistically sorting them by their masses:

1. BDs: $M < 0.2\,M_\odot$
2. WDs: $0.2\,M_\odot < M < 1.2\,M_\odot$
3. NSs: $1.2\,M_\odot < M < 2.2\,M_\odot$
4. BHs: $M > 2.2\,M_\odot$.

In reality, there is overlap between WD and NS masses, and the overlap between NS and BH masses (if they overlap at all) is unknown. In addition, the maximum BD mass set by stellar physics is $0.08\,M_\odot$, but we extend this up to $0.2\,M_\odot$ to have continuity between the lowest-mass WDs of around $0.2\,M_\odot$. Hence, these values are only approximate.

The above analysis is performed for both the HST F606W and F814W filters. The reported probabilities are the joint constraint. A lens is dark if no masses consistent with a stellar lens are found in either filter. A lens is also dark if the maximum inferred lens flux is insufficient to hide a star (i.e., $m_L(M_L, D_L, \star) < m_L(b_{SFF}, m_{base})$) in either filter. A lens is luminous if the maximum inferred lens flux is sufficient to hide a star (i.e., $m_L(M_L, D_L, \star) > m_L(b_{SFF}, m_{base})$) in both filters. We do not perform this analysis for the OGLE or MOA photometry parameters, as the high-resolution HST images show that the seeing-limited apertures have unrelated neighbor stars in the blend, and hence the limits will all be weaker than using HST.

7. Results in Detail

A large (>1 mas) astrometric microlensing signal is detected in OB110462 (Section 7.1). A filter-dependent astrometric signal is also detected in OB110037 (Section 7.4); averaging

Table 10
MB10364 Fit Values

Parameter	Med$^{+1\sigma}_{-1\sigma}$	MAP	MLE
t_0 (MJD)	$55{,}445.13^{+0.12}_{-0.12}$	55,445.06	55,445.06
u_0	$-0.008^{+0.01}_{-0.01}$	-0.004	-0.004
t_E (days)	$61.11^{+0.24}_{-0.24}$	61.06	61.06
$\log_{10}(\theta_E/\text{mas})$	$-0.33^{+0.22}_{-0.25}$	-0.40	-0.40
π_S (mas)	$0.11^{+0.02}_{-0.02}$	0.11	0.11
$\pi_{E,E}$	$-0.24^{+0.003}_{-0.003}$	-0.24	-0.24
$\pi_{E,N}$	$0.12^{+0.01}_{-0.01}$	0.12	0.12
$x_{S0,E}$ (mas)	$130.18^{+0.11}_{-0.10}$	130.13	130.13
$x_{S0,N}$ (mas)	$-78.98^{+0.11}_{-0.10}$	-79.02	-79.02
$\mu_{S,E}$ (mas yr^{-1})	$-7.56^{+0.06}_{-0.06}$	-7.52	-7.52
$\mu_{S,N}$ (mas yr^{-1})	$-6.49^{+0.06}_{-0.06}$	-6.47	-6.47
$b_{SFF,M}$	$0.93^{+0.007}_{-0.007}$	0.93	0.93
$m_{base,M}$ (mag)	$15.02^{+0.00006}_{-0.00006}$	15.02	15.02
$b_{SFF,H8}$	$0.99^{+0.02}_{-0.02}$	0.98	0.98
$m_{base,H8}$ (mag)	$15.32^{+0.006}_{-0.006}$	15.32	15.32
$b_{SFF,H6}$	$1.00^{+0.02}_{-0.02}$	1.01	1.01
$m_{base,H6}$ (mag)	$16.50^{+0.006}_{-0.006}$	16.50	16.50
M_L ($M_\odot$)	$0.21^{+0.14}_{-0.10}$	0.18	0.18
π_L (mas)	$0.24^{+0.08}_{-0.06}$	0.22	0.22
π_{rel} (mas)	$0.12^{+0.08}_{-0.05}$	0.11	0.11
$\mu_{L,E}$ (mas yr^{-1})	$-5.11^{+1.62}_{-1.09}$	-5.38	-5.38
$\mu_{L,N}$ (mas yr^{-1})	$-7.78^{+0.57}_{-0.89}$	-7.56	-7.56
$\mu_{rel,E}$ (mas yr^{-1})	$-2.46^{+1.09}_{-1.61}$	-2.13	-2.13
$\mu_{rel,N}$ (mas yr^{-1})	$1.29^{+0.88}_{-0.57}$	1.09	1.09
θ_E (mas)	$0.46^{+0.31}_{-0.21}$	0.40	0.40
π_E	$0.27^{+0.005}_{-0.005}$	0.27	0.27
$\delta_{c,max}$ (mas)	$0.16^{+0.11}_{-0.07}$	0.14	0.14

Note. Same as Table 9, but for MB10364. The solution is unimodal; hence, there is only one column and Σw_i and $\log \mathcal{Z}$ are not reported.

Table 11
OB110037 Fit Values

Parameter	Med$^{+1\sigma}_{-1\sigma}$	MAP	MLE
t_0 (MJD)	$55{,}781.53^{+0.28}_{-0.30}$	55,781.49	55,781.49
u_0	$-0.002^{+0.03}_{-0.02}$	-0.008	-0.008
t_E (days)	$92.78^{+2.63}_{-2.60}$	93.31	93.31
$\log_{10}(\theta_E/\text{mas})$	$0.09^{+0.11}_{-0.14}$	0.22	0.22
π_S (mas)	$0.12^{+0.02}_{-0.02}$	0.11	0.11
$\pi_{E,E}$	$-0.31^{+0.005}_{-0.005}$	-0.31	-0.31
$\pi_{E,N}$	$0.21^{+0.01}_{-0.02}$	0.21	0.21
$x_{S0,E}$ (mas)	$15.21^{+0.06}_{-0.06}$	15.23	15.23
$x_{S0,N}$ (mas)	$-115.53^{+0.07}_{-0.07}$	-115.61	-115.61
$\mu_{S,E}$ (mas yr^{-1})	$2.19^{+0.02}_{-0.02}$	2.18	2.18
$\mu_{S,N}$ (mas yr^{-1})	$-3.87^{+0.02}_{-0.02}$	-3.86	-3.86
$b_{SFF,O}$	$0.90^{+0.06}_{-0.05}$	0.89	0.89
$m_{base,O}$ (mag)	$16.15^{+0.0003}_{-0.0003}$	16.15	16.15
$b_{SFF,H8}$	$0.91^{+0.06}_{-0.05}$	0.90	0.90
$m_{base,H8}$ (mag)	$16.33^{+0.003}_{-0.003}$	16.33	16.33
$b_{SFF,H6}$	$0.84^{+0.06}_{-0.05}$	0.82	0.82
$m_{base,H6}$ (mag)	$18.32^{+0.004}_{-0.003}$	18.31	18.31
M_L ($M_\odot$)	$0.41^{+0.12}_{-0.12}$	0.55	0.55
π_L (mas)	$0.58^{+0.14}_{-0.13}$	0.74	0.74
π_{rel} (mas)	$0.46^{+0.14}_{-0.13}$	0.62	0.62
$\mu_{L,E}$ (mas yr^{-1})	$6.27^{+1.25}_{-1.17}$	7.59	7.59
$\mu_{L,N}$ (mas yr^{-1})	$-6.56^{+0.74}_{-0.78}$	-7.54	-7.54
$\mu_{rel,E}$ (mas yr^{-1})	$-4.07^{+1.17}_{-1.25}$	-5.42	-5.42
$\mu_{rel,N}$ (mas yr^{-1})	$2.69^{+0.78}_{-0.75}$	3.68	3.68
θ_E (mas)	$1.24^{+0.36}_{-0.35}$	1.67	1.67
π_E	$0.37^{+0.008}_{-0.009}$	0.37	0.37
$\delta_{c,max}$ (mas)	$0.44^{+0.13}_{-0.12}$	0.59	0.59

Note. Same as Table 10, but for OB110037.

the astrometry across the F814W and F606W filters shows a small but significant 0.4 mas signal. The remaining three targets MB09260 (Section 7.2), MB10364 (Section 7.3), and OB110310 (Section 7.5) have astrometric signals that are below HST's detection threshold. Table 7 reports the lens masses, Einstein radii, maximum astrometric shifts, and microlensing parallaxes as either measured values or upper limits.

In Sections 7.1–7.5, the posteriors of the joint photometry and astrometry microlensing fits for the individual targets are presented. Tables 10–13 and 1–2 in Lam et al. (2022) list the median and 1σ (68%) credible intervals for each parameter, in addition to the maximum a posteriori (MAP) and maximum likelihood estimator (MLE)[32] solution.

Using the methodology described in Section 6, constraints are placed on the lens types of each target. We report the relative probabilities of star:BD:WD:NS:BH in Table 8. Figure 19 shows the distribution of dark versus luminous lens probability as a function of mass for each target. Table 8 lists the upper limit on the probability of a stellar lens and lower limits on the probabilities of different dark lenses for each target. In Section 7.9, we compare the yield of BHs from our search to that expected from simulations assuming that there are $\sim 10^8$ BHs in the Milky Way.

7.1. OB110462

The results for OB110462 are presented in Section 4.1 of Lam et al. (2022).

7.2. MB09260

The data and model for MB09260 are shown in Figures 3 (photometry) and 15 (astrometry), and the fit posteriors are summarized in Table 9. The inferred Einstein crossing time t_E is $142.64^{+3.49}_{-2.87}$ days, the microlensing parallax π_E is $0.09^{+0.03}_{-0.01}$, the Einstein radius θ_E is $1.04^{+0.42}_{-0.39}$, and the lens mass is $1.37^{+0.74}_{-0.60}\,M_\odot$.[33]

The probability that MB09260 has a dark lens is at least 96%, and the probability of a stellar lens is at most 4%. The relative probabilities of star:BD:WD:NS:BH are 4:0:38:44:14. Stellar lenses are only allowed below 1 $M_\odot$. A WD or NS is the most probable type of lens, with BHs possible but less likely.

7.3. MB10364

The data and model for MB10364 are shown in Figures 4 (photometry) and 16 (astrometry), and the fit posteriors are

---

[32] For most of the targets, the MAP solution is equal to the MLE solution, i.e., values of the parameters for the mode of the posterior distribution are the same as those where the likelihood function is maximized.

[33] These are the values for the posteriors before they are split into modes, which is why the values differ from what is reported in Table 9. However, since these parameters are all globally unimodal, their distributions are nearly identical across modes within the uncertainties, and neither mode is strongly favored, the values are not very different and we report the global median and uncertainties.

Table 12
OB110310 Fit Values, Modes

Parameter	Mode 1			Mode 2		
	Med$^{+1\sigma}_{-1\sigma}$	MAP	MLE	Med$^{+1\sigma}_{-1\sigma}$	MAP	MLE
t_0 (MJD)	$55,802.11^{+1.21}_{-1.57}$	55,801.39	55,801.39	$55,802.66^{+1.15}_{-1.17}$	55,801.95	55,801.95
u_0	$-0.18^{+0.05}_{-0.07}$	-0.24	-0.24	$-0.005^{+0.07}_{-0.08}$	-0.09	-0.09
t_E (days)	$83.40^{+2.39}_{-1.83}$	83.23	83.23	$82.20^{+1.66}_{-1.33}$	81.47	81.47
$\log_{10}(\theta_E/\mathrm{mas})$	$-0.05^{+0.24}_{-0.28}$	0.04	0.04	$-0.06^{+0.21}_{-0.28}$	0.04	0.04
π_S (mas)	$0.10^{+0.02}_{-0.02}$	0.10	0.10	$0.10^{+0.02}_{-0.02}$	0.09	0.09
$\pi_{E,E}$	$-0.08^{+0.01}_{-0.01}$	-0.09	-0.09	$-0.09^{+0.01}_{-0.02}$	-0.10	-0.10
$\pi_{E,N}$	$-0.08^{+0.06}_{-0.08}$	-0.14	-0.14	$-0.11^{+0.10}_{-0.09}$	-0.21	-0.21
$x_{S0,E}$ (mas)	$-104.56^{+0.12}_{-0.10}$	-104.62	-104.62	$-104.62^{+0.09}_{-0.09}$	-104.58	-104.58
$x_{S0,N}$ (mas)	$-183.61^{+0.13}_{-0.11}$	-183.53	-183.53	$-183.57^{+0.13}_{-0.14}$	-183.49	-183.49
$\mu_{S,E}$ (mas yr^{-1})	$-2.41^{+0.02}_{-0.03}$	-2.39	-2.39	$-2.40^{+0.02}_{-0.02}$	-2.43	-2.43
$\mu_{S,N}$ (mas yr^{-1})	$-7.26^{+0.03}_{-0.03}$	-7.26	-7.26	$-7.26^{+0.03}_{-0.03}$	-7.28	-7.28
$b_{SFF,O}$	$0.97^{+0.02}_{-0.02}$	0.98	0.98	$0.96^{+0.02}_{-0.03}$	0.96	0.96
$m_{base,O}$ (mag)	$18.41^{+0.005}_{-0.005}$	18.41	18.41	$18.41^{+0.005}_{-0.005}$	18.41	18.41
$b_{SFF,H8}$	$1.02^{+0.02}_{-0.03}$	1.04	1.04	$1.02^{+0.02}_{-0.03}$	1.04	1.04
$m_{base,H8}$ (mag)	$18.62^{+0.003}_{-0.003}$	18.61	18.61	$18.62^{+0.003}_{-0.003}$	18.62	18.62
$b_{SFF,H6}$	$1.02^{+0.02}_{-0.03}$	1.04	1.04	$1.02^{+0.02}_{-0.03}$	1.05	1.05
$m_{base,H6}$ (mag)	$21.34^{+0.006}_{-0.006}$	21.34	21.34	$21.34^{+0.006}_{-0.006}$	21.34	21.34
M_L ($M_\odot$)	$0.90^{+0.77}_{-0.47}$	0.83	0.83	$0.71^{+0.62}_{-0.34}$	0.58	0.58
π_L (mas)	$0.21^{+0.11}_{-0.06}$	0.28	0.28	$0.23^{+0.13}_{-0.07}$	0.35	0.35
π_{rel} (mas)	$0.11^{+0.10}_{-0.06}$	0.18	0.18	$0.12^{+0.13}_{-0.07}$	0.25	0.25
$\mu_{L,E}$ (mas yr^{-1})	$0.21^{+2.20}_{-1.30}$	0.22	0.22	$-0.16^{+1.67}_{-1.06}$	-0.30	-0.30
$\mu_{L,N}$ (mas yr^{-1})	$-4.79^{+2.45}_{-1.96}$	-3.22	-3.22	$-4.57^{+2.32}_{-2.31}$	-2.84	-2.84
$\mu_{rel,E}$ (mas yr^{-1})	$-2.61^{+1.30}_{-2.22}$	-2.60	-2.60	$-2.24^{+1.06}_{-1.69}$	-2.13	-2.13
$\mu_{rel,N}$ (mas yr^{-1})	$-2.46^{+1.97}_{-2.48}$	-4.04	-4.04	$-2.69^{+2.33}_{-2.34}$	-4.44	-4.44
θ_E (mas)	$0.90^{+0.66}_{-0.43}$	1.10	1.10	$0.87^{+0.55}_{-0.41}$	1.10	1.10
π_E	$0.12^{+0.06}_{-0.03}$	0.16	0.16	$0.14^{+0.08}_{-0.05}$	0.23	0.23
$\delta_{c,max}$ (mas)	$0.32^{+0.23}_{-0.15}$	0.39	0.39	$0.31^{+0.20}_{-0.14}$	0.39	0.39
$\sum w_i$		0.43			0.57	
$\log \mathcal{Z}$		24,631.66			24,631.92	

Note. Same as Table 9, but for OB110310.

Table 13
Lens/Source Resolvability

	Resolving Time t_{res} (yr)		Contrast (F_L/F_S)	
Parameter	F814W	F606W	F814W	F606W
MB09260	$32.08^{+19.38}_{-9.20}$	$23.88^{+14.42}_{-6.85}$	$0.01^{+0.03}_{-0.00}$	$0.00^{+0.01}_{-0.00}$
MB10364	$30.72^{+24.58}_{-12.19}$	$22.87^{+18.29}_{-9.07}$	$0.01^{+0.02}_{-0.00}$	$0.00^{+0.02}_{-0.00}$
OB110037	$17.45^{+6.92}_{-4.01}$	$12.99^{+5.15}_{-2.98}$	$0.10^{+0.07}_{-0.07}$	$0.20^{+0.08}_{-0.07}$
OB110310	$22.03^{+19.49}_{-6.66}$	$16.40^{+14.51}_{-6.66}$	$0.00^{+0.01}_{-0.00}$	$0.00^{+0.01}_{-0.00}$
OB110462 DW	$16.91^{+2.76}_{-1.89}$	$12.59^{+2.05}_{-1.41}$	$0.07^{+0.04}_{-0.04}$	$0.03^{+0.04}_{-0.00}$
OB110462 EW	$15.81^{+4.68}_{-3.06}$	$11.77^{+3.49}_{-2.27}$	$0.06^{+0.07}_{-0.05}$	$0.02^{+0.07}_{-0.00}$

Note. There are two entries for OB110462, one based on a fit with "default weighting" (OB110462 DW) and one based on a fit with "equal weighting" (OB110462 EW). See Section 5.3 for details.

summarized in Table 10. The inferred Einstein crossing time t_E is $61.11^{+0.24}_{-0.24}$ days, the microlensing parallax π_E is $0.27^{+0.01}_{+0.01}$, the Einstein radius θ_E is $0.46^{+0.31}_{-0.21}$, and the lens mass is $0.21^{+0.14}_{-0.10}\,M_\odot$.

MB10364 is a low-mass object, with the possibility of an NS or BH lens ruled out. The relative probabilities of star:BD:WD are 36:29:35.

7.4. OB110037

The data and model for OB110037 are shown in Figures 5 (photometry) and 17 (astrometry), and the fit posteriors are summarized in Table 11. The inferred Einstein crossing time t_E is $92.78^{+0.01}_{-2.60}$ days, the microlensing parallax π_E is $0.37^{+0.01}_{-0.01}$, the Einstein radius θ_E is $1.24^{+0.36}_{-0.35}$, and the lens mass is $0.41^{+0.12}_{-0.12}\,M_\odot$.

The probability that OB110037 has a dark lens is at least 26%, and the probability of a stellar lens is at most 74%. The relative probabilities of star:BD:WD:NS:BH are 74:0:26:0:0. Stellar lenses are only allowed below $0.6\,M_\odot$, and WDs are the only type of compact object allowed.

The light curve of OB110037 appears to have some type of perturbation at MJD $\sim$55,690. This feature is also apparent in the MOA light curve, raising our confidence that the light-curve feature is real. This perturbation may be attributed to a binary lens.

In addition, the astrometry fit, in particular for the F606W filter, is quite poor (Figure 17). Although the first five observations from 2011 to 2012 seem to agree between the two filters, a drastic difference that increases as time goes on begins from 2013 to 2017. This may be attributed to a binary source.
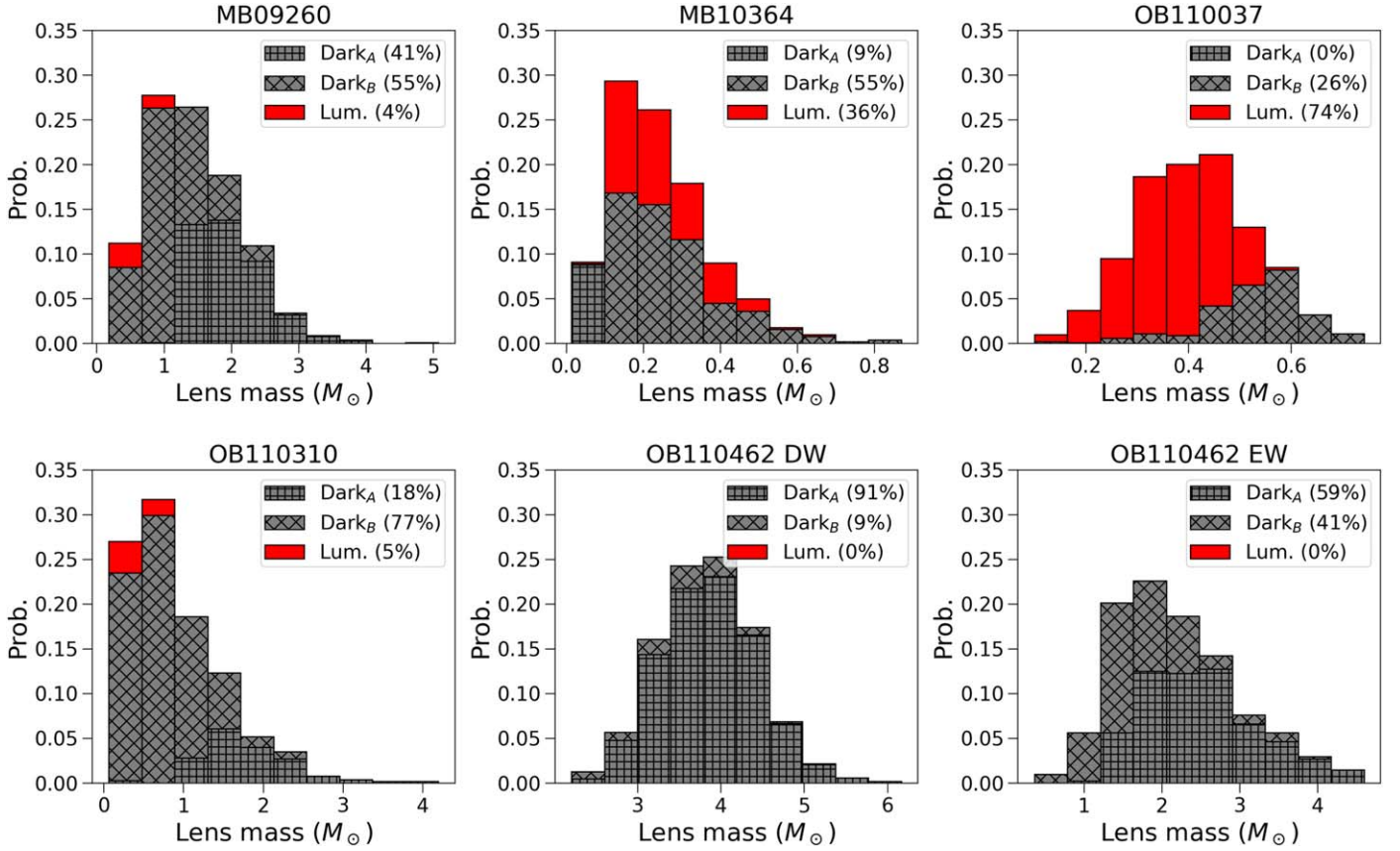
Figure 19. Probabilities for dark (gray) and luminous lenses (red), as a function of lens mass for each target. Lenses that are dark because all stars of that mass have already evolved and died (implying that they are compact objects) are subscribed with A (square hatch), while lenses that are dark because a star would be too bright to be hidden in the allowed lens flux are subscribed with B (diamond hatch). The probabilities for the luminous lenses are upper limits, while the probabilities for the dark lenses are lower limits, since the method described in Section 6 only places an upper limit on the brightness of the lens. Note that there are two fits for OB110462, one with equal weighting to the astrometry and photometry data (OB110462 EW) and one with the default weighting of the astrometry and photometry data (OB110462 DW). See Section 5.3 for details.

It is curious that the photometry may be better explained by a binary lens model, while the astrometry is likely better explained by a binary source model. Reanalysis of this event with both types of binary models would be a worthwhile and interesting pursuit, but it is beyond the current scope of this paper.

7.5. OB110310

The data and model for OB110310 are shown in Figures 6 (photometry) and 18 (astrometry), and the fit posteriors are summarized in Table 12. The inferred Einstein crossing time t_E is $82.64^{+2.18}_{-1.50}$ days, the microlensing parallax π_E is $0.13^{+0.08}_{-0.04}$, and Einstein radius θ_E is $0.88^{+0.61}_{-0.42}$, and the lens mass is $0.78^{+0.71}_{-0.39} M_\odot$.[34]

The probability that OB110310 has a dark lens is at least 95%, and the probability of a stellar lens is at most 5%. The relative probabilities of star:BD:WD:NS:BH are 5:3:65:22:5. Stellar lenses are only allowed below $1 M_\odot$. A WD or NS is the most probable type of lens, although BDs and BHs are still allowed at the low- and high-mass ends, respectively.
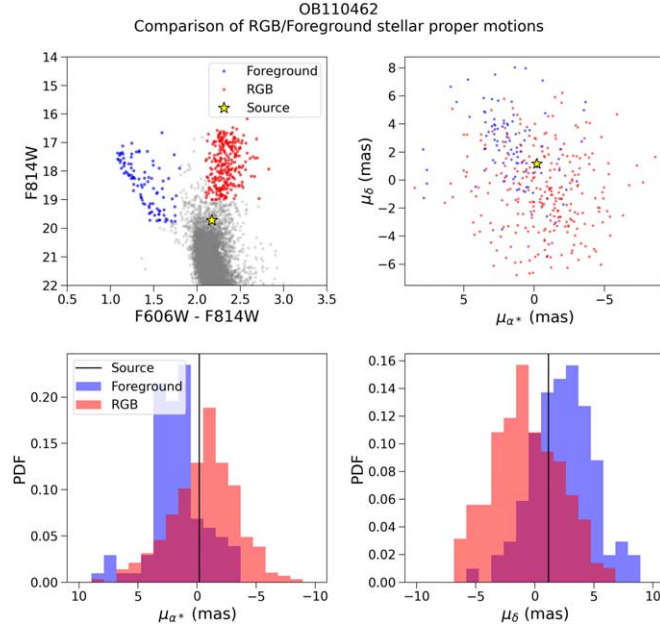
7.6. Source Properties Inferred from CMDs

As there is very little blending for all the targets in the high-resolution F814W and F606W filters ($b_{SFF} \sim 1$), the difference between the target and source on the CMD does not change much in color or magnitude space (ΔF814W $\lesssim 0.1$ mag and Δ(F606W − F814W) $\lesssim 0.1$ mag, Figure 2). Based on a CMD analysis, the source stars in MB09260, MB10364, OB110037, and OB110310 are likely red giant stars in the bulge, as is typical for microlensing events in this part of the sky.

The source of OB110462 in the CMD is around the main-sequence turnoff (MSTO) on the redder and more luminous side of the main sequence, suggesting that it is most likely a giant or subgiant star. However, a main-sequence source could still be consistent.

The region of the CMD around the MSTO contains both foreground stars from the disk and bulge stars. We compare the proper motions of OB110462's source to stars in the bright blue foreground and in the bulge red giant branch (RGB) to determine which population it most likely belongs to (Figure 20). The source is consistent with either population, although it falls within the bulk of the bulge population and more on the edge of the disk population; hence, we consider that it is most likely a bulge star. This is also consistent with the source parallax $\pi_S = 0.11 \pm 0.02$ inferred from the fit, which also indicates that the source is likely in the bulge.

---

[34] These are the values for the posteriors before they are split into modes, which is why the values differ from what is reported in Table 12. However, since these parameters are all globally unimodal, their distributions are nearly identical across modes within the uncertainties, and neither mode is strongly favored, the values are not very different and we report the global median and uncertainties.

Figure 20. Top left: CMD with the blue foreground and RGB stars marked. The source color and magnitude as inferred from the fit are shown as the yellow star. Top right: Vector point diagram of the foreground and RGB stars. The source proper motion as inferred from the fit is shown as the yellow star. Bottom left: histogram of the foreground and RGB R.A. proper motions. The proper motion of the source is shown with the black line. Bottom right: same as bottom left, but for decl. The source proper motion is consistent with either the foreground or RGB bulge population, although it falls closer to the bulk of the RGB population; hence, we consider that it is most likely a bulge star.

MB09260 and OB110310 are in the the most highly reddened field, OB110462 and OB110037 are in intermediately reddened fields, and MB10364 is in the least reddened field. This serves as a reminder that within the bulge the amount of extinction is highly variable, even over relatively small fields.

7.7. Verifying Fit Results with b_{SFF}

The fitting results are validated by comparing the best-fit OGLE or MOA I-band source flux fraction ($b_{SFF,O}$, $b_{SFF,M}$ in Tables 1 and 2 in the main paper, and Tables 9–12) to the high-resolution F814W HST images (Figure 12). We only compare the F814W images, as they have a similar effective wavelength to OGLE I band. Assuming a seeing disk radius of $\sim 0\farcs65$ for OGLE and $\sim 1\farcs25$ for MOA, we add up the flux from all stars detected by hst1pass within this radius around the target. Next, by assuming that all the flux from the microlensing target at baseline as seen by HST is due to the source (i.e., no flux from the lens or blended neighbor stars within HST's diffraction-limited aperture $\theta_{HST} \sim 0\farcs09$), we can estimate an upper limit on the source flux fraction for a given seeing disk radius $\theta_{see} > \theta_{HST}$ using

$$b_{SFF,HST-derived} \leqslant \frac{F_{event}}{\sum_i F_i},\qquad(33)$$

where F_i are the fluxes of the i stars within θ_{see} and F_{event} is the flux of the event at baseline in HST. This estimate on the upper limit of the source flux fraction derived using HST, $b_{SFF,O,HST-derived}$ or $b_{SFF,M,HST-derived}$, is compared to the values inferred from the light-curve fit, $b_{SFF,O}$ or $b_{SFF,M}$. This approach is sufficient to cross-check our results, considering that other differences prevent a perfect comparison (e.g., HST F814W is not a perfect match to the OGLE I filter).

From the photometry fits, MB10364 has $b_{SFF,M} \sim 0.93$, OB110037 has $b_{SFF,O} \sim 0.90$, OB110310 has $b_{SFF,O} \sim 0.97$, and OB110462 has $b_{SFF,O} \sim 0.05$, which are all below or no more than ~ 0.05 higher than the upper limits inferred from the HST-derived values shown in Figure 12.

MB09260 has $b_{SFF,M} \sim 0.60$, which is higher than the upper limit of $b_{SFF,HST-derived} \sim 0.4$ in F814W at $1\farcs25$ estimated from the high-resolution HST images. However, there is an abrupt transition from $b_{SFF,HST-derived} \sim 1$ to $b_{SFF,HST-derived} \sim 0.4$ (indicating a very bright star) at a radius of $1''$ from the source. The best-fit $b_{SFF,M} \sim 0.60$ falls within these two values, indicating that properly treating this situation by convolving the HST image with an MOA PSF would result in a better match. Hence, MB09260 seems consistent with the high-resolution image.

The consistency between the source flux fraction inferred from the fits and the high-resolution imaging provides an extra degree of confidence in the inferred fit values.

7.8. Prospects for Resolving Lens and Source

By definition, microlensing means that the source and lens are not resolvable. However, after many years, the lens and source can separate far enough to be resolved (e.g., Batista et al. 2015; Bennett et al. 2015). In the case of dark lenses, such as BHs, nondetections of the lens many years after the event can be used to place constraints on its properties (e.g., Abdurrahman et al. 2021). For the five targets in this paper, we provide estimates to determine whether and when taking late-time follow-up data would enable such analyses.

From the results of the fit, we can estimate the time necessary to resolve the source and lens t_{res} via

$$t_{res} = \theta_{res}/\mu_{rel},\qquad(34)$$

where the relative proper motion μ_{rel} comes from fitting the data, and the minimum angular separation θ_{res} can be estimated using the Rayleigh criterion. For HST with a mirror diameter of 2.4 m, θ_{res} corresponds to 63.53 mas in F606W and 85.35 mas in F814W.

Assuming that there are no contaminating stars, $b_{SFF} = F_S/(F_S + F_L)$. Then, the ratio of lens to source flux, in contrast, is $F_L/F_S = (1 - b_{SFF})/b_{SFF}$. Note that $b_{SFF} > 1$ are allowed by some of the fits, which would lead to an unphysical negative contrast. $b_{SFF} > 1$ is often referred to as "negative blending" because it means that there is negative nonsource flux (see Equation (25)). Negative blending can occur in ground-based images if the background subtraction is imperfect (Park et al. 2004). For HST, where the photometry is not derived from difference imaging but rather PSF fitting, this is unlikely to be the case. However, when fitting a microlensing model to data, negative blending can occur if $b_{SFF} \approx 1$, simply due to normal photometric uncertainties. This is the most likely explanation for HST; all fits with negative blending values have posterior probabilities that encompass $b_{SFF} = 1$. Thus, if a contrast value is negative, we cap it at 0.[35] In addition, the fit values for μ_{rel} and b_{SFF} are nearly independent, and so these results for t_{res} and F_L/F_S can be thought of as independent.

The resolving time after photometric peak and maximum contrast in the F814W and F606W HST filters for each target are listed in Table 13. Currently, only OB110037 could potentially have its source−lens pair resolved in F606W. All the other targets have lens−source resolving times at least 15 yr post-photometric peak or very low contrast. In addition, since they all have very high source flux fractions b_{SFF}, their lens −source contrasts are very low, which means that even after enough time has passed for the lens and source to separate, a luminous lens would be difficult to detect. Thus, high-resolution imaging of OB110037 in the near future could confirm the results of the fit if the separating source and lens could be detected. For the other targets, the absence of any lens detection would imply consistency with the results presented here but could not confirm them; however, any detection of a lens would imply that the fit results here are incorrect.

7.9. Number of Detected BHs

Next, we compare our observed BH yield to the theoretical expectation calculated using the PopSyCLE simulations. For a sample of simulated events that would be observable by OGLE (see Table 4 of Lam et al. 2020), we calculate the fraction of those events due to BHs as a function of the Einstein crossing time t_E. Assuming the OGLE observability criterion for the MOA sample is not strictly correct; however, OGLE and MOA often observe an overlapping set of events, so this approximation suffices.

We wish to calculate the probability of detecting k BHs in our sample given n events, where the probability of detecting a BH in the ith event is p_i. This is described by a Poisson binomial distribution, which characterizes a "success/no success" experiment with n independent trials, where the ith trial has probability p_i of success (Wang 1993). The probability of k successes is given by

$$P(K = k) = \sum_{A \in F_k} \prod_{i \in A} p_i \prod_{j \in A^c} (1 - p_j), \qquad (35)$$

where F_k is the set of all subsets of k integers that can be selected from the set $\{1,...,n\}$, i.e.,

$$F_k = \{A: A \subseteq \{1,...,n\}, |A| = 0, 1,...,n\}.$$

$|A|$ is the number of elements in A, and A^c is the complement of A. In the limit where all p_i are equal, the Poisson binomial distribution is equivalent to the ordinary binomial distribution.

In our case, there are $n = 5$ independent trials (i.e., microlensing targets). We calculate the probability of success p_i (i.e., BH detection) using PopSyCLE. We define the success probability for the ith target as the fraction of BH lensing events in PopSyCLE over the range of t_E inferred from the fit

$$\text{med}(t_E) - 3\sigma < t_E < \text{med}(t_E) + 3\sigma.$$

The probabilities of BH detection for each target are listed in Table 14.[36]

The results of evaluating Equation (35) for $k = 0,...,5$ BH detections assuming success probabilities p_i are presented in Figure 5 in the main paper. PopSyCLE's Galactic model contains 2×10^8 BHs ranging from 5 to $16\,M_\odot$ (Lam et al. 2020). There are no $2-5\,M_\odot$ mass-gap NSs or BHs in the simulation, and hence no exact OB110462 analog. Thus, we consider a mass-gap detection as falling between zero and one BH detection. The probabilities of detecting zero and one BH are $\sim25\%$ and $\sim40\%$, respectively. This estimate is consistent with our single detection of a NS–BH mass-gap object.

8. Discussion in Detail

OB110462 is the first definitive detection of a compact object discovered with astrometric microlensing. Depending on the fit, it is either an NS (50% probability for the EW fit), a BH (44% probability for the EW fit, 100% probability for the DW fit), or a WD (6% probability for the EW fit). MB09260 and OB110310 are mostly likely WDs or NSs, although an NS–BH mass-gap object cannot be ruled out. MB10364 and OB110037 are definitively low-mass objects; OB110037 is most likely a star or WD, while MB10364 is either a star, BD, or WD.

Discussion of the BH yield as compared to theoretical expectations is found in Section 5 of Lam et al. (2022). Here we discuss in more detail our sample of BH candidates and the questions it raises about the Galactic BH population (Section 8.1), additional observations of OB110462 (Section 8.2), potential sources of systematics in OB110462 observations (Section 8.3), and the future of BH microlensing searches (Sections 8.4 and 8.5).

8.1. OB110462 in Comparison to the BH Population

8.1.1. Low-mass X-Ray Binaries

Several attempts have been made to determine the Milky Way BH mass function using dynamical mass measurements of BHs in low-mass X-ray binaries (LMXBs). Using a sample of seven LMXBs, Bailyn et al. (1998) found the BH mass function to be tightly centered around $7\,M_\odot$, with a dearth of

---

[35] This is technically not correct, analogous to truncating negative parallaxes in Gaia; a proper treatment would involve a full Bayesian analysis as explained in Luri et al. (2018). Such a treatment is beyond the scope of this paper. We proceed with capping the contrast at 0, since if $b_{SFF} \sim 1$, then the target is likely very dim or dark, and the contrast is unlikely to be detectable.

[36] The fact that BH probability does not increase monotonically as a function of t_E appears to contradict the claims made in the main paper that events with longer t_E are more likely to have a BH lens. The issue is that the uncertainty in BH probability rapidly increases at longer t_E, as the number of events steeply drops off for $t_E \gtrsim 50$ days (Figure 6 in the main paper). For example, for both OB110462 solutions, the estimates are based on < 10 events. Because of the small number of events, the estimate is highly sensitive to the particular t_E range.

systems between 3 and 5 $M_\odot$; they argued that this dearth was not due to observational selection effects. Later work by Özel et al. (2010) and Farr et al. (2011) using samples of 15–16 LMXBs found similar results, providing further support to the idea of the NS–BH mass gap. However, Kreidberg et al. (2012) cautioned that systematic errors in the analysis of LMXB systems could push their inferred masses high, artificially creating the mass gap, and Jonker et al. (2021) identified potential observational biases that prevent measurement of high-mass LXMB systems. Additionally, LXMBs occupy a very small and specific part of BH evolutionary parameter space, and the BHs found in those systems are likely not representative of the Galactic BH population as a whole.

8.1.2. Filling the NS–BH Mass Gap

Measurements of BH masses in non-LMXB systems do not show evidence of a mass gap. Gravitational wave searches have found mass-gap objects both as the merger remnant ($\sim 3\,M_\odot$ in GW170917, Abbott et al. 2017; $\sim 3.4\,M_\odot$ in GW190425, Abbott et al. 2020a) and in the merger components ($\sim 2.6\,M_\odot$ in GW190814; Abbott et al. 2020b). Noninteracting mass-gap BHs of $\sim 3\,M_\odot$ with red giant companions have also been detected in the Milky Way (Thompson et al. 2019). With a mass of 1.6–4.4 $M_\odot$, the lens of OB110462 is the first measured isolated Galactic NS or mass-gap BH. These detections of mass-gap objects will improve our theoretical understanding of compact object formation channels.

8.1.3. A Lack of Higher-mass BH Systems?

In order to gain a full understanding of the Galactic BH population, BHs must be uncovered outside of closely interacting X-ray binary systems.

We first consider searches for isolated BHs using microlensing, as discussed in this paper. From our sample of five events, we have a single detection of a mass-gap object; all other lenses are lower-mass non-BH detections. In addition, we have a single detection of a >1 mas astrometric shift; most of the remaining detections are at the ~ 0.5 mas level, near the limit of HST's precision. As discussed in Section 5.1 of Lam et al. (2022), the low yield of BHs in this sample is consistent with predictions by Galactic models. However, this presents tentative evidence that Galactic BHs may be less massive than the $\sim 10\,M_\odot$ expectation. If the BH mass function truly peaks at 8 $M_\odot$, then selecting candidates via long-duration microlensing events should doubly bias us toward finding these high-mass lenses. First, the lensing cross section $\sigma = \pi\theta_E^2$ is proportional to the mass of the lens M_L, since $\theta_E \propto \sqrt{M_L}$. Thus, more massive objects are more likely to be microlenses. Second, the Einstein crossing time is proportional to the square root of the lens mass, $t_E \propto \sqrt{M_L}$. Thus, long-duration events are also more likely to be due to massive microlenses.

Next, we consider searches for BHs in detached/noninteracting binary systems. The mass function f of a single-lined spectroscopic binary is given by

$$ f = \frac{P_{orb} K^3 (1 - e^2)^{3/2}}{2\pi G} = \frac{M_2^3 \sin^3 i}{(M_1 + M_2)^2}, \quad (36) $$

where P_{orb} is the orbital period, K is the radial velocity (RV) semiamplitude, e is the orbital eccentricity, i is the orbital inclination, M_1 is the mass of the visible component, and M_2 is the mass of the unseen component. If measurements of P_{orb}, K, e, and

M_1 can be obtained, then a minimum mass on M_2 can be derived. If $M_2 > 5\,M_\odot$ without evidence of luminosity, the unseen system is inferred to be a BH. Since systems with larger RV semiamplitudes have larger mass functions, they are most likely to host unseen BH companions. To date, searches for large RV semiamplitudes in spectroscopic catalogs have detected an object that falls within the mass gap, but no $\sim 10\,M_\odot$ BHs, which suggests a paucity of higher-mass systems (Thompson et al. 2019; El-Badry et al. 2022). Complementary searches using ellipsoidal variables (Rowan et al. 2021) also suggest that higher-mass systems are rare.

Although both microlensing and RV searches should be biased toward finding $10\,M_\odot$ objects more easily than $3\,M_\odot$ objects, only the latter are being detected. It may be that the selection bias for massive objects is canceled out by the fact that the mass function of stars, WDs, NS, and BHs sharply decreases from low to high mass. Additional work to quantify and compare these two competing effects, combined with larger sample sizes, will be needed to understand the Galactic BH mass function.

Finally, astrometric searches for detached binaries are also eagerly anticipated with Gaia (e.g., Yalinewich et al. 2018; Yamaguchi et al. 2018; Wiktorowicz et al. 2020). It will be very fruitful to compare the results of those searches to the X-ray transient, microlensing, and RV searches.

8.2. Auxiliary OB110462 Observations

Additional observations of OB110462 may assist in ascertaining its NS or BH nature. Here we describe planned observations of OB110462, as well as data found in searches of archival catalogs.

The 2021 astrometric observations of OB110462 are crucial to the modeling, as they extend the temporal baseline of the original archival observations by 50%, from 6 to 10 yr. The remaining data from HST Cycle 29 program GO-16760 to be taken in the fall of 2022 (Lam & Lu 2021) will further extend the baseline by another year and improve the characterization of the astrometric signal. The astrometric microlensing shift is a deflection with respect to the unlensed position of source (Equation (27)), and we can only have confidence in our measurement of that shift if we also have confidence in our measurement of the source's unlensed proper motion. The astrometric shift due to lensing when $u \gg 1$ can be approximated as $\delta_c \approx \theta_E t_E / (t - t_0)$ (see Appendix D). For OB110462 ($t_E = 280$ days and $\theta_E = 4$ mas), the microlensing astrometric shift did not dip below HST's astrometric precision of ~ 0.3 mas until 2021, 10 yr after source–lens closest approach. This calculation illustrates the importance of having a long temporal baseline for OB110462 in order to properly measure the source's unlensed proper motion and characterize the astrometric microlensing signal.

Additional follow-up observations in the X-ray can place limits on accretion from the ISM (Agol & Kamionkowski 2002). For example, Maeda et al. (2005) and Nucita et al. (2006) looked for X-rays at the location of BH microlensing candidate MACHO-96-BLG-5 reported in Bennett et al. (2002), using ACIS on Chandra and EPIC on XMM-Newton, respectively. Neither detected any X-rays.

We searched several X-ray catalogs that have observed at OB110462's coordinates to determine whether there are any

Table 14
Fraction of Expected BH Detections vs. t_E from `PopSyCLE` Simulation

Target	t_E Range	% BH
MB09260	135 days $< t_E <$ 155 days	50
MB10364	60 days $< t_E <$ 62 days	14
OB110037	87 days $< t_E <$ 100 days	12
OB110310	78 days $< t_E <$ 90 days	20
OB110462 DW	266 days $< t_E <$ 300 days	17
OB110462 EW	256 days $< t_E <$ 325 days	14

Note. For each target, the t_E range is the median $\pm 3\sigma$. For OB110462 there are two entries, one with equal weighting to the astrometry and photometry data (OB110462 EW) and one with the default weighting of astrometry and photometry data (OB110462 DW). See Section 5.3 for details.

coincident sources. OB110462 was not detected as an X-ray source in any of the following catalogs:

1. Chandra Source Catalog 2.0[37] (Evans et al. 2019a, 2019b). The limiting sensitivity provides an upper limit of 1.91×10^{-14} erg s^{-1} cm^{-2} at 0.5–7.0 keV.
2. XMM-Newton Science Archive[38] (Sarmiento et al. 2019). This provides an upper limit of 1.52×10^{-14} erg s^{-1} cm^{-2} and $<1.38 \times 10^{-3}$ counts s^{-1} at 0.2–12.0 keV.
3. Swift XRT Point Source Catalogue[39] (Evans et al. 2020). This provides an upper limit of 2.4×10^{-3} counts s^{-1} at 0.3–10 keV.

OB110462's coordinates are not in the eROSITA-DE Early Data Release catalog.[40]

We also searched the Australia Telescope National Facility Pulsar Catalogue[41] (Manchester et al. 2005) version 1.65 for any pulsars coincident with the target. There are no coincident pulsars; the nearest pulsar is 0°.55 away.

As mentioned in Section 3.5, OB110462 is not in the Gaia EDR3 catalog. OB114062's baseline magnitude is F606W ≈ 22, while Gaia's nominal magnitude limit is $G \approx 20.7$ and will be even brighter in crowded regions (Fabricius et al. 2021).

8.3. Potential Systematics in OB110462 Observations

We briefly discuss whether the tension between the photometry and astrometry could be due to systematics in the data.

First, we consider the OGLE photometry. For such a long temporal baseline, possible sources of systematic error include differential refraction, proper motion, or low-level stellar variability. However, no trends due to proper motion or stellar variability are seen in the light curve. In addition, the F814W − F606W color of the bright star within $\sim0''.3$ of OB110462 that are blended together in the OGLE images are within 0.1 of each other, and hence effects due to differential refraction would be undetectable. We also inspect the light curves of several stars near OB110462 that have similar magnitude to the baseline magnitude of OB110462. No trends can be seen that resemble the residuals in the EW fit. In addition, we explored rescaling the photometric uncertainties of the OGLE data; however, even

inflating all uncertainties by a factor of ~2 did not significantly change the structure of the residuals or the inferred microlensing parameters, including lens mass.

Potential sources of systematics in the HST astrometry are discussed in the next section.

8.4. Improving Experimental Strategy and Design

8.4.1. Multifilter Astrometry

In contrast to photometric observations, multifilter astrometry is not routinely obtained, as astrometric observations are expensive and facilities with the requisite precision are rare. This is one of the first projects to explore the impact of different filters on relative astrometry. The nature of the difference between F606W and F814W filter astrometric observations of OB110037 and OB110462 is an open question, whether it be astrophysical (e.g., binaries sources with different color), systematic (e.g., uncorrected CTE), or statistical. However, it demonstrates that multifilter observations are worth continuing to pursue in future astrometric microlensing studies. For example, it could help break degeneracies between certain types of binaries lenses or sources.

8.4.2. CTE Correction

As mentioned in Section 4.1, the CTE correction in the `_flc` files is not perfect. Future pursuits will explore other methods of correction, such as a re-analysis of OB110462 that uses the newer and more accurate tabular correction for CTE (Anderson 2021). In addition, trying to fix CTE via a magnitude-dependent astrometric alignment is another avenue that is being explored.

8.4.3. Observational Strategy

For these precise astrometric measurements, taking good observations is critical. The lens mass constraints for several of the targets are only upper limits, as the astrometric shifts were so small as to be undetectable at the precision of the measurements. A dominant source of astrometric uncertainty with HST WFC3-UVIS observations is the undersampling of the PSF. It has been shown that there is a floor in the astrometric precision that can be achieved, even at high signal-to-noise ratio, when only a few exposures are used (Hosek et al. 2015). As the majority of the observations in each filter had four or fewer exposures, this limited the achievable astrometric precision for several of the targets, in particular OB110462. Increasing the number of exposures and implementing small uncorrelated dithers to sample different pixel phases can reduce this floor as $\sqrt{N_{\mathrm{dithers}}}$.

In addition, the effects of CTE are worsening with time. Actively mitigating CTE through careful planning of observations rather than trying to correct it afterward is even more important than before (e.g., as described in Section 7 of Anderson et al. 2021).

8.4.4. Event Selection

Although all events presented in this work were selected to have $t_E > 200$ days (Sahu 2009), the inferred t_E values for four of the five events did not satisfy this criterion. As a result, the true t_E range probed extended down to $t_E = 60$ days and did not sample the t_E range that maximizes the expected yield of BHs ($t_E \gtrsim 100$ days). Only MB09260 and OB110462 had $t_E > 100$ days, weakening the constraints on the BH fraction. We are currently attempting to determine whether prediction of t_E

---

37 https://cxc.harvard.edu/csc/
38 http://nxsa.esac.esa.int/nxsa-web/#search
39 https://www.swift.ac.uk/2SXPS
40 https://erosita.mpe.mpg.de/edr/
41 https://www.atnf.csiro.au/research/pulsar/psrcat/

before the photometric peak of the event could be improved. If possible, this would enable improved selection of BH candidates for astrometric follow-up.

A secondary concern is the target field itself. A sufficient number of reference stars are needed; hence, the field in the immediate vicinity of the target must be sufficiently crowded. However, the magnitude range of those nearby stars must also be similar to the target. Because of the steepness of the luminosity function, bright targets or targets with high magnification are more difficult to analyze, as they lack sufficient reference stars to perform relative astrometric alignment. This is in tension with the need to have high photometric precision in order to precisely measure the microlensing parallax. Although bright and highly magnified stars should still be followed up if they are long-duration events, special care must be taken when designing observations to ensure good astrometric alignment.

8.5. BH Searches with the Roman Space Telescope

Although the initial idea and subsequent design requirements for the Roman Space Telescope (hereafter Roman) microlensing survey are driven by exoplanet searches (Penny et al. 2019), it also hails the next generation of astrometric microlensing campaigns searching for BHs. Currently, each event must be followed up individually, with only two facilities (HST and Keck) capable of the precision in the near-infrared required to make such a measurement. Such measurements are expensive (requiring approximately an orbit of HST or $\sim$1 hr of Keck time per measurement), prohibiting dense astrometric temporal sampling or a large sample of targets.

Roman will change this with its ability to simultaneously obtain precise photometry and astrometry over a wide FOV $100\times$ the area of HST and astrometric precision almost an order of magnitude better than HST (Spergel et al. 2015; WFIRST Astrometry Working Group et al. 2019). This will also allow the masses of NS–BH mass-gap objects to be precisely measured and allow a sample of 100–1000 BH candidates to be built up over the duration of the survey (Lam et al. 2020). In addition, Roman will probe a large sample of shorter t_E events that will place constraints on BH kicks.

To make Roman as effective as possible for finding BHs, there are several considerations that need to be addressed. Due to the placement of the observatory's solar panels, which dictates the available pointings of the telescope, the Galactic bulge can only be observed twice a year during a 72-day window centered on the vernal and autumnal equinoxes. In addition, for Roman's planned 5 yr mission, only 6 of the 10 available bulge seasons are to be dedicated to the microlensing survey. These large temporal gaps are generally not a concern for exoplanets searches, as the transient portion of the light curve is nearly covered within the 72-day window. However, for long-duration events where the transient portion of the light curve is much longer than the window and where a measurement of small microlensing parallax is crucial, incomplete light-curve coverage will mean the difference between a confirmed BH mass measurement and only an upper limit. Observations filling in these gaps will be crucial. Collaboration with a ground-based telescope to provide imaging during the gaps, or smaller independent follow-up efforts, would be very important.

Appendix A
Rescaling of Uncertainties

For each epoch, `hst1pass` returns the rms error of extracted source positions and magnitudes over multiple frames σ_x, σ_y, and σ_m, respectively. Following Hosek et al. (2015), instead of using the rms errors for our uncertainties, we use the error on the mean $\sigma/\sqrt{N}$, where N is the number of frames the star is detected in, inflated with a empirical additive error. The empirical constant additive error on the positions Δ_{xy} and magnitudes Δ_m is calculated for each epoch and added in quadrature to the error on the mean. This produces the final rescaled uncertainties used in the analysis

$$\sigma_x' = \sqrt{\sigma_x^2/N + \Delta_{xy}^2} \tag{A1}$$

$$\sigma_y' = \sqrt{\sigma_y^2/N + \Delta_{xy}^2} \tag{A2}$$

$$\sigma_m' = \sqrt{\sigma_m^2/N + \Delta_m^2}. \tag{A3}$$

To determine Δ_{xy} and Δ_m, a sample of bright, unsaturated stars are selected. The exact magnitude range constituting "bright" is roughly saturation to 3–5 mag fainter, with the exact range determined empirically through the astrometric alignment process. In this sample, the additive error is selected such that the χ^2 distribution of the reference stars' position and magnitude fits is roughly consistent with the expected distribution (Figure 9). The resulting values are listed in Table 15. Note that for MB09260 F606W the same additive magnitude error was used across all epochs.

Table 15
Additive Errors for HST Data

Epoch (yyyy-mm-dd)	Pos. Error (mas)		Mag. Error (mmag)	
	F814W	F606W	F814W	F606W
MB09260				
2009-10-01	⋯	0.21	⋯	4.0
2009-10-19	0.12	⋯	3.2	⋯
2010-03-22	0.14	⋯	4.9	⋯
2010-06-14	0.14	⋯	6.1	⋯
2010-10-20	0.13	⋯	9.2	⋯
2011-04-19	0.14	0.36	12.8	4.0
2011-10-24	0.15	0.23	4.0	4.0
2012-09-25	0.15	0.27	4.3	4.0
2013-06-17	0.16	0.28	9.8	4.0
MB10364				
2010-09-13	0.14	1.61	8.6	11.6
2010-10-26	0.14	0.49	4.5	8.6
2011-10-31	0.17	0.26	5.9	5.0
2012-09-25	0.18	0.26	8.5	6.1
2013-10-24	0.17	0.25	6.8	5.8
OB110037				
2011-08-15	0.11	0.22	16.0	8.5
2011-09-26	0.11	0.18	4.1	14.0
2011-11-01	0.10	0.21	4.0	3.8
2012-05-07	0.10	0.26	12.9	12.2
2012-09-25	0.10	0.22	6.7	4.3
2013-10-21	0.10	0.23	3.9	4.9
2014-10-26	0.10	0.21	4.2	9.7
2017-03-13	0.10	0.21	4.9	5.1
2017-09-04	0.11	0.21	8.5	19.6

Table 15
(Continued)

Epoch (yyyy-mm-dd)	Pos. Error (mas)		Mag. Error (mmag)	
	F814W	F606W	F814W	F606W
OB110310				
2011-09-21	0.10	0.20	9.3	12.9
2011-10-31	0.12	0.30	4.2	4.9
2012-04-24	0.13	0.30	10.0	24.3
2012-09-24	0.14	0.29	10.2	10.9
2013-10-21	0.13	0.29	4.3	6.3
2017-03-14	0.13	0.31	4.1	18.8
2017-09-01	0.14	0.32	10.0	24.9
OB110462				
2011-08-08	0.13	0.41	18.1	17.0
2011-10-31	0.19	0.37	3.9	5.4
2012-09-09	0.19	0.36	4.7	7.2
2012-09-25	0.19	0.36	6.8	7.2
2013-10-22	0.19	0.36	3.6	4.8
2014-10-26	0.19	0.39	3.8	10.7
2017-08-29	0.20	0.40	5.4	14.7
2021-10-01	0.17	0.36	7.5	12.9

As mentioned in Section 4.2.1, for the five microlensing targets, the rms and rescaled astrometric uncertainties are generally similar. However, adopting an additive error makes the resulting astrometric uncertainties more uniform across the field, particularly for bright stars. This is critical, as these uncertainties are used as weights in the astrometric alignment (Section 4.2.3 and Figure 9). The reference stars' uncertainties are used to determine how good the reference frame transformation is, which is ultimately used to measure the astrometry of the target.

Appendix B
Injection and Recovery Tests

We use the `ks2` software (Anderson et al. 2008; Bellini et al. 2018; see also Section 3 of Sabbi et al. 2016 for a detailed description) to inject artificial stars into the OB110462 HST images to determine how well we can recover the magnitudes and positions of faint sources near bright sources. Injection and recovery tests are performed for all OB110462 epochs in two different manners:

1. Sources are injected radially around the bright neighbor star at the radius of OB110462 at a variety of azimuths excluding the azimuth of OB110462 itself, as we cannot recover a source planted on top of a real star.
2. Sources are injected near a star of similar brightness to the neighbor, in the same radial and azimuthal configuration relative to the star as OB110462 relative to the bright neighbor.

The first test directly probes the region around the neighbor itself but excludes the actual position of the OB110462, while the second test probes a region around a star similar to the neighbor, at the same separation and angle of OB110462 relative to the neighbor.

The star we dub "the neighbor" is ∼10 pixels (∼0″.4) west of OB110462. The star we dub "the neighbor-like star" in F814W
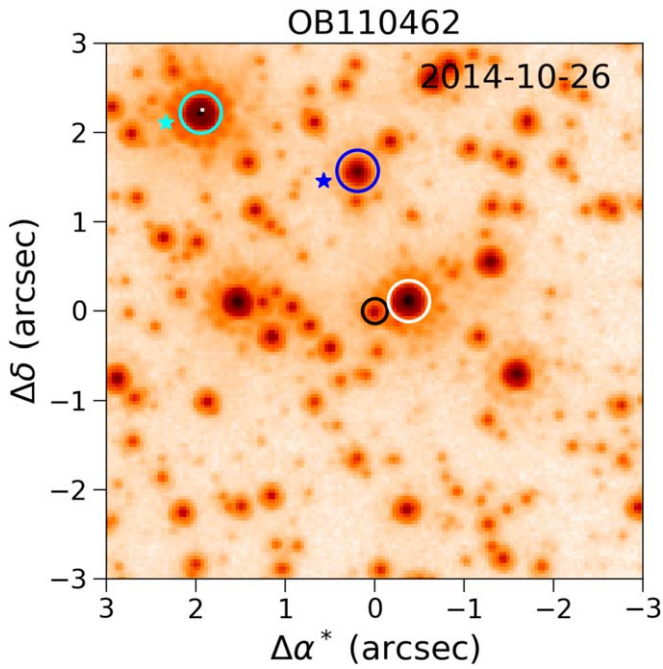
Figure 21. Injection and recovery for OB110462. Black circle, center: OB110462. White circle: the bright neighbor. Blue circle: neighbor-like star for F606W. Cyan circle: neighbor-like star for F814W. Positions where stars are injected in reference to the neighbor-like star are shown as blue and cyan stars (F606W and F814W, respectively).

is ~75 pixels (~3″) northeast of OB110462; for F606W the neighbor-like star is ~40 pixels (~1″.6) north of OB110462 (Figure 21).

In summary, both methods produce similar results (Figures 22 and 23). We use the single-azimuth results from injection around the neighbor-like star in order to capture any azimuthal dependence that would be lost by averaging over multiple azimuths (Table 16).

In F814W, the bias is negligible in the first epoch, when the target is magnified and is of similar brightness to the neighbor. However, in later epochs once the target is no longer magnified, the measured position of the target is biased by ~0.4 mas toward the bright neighbor star along the target–neighbor separation vector. The magnitude and direction of the positional offset are comparable across the two approaches, except in 2014, where the injection around the neighbor-like star leads to a larger difference than when injecting around the neighbor. The uncertainties are larger in the approach of planting around the neighbor, as it averages over more azimuths and results in a larger uncertainty.

In F606W, the bias is smaller than F814W because the shorter wavelength results in higher resolution. Like F814W, the bias is also negligible in the first epoch and around ~0.25 mas in later epochs. The uncertainties are also larger when averaging across many azimuths. Unlike F814W, the bias is mixed between radial and azimuthal components when injecting around the neighbor-like star at a single azimuth.

B.1. Injection around the Neighbor

For each epoch, we determine the separation r of OB110462 and the bright neighbor. We inject three rings of stars surrounding the bright neighbor, of radii $r - 0.2$, r, and $r + 0.2$ pixels. Each ring consists of 24 evenly spaced stars, resulting in one star every 15°. Because we cannot recover stars injected on top of the target itself, we do not attempt to recover injected stars that fall within 4
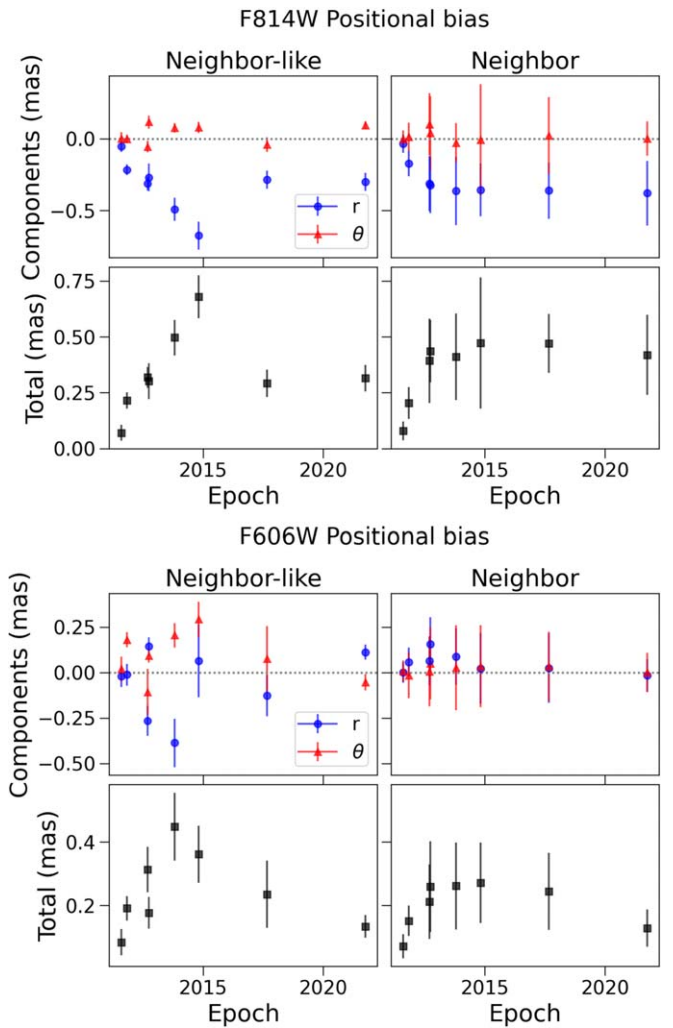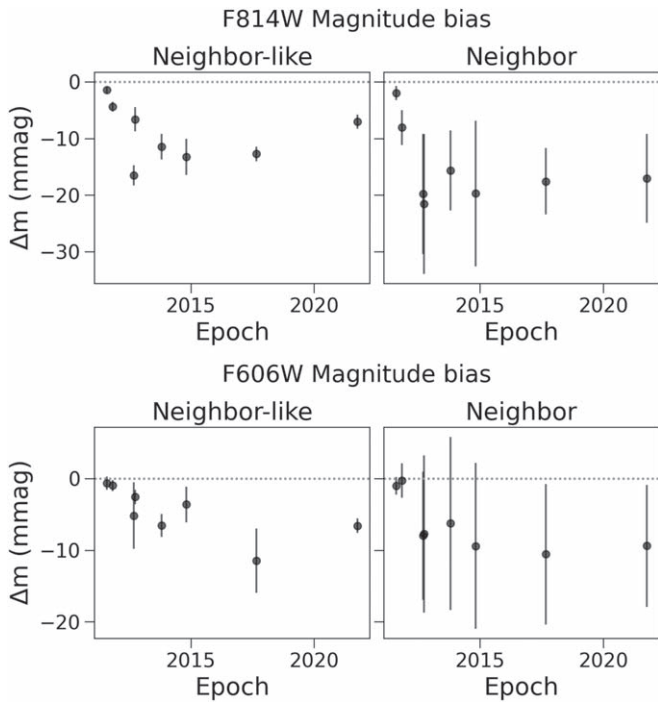

Figure 22. Positional bias in F814W (top panel) and F606W (bottom panel) as calculated from injection and recovery tests, injecting around a neighbor-like star (left column) or around the neighbor (right column). The positional bias (position recovered minus the true position input) is shown as a function of radial r and azimuthal θ components (top row), as well as total positional bias (bottom row).

pixels of the target itself; this excludes three of the positions. We thus inject a total of $(24 - 3) \times 3 = 63$ stars per epoch.

B.2. Injection around the Neighbor-like Star

The neighbor-like star we inject around is different for F814W and F606W because the surrounding stars do not have the same colors as the neighbor and target. The neighbor-like stars were chosen to have similar magnitude and saturation level to the neighbor. In F814W, the neighbor tended to be saturated; the F814W neighbor-like star is also saturated. On the other hand, in F606W the neighbor was not saturated, and the F606W neighbor-like star is also not saturated. The F814W neighbor-like star is brighter than the neighbor in F814W by ~0.6 mag, and the F606W neighbor-like star is fainter than the neighbor in F606W by ~0.5 mag.

In each epoch, we inject three arcs of radii $r - 0.2$, r, and $r + 0.2$ pixels centered on the neighbor-like star, where r is the target–neighbor separation (~10 pixels). Each arc consists of 15 stars at the azimuth of the target relative to the neighbor ± 0.2 pixels/(target–neighbor separation in pixels), which corresponds to a subtended angle of approximately 2°.2.

Figure 23. Magnitude bias in F814W (top panel) and F606W (bottom panel) as calculated from injection and recovery tests, injecting around a neighbor-like star (left column) or around the neighbor (right column). The magnitude bias is defined as the magnitude recovered minus the true magnitude input.

This corresponds to a region of ~ 0.04 pixels^2 where $3 \times 3 \times 15 = 135$ stars are injected.

At each position we inject stars of magnitude $m_I - 0.1$, m_I, and $m_I + 0.1$, where m_I is the magnitude that results in the same contrast with the neighbor-like star as OB110462 to the neighbor. That is, if OB110462 has magnitude m_T and the neighbor m_N, and the injected star is m_I around the neighbor-like star m_C, then $m_T - m_N = m_I - m_C$.

B.3. Recovery of Injected Sources

After planting fake stars into the image, we determine how well we can recover the positions and magnitudes. To match the properties of our original data set, we consider stars to be recovered if they are detected in at least N frames, where N is the number of frames that were used to calculate the position of the source. Iterative 3σ clipping is performed to exclude outliers due to confusion, e.g., from the diffraction spike mask. We then use the transformation parameters derived for this epoch (as described in Section 4.2.1) to convert from (x, y) pixel positions to (R.A., decl.) coordinates.

We define a polar coordinate system with the origin located at the neighbor star for the analysis in Section B.1 and located at the neighbor-like star for the analysis in Section B.2. The azimuthal direction is measured counterclockwise from the origin–OB110462 separation vector. The average offsets in the radial and azimuthal directions are r and θ (Figures 22 and 23).

The colors of the neighbor and OB110462 are very similar (F606W–F814W = 2.25 and 2.15, respectively). At baseline, the neighbor is about 3.1 mag brighter than OB110462. During magnification in the first epoch (2011 August 08), the neighbor is only about 0.4 mag brighter. Since the resolution is higher at shorter wavelengths, it is not unexpected that the positional bias is less in F606W than in F814W, since the separation is the same in both filters. It is also not surprising that the bias is

Table 16
Bias Correction Derived from Injection and Recovery

Epoch (yyyy-mm-dd)	ΔR.A. (mas)	ΔDecl. (mas)	ΔMag (mag)
F606W			
2011-08-08	-0.025 ± 0.001	0.012 ± 0.001	-0.001 ± 0.000
2011-10-31	-0.068 ± 0.002	0.168 ± 0.002	-0.001 ± 0.000
2012-09-09	-0.216 ± 0.001	-0.185 ± 0.001	-0.005 ± 0.000
2012-09-25	0.108 ± 0.002	0.136 ± 0.001	-0.003 ± 0.000
2013-10-22	-0.431 ± 0.001	0.070 ± 0.001	-0.007 ± 0.000
2014-10-26	-0.033 ± 0.001	0.298 ± 0.001	-0.004 ± 0.000
2017-08-29	-0.144 ± 0.001	0.032 ± 0.001	-0.011 ± 0.000
2021-10-01	0.124 ± 0.002	-0.014 ± 0.001	-0.007 ± 0.000
F814W			
2011-08-08	-0.049 ± 0.000	-0.014 ± 0.000	-0.001 ± 0.000
2011-10-31	-0.203 ± 0.001	-0.070 ± 0.001	-0.004 ± 0.000
2012-09-09	-0.278 ± 0.001	-0.150 ± 0.001	-0.016 ± 0.000
2012-09-25	-0.292 ± 0.001	0.025 ± 0.002	-0.007 ± 0.000
2013-10-22	-0.490 ± 0.001	-0.081 ± 0.001	-0.011 ± 0.000
2014-10-26	-0.665 ± 0.001	-0.138 ± 0.001	-0.013 ± 0.000
2017-08-29	-0.258 ± 0.001	-0.129 ± 0.001	-0.013 ± 0.000
2021-10-01	-0.315 ± 0.000	-0.001 ± 0.001	-0.007 ± 0.000

Note. Bias correction derived from injection/recovery around a star of comparable brightness at the same separation, azimuth, and magnitude difference as the target to its bright neighbor.

smallest in the first epoch when the magnitude difference between OB110462 and the neighbor is small and larger in the remaining epochs when the magnitude difference is large.

Appendix C
Absolute Proper-motion Reference Frame

The HST astrometry in Section 4.2 is derived in a procedure where the average motion of the stars is at rest with respect to the reference frame. To interpret the lens's proper motion or transverse velocity, we must place the relative astrometry into an absolute reference frame. To do this, we calculate the proper-motion offset between stars in the relative HST frame and the absolute Gaia frame. We match all stars in the Gaia EDR3 catalog within $1'$ of the target that have `astrometric_excess_noise_sig < 2` and a proper-motion measurement (i.e., five-parameter and six-parameter solutions) to the bright stars in our HST proper-motion catalog (F814W < 22 for MB10364 and OB110037; F814W < 23 for MB09260, OB110310, and OB110462). The one iteration 3σ clipped uncertainty-weighted average difference in the proper motion between the cross-matched stars is calculated and then applied to the relative HST astrometry to place it into the absolute Gaia proper-motion frame. The values to convert between the HST and Gaia frames for each target's field are listed in Table 17.

The vector point diagram of proper-motion differences between cross-matched sources in the Gaia and HST F814W catalogs, after applying the proper-motion offset to place the HST catalog into the Gaia reference frame, is shown in Figure 24. In general, the proper motions of bright stars in Gaia are inconsistent with those derived using HST. For fainter stars, the uncertainties are much larger, so there is more consistency between Gaia and HST; however, there is substantial scatter between the measurements of the two catalogs. The discrepancies between the HST and Gaia proper motions could
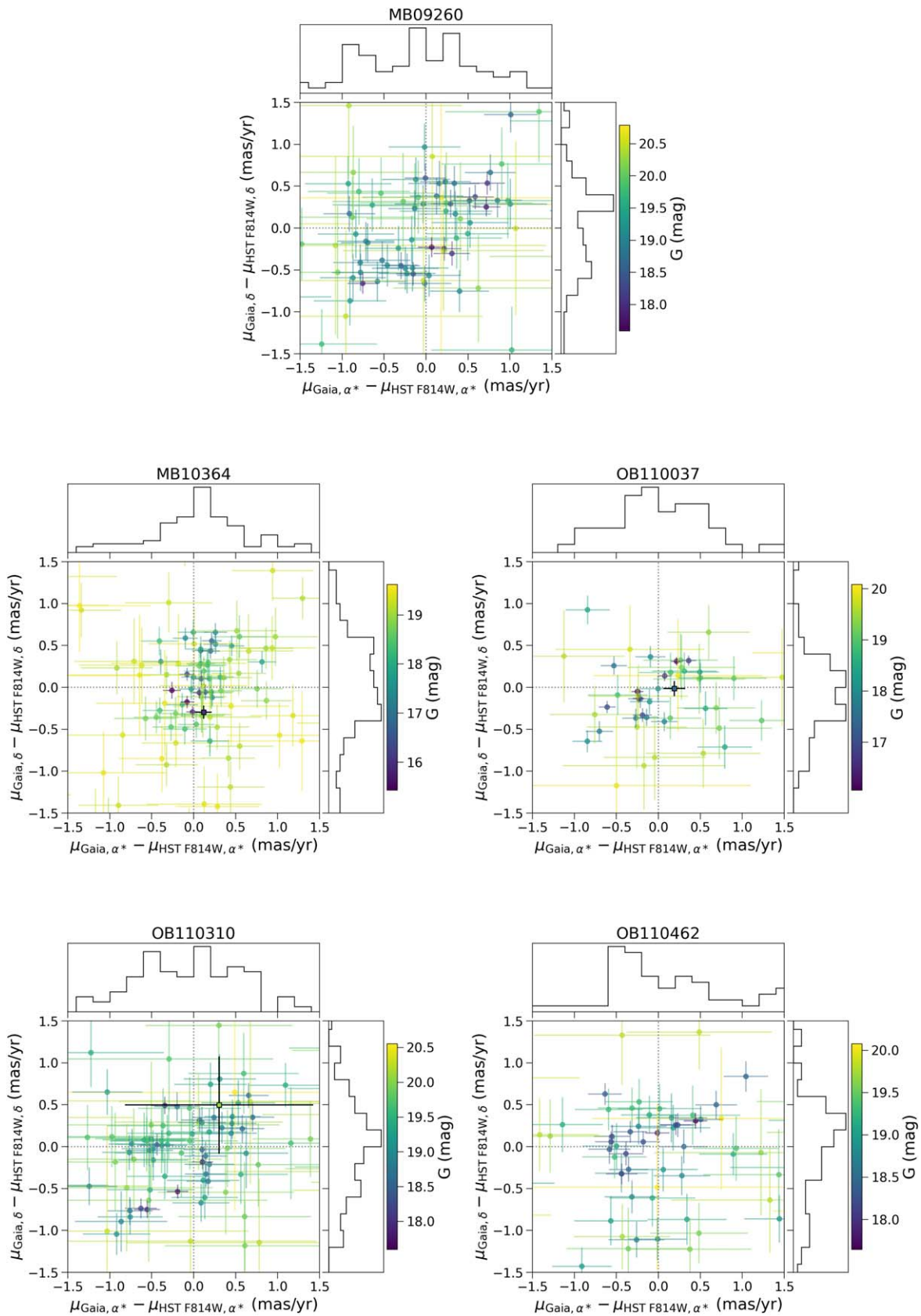
Figure 24. Vector point diagram of proper-motion differences between cross-matched sources in the Gaia and HST F814W catalogs within 60″ of the targets, after applying the constant proper-motion offset derived in Appendix C to place the HST catalog into the Gaia reference frame. The color of the point denotes the cross-matched source's magnitude in Gaia G band. MB10364, OB110037, and OB110310 are sources in Gaia; they are shown as the black-outlined squares and error bars.

Table 17
HST to Gaia Proper-motion Reference Frame Offset

Target	$\langle \Delta\mu_{\alpha*} \rangle$ (mas yr^{-1})	$\langle \Delta\mu_{\delta} \rangle$ (mas yr^{-1})
MB09260	-2.56 ± 0.13	-4.25 ± 0.10
MB10364	-2.70 ± 0.10	-4.56 ± 0.10
OB110037	-2.31 ± 0.23	-4.48 ± 0.20
OB110310	-2.20 ± 0.12	-4.73 ± 0.08
OB110462	-2.34 ± 0.15	-4.72 ± 0.11

Note. $\Delta\mu_{\alpha*} = \mu_{\text{Gaia},\alpha*} - \mu_{\text{HST F814W},\alpha*}$ and $\Delta\mu_{\delta} = \mu_{\text{Gaia},\delta} - \mu_{\text{HST F814W},\delta}$.

indicate that the uncertainties are underestimated in one or both catalogs, or that there are higher-order distortions between the two reference frames that cannot be captured by a constant offset. However, the most likely explanation is that the Gaia proper motions are not accurate, as it is clear that the Gaia EDR3 astrometry is unreliable in crowded regions like the Galactic Bulge (see Appendix E and Rybizki et al. 2022).

Appendix D
Astrometric Lensing in Gaia

As discussed in Section 4.2.6, there are several differences with the proper-motion modeling of microlensing targets in this paper as compared to Gaia. First, we simultaneously model the proper motions of the lens and source with parallax within a microlensing model. In contrast, Gaia models the proper motion of a single star with parallax. As the source and lens are not resolved by Gaia during the observations, if the lens is luminous, the proper motions of the source and lens are being treated as a single object. Depending on the relative source−lens motion and colors, this can produce different inferred proper motions. Second, the temporal baselines of the data used to calculate the proper motions differ. The HST time baseline spans 2010–2013 for MB10364 and 2011–2017 for OB110037 and OB110310, in contrast to 2014–2017 in Gaia. As the astrometric lensing signal is time dependent, temporal baseline differences can also lead to different inferred proper motions.

With regard to the second point, we estimate the amount by which astrometric microlensing could affect the proper-motion measurement. The lens−source separation $\boldsymbol{u}(t)$ (Equation (20)) sets the time evolution of the astrometric shift $\delta_c(t)$ (Equation (27)). Three terms contribute to $\boldsymbol{u}(t)$: the impact parameter $\boldsymbol{u}_0$, the source−lens proper motion $(t - t_0)\hat{\boldsymbol{\mu}}_{\text{rel}}/t_E$, and the microlensing parallax $\pi_E\boldsymbol{P}(t)$. As Earth's orbit around the Sun is nearly circular, $|\boldsymbol{P}(t)| \approx 1$ to within 3%. For typical microlensing events like MB10364, OB110037, and OB110310, $|\boldsymbol{u}_0| < 1$ and $\pi_E < 1$. Thus, long after source−lens closest approach, i.e., $(t - t_0)/t_E \gg 1$, the contributions by the impact parameter and microlensing parallax terms to $\boldsymbol{u}(t)$ are subdominant to that of the source−lens relative proper motion, and the source−lens separation can be approximated by

$$u(t) \approx \frac{t - t_0}{t_E} \gg 1. \tag{D1}$$

The astrometric shift for large source−lens separations $u \gg 1$ can be approximated as

$$\delta_c(t) \approx \frac{\theta_E}{u(t)}. \tag{D2}$$

Putting these two equations together, we can approximate how much a proper-motion measurement based on observations

made at times t_2 and t_1 will change owing to astrometric microlensing as

$$\Delta_{\text{PM}} \approx \frac{\delta_c(t_2) - \delta_c(t_1)}{t_2 - t_1} \tag{D3}$$

$$\approx \frac{\theta_E}{t_2 - t_1}\left(\frac{t_E}{t_2 - t_0} - \frac{t_E}{t_1 - t_0}\right), \tag{D4}$$

where $(t_2 - t_0)/t_E$, $(t_1 - t_0)/t_E \gg 1$. For MB10364, OB110037, and OB110310, for t_1 and t_2 corresponding to the start and end of Gaia EDR3 observations, $\Delta_{\text{PM}} \approx 0.003$, 0.02, and 0.01 mas yr^{-1}, respectively. In other words, the effect of lensing on proper motions should be negligible in Gaia. Thus, if the lens is dark, the proper motions of the source as measured by the HST data and the proper motion of the target reported by Gaia should be the same within the uncertainties.

Appendix E
Gaia Diagnostics

We would ideally like to incorporate information from Gaia EDR3 into our target analysis (e.g., using the reported parallaxes and proper motions to inform the prior on the source parallax in the fit, or to compare to the posteriors as a cross-check to validate the results). However, it is known that there are many as-of-yet-unresolved systematics in the Gaia EDR3 astrometry, especially toward the Bulge, and extra care must be taken to verify that a proper motion or parallax for a particular Gaia source is reliable. Gaia EDR3 is much better than Gaia DR2 in terms of photometry, but the astrometry still has issues that need to be worked out (Fabricius et al. 2021). We investigate several different metrics for the Gaia solutions for our targets to determine the reliability of the reported parallax and proper motions. A brief summary of the meaning of relevant Gaia statistics is presented in Table 3; we refer the reader to the Gaia Early Data Release 3 documentation (van Leeuwen et al. 2021) for details.

E.1. Solution Type

Sources in Gaia have varying amounts of information available, described by the `astrometric_params_-solved` parameter. A value of 3 signifies a two-parameter solution (position), a value of 31 signifies a five-parameter solution (position, parallax, proper motion), and a value of 95 signifies a six-parameter solution (position, parallax, proper motion, astrometrically estimated effective wavenumber). Five-parameter solutions are generally the most accurate, followed by six-parameter and then two-parameter solutions. Six-parameter solutions are worse than five-parameter solutions because it means that an assumption had to be made about the source color. This usually indicates an issue with determining the properties of the source, which reduces the accuracy of the solution. This can happen in very crowded regions, like the Bulge. MB09260 has a two-parameter solution, MB10364 and OB110310 have six-parameter solutions, and only OB110037 has a five-parameter solution. Based on the high-resolution HST images (Figure 1), this is not surprising, as OB110037 is the brightest object in its vicinity, while the other targets are near, comparably bright stars.

E.2. Image Parameter Determination Parameters

The Gaia EDR3 solution assumes that each source is a single star. Gaia's IPD parameters can be used to determine whether this assumption is valid. Different types of binaries can be identified through large IPD values: `ipd_gof_harmonic_amplitude` (indicates partially resolved binaries, asymmetric images), `ipd_frac_multi_peak` (indicates resolved, close binaries), `ipd_frac_odd_win` (indicates another bright source, or observation window conflicts for wide pairs) (Lindegren et al. 2021b). Given that the targets all have light curves well described by point lenses (although see Section 7.4 regarding indications of binarity in OB110037), we do not expect any of these parameters to be unusual for our targets; unusual values likely indicate problems with the astrometric solution itself due to crowding or contamination.

The `ipd_gof_harmonic_amplitude` values for MB09260, MB10364, OB110037, and OB11030 (0.089, 0.064, 0.036, and 0.042, respectively) are somewhat large compared to the median values reported in Tables 4–6 of Lindegren et al. (2021b). However, this is to be expected toward the Bulge. Compared to other sources within 1 deg^2 (Table 18) of these targets, the values are not unusual.[42]

MB10364 has `ipd_frac_multi_peak` = 15. The high-resolution HST images do not indicate that MB10364 is a resolved binary. The last HST image is from 2014, and Gaia EDR3 observations span 2014–2017. A possibility is that the lens and source separation after 2014 was large enough to resolve with Gaia EDR3. However, this is ruled out by considering the lens−source separation criteria (Table 13) and that Gaia's resolution is worse than HST's. The most likely explanation is confusion in Gaia due to stars near MB10364 since the crowding within 1″ of MB10364 is high. The other targets have `ipd_frac_multi_peak` = 0.

MB09260 has `ipd_frac_odd_win` = 18, and OB110310 has `ipd_frac_odd_win` = 55. Similar to the case of MB10364 in the previous paragraph, this is likely due to bright stars within 1″ of these targets that led to confusion in Gaia. The other targets have `ipd_frac_odd_win` = 0.

E.3. Astrometric Goodness-of-fit Statistics

Gaia also presents several relevant goodness-of-fit statistics from the astrometric fit: the RUWE (ideally 1), the extra noise required per observation to explain the residual in the astrometric fit of the source (`astrometric_excess_noise`; ideally 0), and the significance of this source noise (`astrometric_excess_noise_sig`; insignificant if <2).

MB09260 does not have an RUWE because it is not calculated for two-parameter solutions. OB110037 and OB110310 both have RUWE ∼1 (0.971 and 0.981, respectively). MB10364 has a large RUWE (1.388), although not unusual compared to the sources nearby (Table 18).[43]

MB09260 and MB10364 both have significant astrometric excess noise (1.241 mas and 0.406 mas, respectively). OB110037 does not have astrometric excess noise, and the noise for OB110310 is not significant.

---

[42] Note that the values reported in Table 18 are the logarithms of `ipd_gof_harmonic_amplitude`. We choose to report the logarithms because they are approximately normally distributed.

[43] Note that the values reported in Table 18 are the logarithms of RUWE. We choose to report the logarithms because they are approximately normally distributed.

Table 18
Distribution of Gaia Parameters toward Fields of Interest

Parameter	MB09260	MB10364	OB110037	OB110310
N_{stars}	611	1157	1056	884
$f_{D>2}$	0.44	0.51	0.59	0.55
$f_{\epsilon=0}$	0.81	0.77	0.85	0.86
$f_{\mathrm{multi}=0}$	0.79	0.41	0.53	0.70
med(multi $_{>0}$)	4.50	14.00	9.00	5.00
multi $_{>0[95\%]}$)	37.55	54.00	42.30	43.00
$f_{\mathrm{odd}=0}$	0.76	0.61	0.64	0.64
med(odd $_{>0}$)	25.50	30.00	26.00	27.50
odd $_{>0[95\%]}$)	83.55	78.20	80.00	78.70
$\langle\log_{10}(\mathrm{amp})\rangle$	−1.24	−0.89	−1.03	−1.13
$\sigma_{\log_{10}(\mathrm{amp})}$	0.45	0.39	0.58	0.44
$\langle\log_{10}(\mathrm{ruwe})\rangle$	0.04	0.12	0.08	0.06
$\sigma_{\log_{10}(\mathrm{ruwe})}$	0.10	0.16	0.11	0.11
$\langle\log_{10}(C)\rangle$	0.23	0.22	0.25	0.26
$\sigma_{\log_{10}(C)}$	0.12	0.16	0.15	0.15

Note. N_{stars}: number of Gaia sources within 1 deg^2 of the target. $f_{D>2}$: fraction of sources with `astrometric_excess_noise_significance` > 2. $f_{\epsilon=0}$: fraction of sources with `astrometric_excess_noise` > 2. $f_{\mathrm{multi}=0}$: fraction of stars with `ipd_frac_multi_peak`= 0. med(multi $_{>0}$): median of nonzero `ipd_frac_multi_peak` values. multi $_{>0[95\%]}$): 95th quantile of nonzero `ipd_frac_multi_peak` values. $f_{\mathrm{odd}=0}$: fraction of stars with `ipd_frac_odd_win` = 0. med(odd $_{>0}$): median of nonzero `ipd_frac_odd_win` values. odd $_{>0[95\%]}$): 95th quantile of nonzero `ipd_frac_odd_win` values. $\langle\log_{10}(\mathrm{amp})\rangle$: mean of $\log_{10}$(`ipd_gof_harmonic_amplitude`). $\sigma_{\log_{10}(\mathrm{amp})}$: standard deviation of $\log_{10}$(`ipd_gof_harmonic_amplitude`). $\langle\log_{10}(\mathrm{ruwe})\rangle$: mean of $\log_{10}$(ruwe). $\sigma_{\log_{10}(\mathrm{ruwe})}$: standard deviation of $\log_{10}$(ruwe). $\langle\log_{10}(C)\rangle$: mean of $\log_{10}$(`phot_bp_rp_excess_factor`). $\sigma_{\log_{10}(C)}$: standard deviation of $\log_{10}$(`phot_bp_rp_excess_factor`).

Table 18 lists the distributions of D = astrometric excess noise significance for the stars in Gaia within 1 deg^2 of our targets. Gaia documentation notes that $D = 0$ for roughly half the sources and $D > 2$ for a few percent of sources with well-behaved astrometric solutions (van Leeuwen et al. 2021). Near MB09260, 84% of sources have $D > 0$ and 44% have $D > 2$. Near MB10364, 79% of sources have $D > 0$ and 51% have $D > 2$. Near OB110037, 86% of sources have $D > 0$ and 59% have $D > 2$. Near OB110310, 87% of sources have $D > 0$ and 54% have $D > 2$. This indicates that the astrometric solution is not well behaved. This is not surprising, as there still exist many systematics in the astrometry, especially toward the Bulge. Figure 25 shows astrometric excess noise significance plotted against astrometric excess noise for systems where astrometric excess noise is nonzero.

E.4. Color Excess

Fabricius et al. (2021) use C = `phot_bp_rp_excess_factor` as a proxy for contamination due to crowding. Stars with large excess ($C > 5$) tend to have underestimated proper-motion uncertainties by a factor of ∼1.7. All of our targets have $C < 5$; less than 1% of stars within 1 deg^2 of the targets have $C > 5$. This metric does not seem to capture crowding toward the Bulge.

E.5. Summary

Compared to the high-resolution images from HST, the various metrics reported by Gaia make sense.
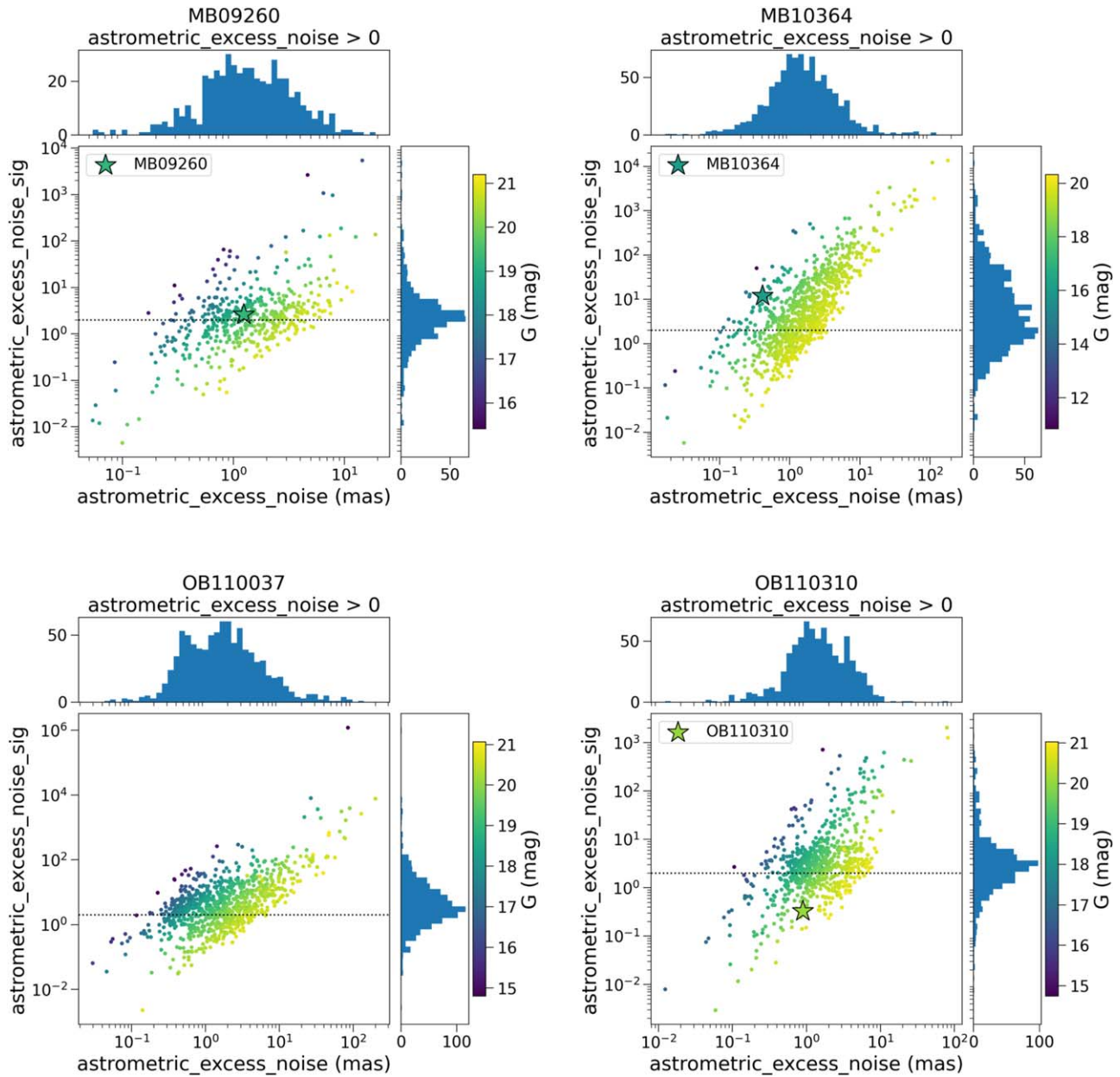
Figure 25. Astrometric excess noise vs. astrometric excess noise significance as a function of *G* magnitude, for sources with nonzero astrometric excess noise in the 1 deg² fields surrounding the microlensing targets found in Gaia. The targets are marked as stars; OB110037 is not marked, as it has astrometric excess noise 0. The dotted horizontal line denotes `astrometric_excess_noise_sig` =2; values < 2 are not significant.

1. OB110037 is the brightest source in its vicinity and hence has a good astrometric solution. Its astrometric solutions (parallax and proper motion) are likely to be reliable. The HST source proper motion agrees with the Gaia proper-motion measurement.
2. MB10364 is bright but is in a crowded field. OB110310 is somewhat isolated but is faint. Their astrometric solutions are likely to be unreliable.
3. MB09260 does not have enough visibility periods to generate an astrometric solution (which requires at least nine visibility periods, while MB09260 only has eight).

In conclusion, although Gaia is a dedicated astrometric mission, it is not optimized for the crowded and extincted Bulge, and the astrometric parameters are likely to be untrustworthy there (Fabricius et al. 2021; Rybizki et al.

2022). Although Gaia EDR3 is also an improvement over DR2, those improvements are in the photometry and not the astrometry. Placing too much weight on the Bulge astrometry in analyses (especially the uncertainties) should be done with caution. To make use of Gaia data for these targets, we will need to wait for future data releases with improved astrometry in crowded fields, as well as per-epoch astrometry.

Appendix F
Gaussian Process

The photometric microlensing survey data contain uncharacterized systematics in the light curves, which may be due to unaccounted-for correlated noise from astrophysical processes or data acquisition and reduction. Correlated noise can bias the results of parameter estimation. Golovich et al. (2022) fit a set

of publicly released OGLE-III and OGLE-IV microlensing light curves using Gaussian processes (GPs) to account for correlated noise; we follow that approach here. We use the `celerite` package (Foreman-Mackey et al. 2017) to implement GPs in our microlensing model.

For a thorough reference about GPs and their application to machine learning and inference, the reader may consult sources such as Rasmussen & Williams (2006). In short, a GP is composed of two parts: the noise (the stochastic component) and the mean function (the deterministic component). The properties of the stochastic component are governed by the covariance matrix, also known as the kernel, of the GP. The notation

$$y \sim \mathcal{GP}(\mu_{\boldsymbol{\theta}}(t), K_{\boldsymbol{\alpha}}(t, t')) \tag{F1}$$

indicates a GP with mean function μ with parameters $\boldsymbol{\theta}$ and kernel K with parameters $\boldsymbol{\alpha}$.

When trying to infer some set of parameters $\boldsymbol{\theta}$ from data

$$\boldsymbol{y} = (y_1(t_1)... \quad y_N(t_N))^T, \tag{F2}$$

the Gaussian log-likelihood is

$$\log \mathcal{L}(\boldsymbol{y}|\boldsymbol{\theta}, \boldsymbol{\alpha}) = -\frac{1}{2}\boldsymbol{r}_{\boldsymbol{\theta}}^T K_{\boldsymbol{\alpha}}^{-1}\boldsymbol{r}_{\boldsymbol{\theta}} - \frac{1}{2}\log|K_{\boldsymbol{\alpha}}| - \frac{N}{2}\log(2\pi), \tag{F3}$$

where N is the number of data points and $\boldsymbol{r}_{\boldsymbol{\theta}}$ is the residual vector

$$\boldsymbol{r}_{\boldsymbol{\theta}} = (y_1 - \mu_{\boldsymbol{\theta}}(t_1)... \quad y_N - \mu_{\boldsymbol{\theta}}(t_N))^T. \tag{F4}$$

In the residual vector, $\mu_{\boldsymbol{\theta}}$ is the mean model, which in our case is the microlensing model. The kernel or covariance matrix $K_{\boldsymbol{\alpha}}$ describes the correlated errors. If the errors are not correlated, $K_{\boldsymbol{\alpha}}$ is diagonal and the likelihood reduces to the familiar form

$$\log \mathcal{L}(\boldsymbol{y}|\boldsymbol{\theta}) = -\frac{1}{2}\sum_i \left(\log[2\pi\sigma_i^2] + \frac{(y_i - \mu_{\boldsymbol{\theta}}(t_i))^2}{\sigma_i^2} \right)$$
$$= -\frac{1}{2}\sum_i \log[2\pi\sigma_i^2] - \frac{1}{2}\chi^2, \tag{F5}$$

where σ_i is the uncertainty on data point y_i and χ^2 is the "goodness of fit."

Following Golovich et al. (2022), a damped driven simple harmonic oscillator (DDSHO) kernel κ_{DDSHO} added to a Matérn-3/2 kernel $\kappa_{M3/2}$ is used to model the correlated noise in the photometric microlensing survey light curves. Both these kernels are stationary, as they are a function of the differences of the times only:

$$\tau_{ij} = |t_i - t_j|. \tag{F6}$$

The kernel is given by

$$K_{\boldsymbol{\alpha}}(\tau_{ij}) = \kappa_{\text{DDSHO}}(\tau_{ij}) + \kappa_{M3/2}(\tau_{ij}) + \delta_{ij}\sigma_i^2. \tag{F7}$$

Qualitatively, the DDSHO kernel models smooth variations, while the Matérn-3/2 captures more irregular variations.

The DDSHO kernel is given by

$$\kappa_{\text{DDSHO}}(\tau_{ij}) = S_0\omega_0 e^{-\omega_0\tau_{ij}/\sqrt{2}} \cos\left(\frac{\omega_0\tau_{ij}}{\sqrt{2}} - \frac{\pi}{4} \right), \tag{F8}$$

where S_0 controls the amplitude of the deviation from the mean model and ω_0 controls the variation frequency. This kernel has

been used in asteroseismic modeling (Li et al. (2019) and references therein).

The Matérn-3/2 kernel is given by

$$\kappa_{M3/2}(\tau_{ij}) = \sigma^2 e^{-\sqrt{3}\,\tau_{ij}/\rho}\left(1 + \frac{\sqrt{3}\,\tau_{ij}}{\rho} \right), \tag{F9}$$

where σ determines the amount of deviation allowed from the mean model and ρ is the characteristic coherence scale. The Matérn-3/2 kernel has been used to model correlated noise in the light curves of transiting and eclipsing exoplanets (Gibson et al. 2013; Evans et al. 2015) and, in particular, is appropriate for modeling nonsmooth behaviors (Gilbertson et al. 2020). For numerical reasons (see Section 4 of Foreman-Mackey et al. 2017), the Matérn-3/2 kernel is approximated as

$$\kappa_{M3/2}(\tau_{ij}) = \sigma^2 \left[\left(1 + \frac{1}{\epsilon} \right)e^{-\sqrt{3}(1-\epsilon)\tau_{ij}/\rho}\left(1 - \frac{1}{\epsilon} \right)e^{-\sqrt{3}(1+\epsilon)\tau_{ij}/} \right] \tag{F10}$$

In the limit $\epsilon \to 0$, this is exactly the Matérn-3/2 kernel. We implement the approximation with $\epsilon = 0.01$.

The ground-based OGLE and MOA photometry are fit using the Gaussian likelihood with a full covariance matrix (Equation (F3)). The HST photometry and astrometry are fit using the Gaussian likelihood assuming a diagonal covariance matrix (Equation (F5)).

Note that for MB10364, instead of fitting the MOA light curve using a GP, we instead fit an additive error on the ground-based photometry. During nested sampling, the GP showed some numerical instability.

Appendix G
Priors

The distributions for the priors π are described in this appendix. $\mathcal{N}(\mu, \sigma)$ denotes a normal distribution with mean μ and standard deviation σ. $\mathcal{N}_T(\mu, \sigma, l_\sigma, u_\sigma)$ denotes a normal distribution with a low-end truncation at $\mu + \sigma l_\sigma$ and a high-end truncation at $\mu + \sigma u_\sigma$. $\mathcal{U}(a, b)$ denotes a uniform distribution from a to b. $\Gamma^{-1}(\alpha, \beta)$ is the inverse gamma distribution

$$\Gamma^{-1}(x; \alpha, \beta) = \frac{\beta^\alpha}{\Gamma(\alpha)}x^{-\alpha-1}\exp[-\beta/x]. \tag{G1}$$

The prior distributions for each target are summarized in Table 19.

G.1. Photometry Priors

The five microlensing parameters in a PSPL with parallax fit are t_0, u_0, t_E, $\pi_{E,E}$, and $\pi_{E,N}$.

The prior on t_0 is a normal distribution centered on the time of peak magnification in the geocentric frame, with a spread of 75 days,

$$\pi(t_0) \sim \mathcal{N}(t_{\text{peak},\oplus}, 75 \text{ days}). \tag{G2}$$

Note that the time at peak magnification in the heliocentric frame t_0 is not necessarily the same as in the geocentric frame $t_{\text{peak},\oplus}$, hence the large amount of spread in the prior.

Table 19
Priors

Parameter	MB09260	MB10364	OB110037	OB110310	OB110462 DW	OB110462 EW
t_0 (MJD)	$\mathcal{N}(55{,}110, 75)$	$\mathcal{N}(55{,}460, 75)$	$\mathcal{N}(55{,}805, 75)$	$\mathcal{N}(55{,}810, 75)$	$\mathcal{N}(55{,}770, 75)$	$\mathcal{N}(55{,}770, 75)$
u_0	$\mathcal{N}(0, 0.5)$	″	″	″	″	″
t_E (days)	$\mathcal{N}_T(200, 100, -1.8, 3)$	″	″	″	″	″
$\pi_{E,E}$	$\mathcal{N}(-0.02, 0.12)$	″	″	″	″	″
$\pi_{E,N}$	$\mathcal{N}(-0.03, 0.13)$	″	″	″	″	″
$m_{\text{base},O/M}$ (mag)	$\mathcal{N}(17.43, 0.2)$	$\mathcal{N}(15.02, 0.2)$	$\mathcal{N}(16.15, 0.1)$	$\mathcal{N}(18.41, 0.1)$	$\mathcal{N}(16.41, 0.1)$	$\mathcal{N}(16.41, 0.1)$
$b_{\text{SFF},O/M}$	$\mathcal{U}(0, 1.1)$	″	″	″	″	″
$m_{\text{base},H8}$ (mag)	$\mathcal{N}(17.83, 0.05)$	$\mathcal{N}(15.32, 0.05)$	$\mathcal{N}(16.33, 0.05)$	$\mathcal{N}(18.61, 0.05)$	$\mathcal{N}(19.85, 0.05)$	$\mathcal{N}(19.85, 0.05)$
$b_{\text{SFF},H8}$	$\mathcal{U}(0, 1.05)$	″	″	″	″	″
$m_{\text{base},H6}$ (mag)	$\mathcal{N}(20.74, 0.05)$	$\mathcal{N}(16.50, 0.05)$	$\mathcal{N}(18.33, 0.05)$	$\mathcal{N}(21.34, 0.05)$	$\mathcal{N}(22.03, 0.05)$	$\mathcal{N}(22.03, 0.05)$
$b_{\text{SFF},H6}$	$\mathcal{U}(0, 1.05)$	″	″	″	″	″
$\log \sigma_{0,O/M}$ (mag)	$\mathcal{N}(0, 5)$	″	″	″	⋯	⋯
$\rho_{O/M}$ (days)	$\Gamma^{-1}(0.448, 0.063)$	$\Gamma^{-1}(0.448, 0.113)$	$\Gamma^{-1}(0.473, 0.162)$	$\Gamma^{-1}(0.527, 0.450)$	⋯	⋯
$\log \omega_{0,O/M}^4 S_{0,O/M}$ (mag^2 days $^{-3}$)	$\mathcal{N}(3.53\text{e}{-}04, 5)$	$\mathcal{N}(8.41\text{e}{-}06, 5)$	$\mathcal{N}(3.60\text{e}{-}05, 5)$	$\mathcal{N}(1.02\text{e}{-}03, 5)$	⋯	⋯
$\log \omega_{0,O/M}$ (days^{-1})	$\mathcal{N}(0, 5)$	″	″	″	⋯	⋯
$\log_{10}(\theta_E)$ (mas)	$\mathcal{N}(-0.2, 0.3)$	″	″	″	$\mathcal{N}(0.5, 0)$	$\mathcal{N}(0.5, 0)$
π_S (mas)	$\mathcal{N}_T(0.1126, 0.0213, -2.94, 90)$	″	″	″	″	″
$x_{S0,E}$ (arcseconds)	$\mathcal{U}(0.213, 0.250)$	$\mathcal{U}(0.086, 0.158)$	$\mathcal{U}(-0.034, 0.091)$	$\mathcal{U}(-0.108, -0.103)$	$\mathcal{U}(0.227, 0.233)$	$\mathcal{U}(0.227, 0.233)$
$x_{S0,N}$ (arcseconds)	$\mathcal{U}(-0.697, -0.683)$	$\mathcal{U}(-0.096, -0.068)$	$\mathcal{U}(-0.122, -0.104)$	$\mathcal{U}(-0.228, -0.154)$	$\mathcal{U}(-0.235, -0.183)$	$\mathcal{U}(-0.235, -0.183)$
$\mu_{S,E}$ (mas yr^{-1})	$\mathcal{U}(-5.96, 1.12)$	$\mathcal{U}(-7.93, -1.78)$	$\mathcal{U}(0.87, 8.05)$	$\mathcal{U}(-1.30, 0.95)$	$\mathcal{U}(-4.82, 4.99)$	$\mathcal{U}(-4.82, 4.99)$
$\mu_{S,N}$ (mas yr^{-1})	$\mathcal{U}(-2.37, 4.17)$	$\mathcal{U}(-7.28, 3.41)$	$\mathcal{U}(-1.67, 2.94)$	$\mathcal{U}(-4.55, -0.49)$	$\mathcal{U}(-3.49, 5.91)$	$\mathcal{U}(-3.49, 5.91)$

Note. For definitions of the different variables, see Appendix G. There are two fits for OB110462 depending on the likelihood used, "equal weighting″ (OB110462 EW) or "default weighting″ (OB110462 DW). See Section 5.3 for details.

The prior on u_0 is a Gaussian with mean 0 and standard deviation 0.5,

$$\pi(u_0) \sim \mathcal{N}(0, 0.5), \tag{G3}$$

which takes into account that events with smaller $|u_0|$ are more likely to be detected and that events with $|u_0| > 1.5$ are not robustly detectable with current ground-based surveys.[44]

The prior on t_E is a Gaussian centered at 200 days with a large spread of $\sigma = 100$ days. The distribution is truncated at -1.8σ and 3σ (20 and 500 days, respectively):

$$\pi(t_E) \sim \mathcal{N}_T(200, 50, -1.8, 10) \text{ days}. \tag{G4}$$

The priors on the microlensing parallax are estimated from the population of bulge microlensing events from the PopSyCLE simulation:

$$\pi(\pi_{E,E}) \sim \mathcal{N}(-0.02, 0.12) \tag{G5}$$

$$\pi(\pi_{E,N}) \sim \mathcal{N}(-0.03, 0.13). \tag{G6}$$

For each data set filter, b_{SFF} and m_{base} are also fit. For the ground-based photometry, we use a prior

$$b_{SFF,ground} \sim \mathcal{U}(0, 1.1), \tag{G7}$$

where the negative blend flux implied by $b_{SFF} > 1$ allows for some extra noise such as imperfect background subtraction. Similarly for the HST astrometry, we use a uniform prior on b_{SFF},

$$b_{SFF,HST} \sim \mathcal{U}(0, 1.05). \tag{G8}$$

m_{base} is a normal distribution

$$m_{base} \sim \mathcal{N}(\overline{m}_{base}, \sigma_{\overline{m}_{base}}), \tag{G9}$$

where $\overline{m}_{base}$ is the average magnitude during the unmagnified seasons, weighted by the measurement uncertainties, and $\sigma_{\overline{m}_{base}}$ is 0.1 for OGLE, 0.2 for MOA, and 0.05 for HST.

G.2. Gaussian Process Hyperparameter Priors

The ground-based photometry includes correlated noise we fit. We follow a very similar parameterization to Golovich et al. (2022) for the GP priors. The main difference is that fit in magnitude space instead of flux space, and so our priors are also in magnitudes instead of fluxes.

For σ, we use the prior

$$\log(\sigma/\text{mag}) \sim \mathcal{N}(0, 5), \tag{G10}$$

which allows a wide range of light-curve amplitude variability.

For ρ, we use the prior

$$\rho \sim \Gamma^{-1}(a, b), \tag{G11}$$

where a and b are the constants that satisfy the relation

$$0.01 = \int_0^{\text{med}(\Delta t)} \Gamma^{-1}(x; a, b) \, dx \tag{G12}$$

$$0.01 = 1 - \int_0^{\Delta T} \Gamma^{-1}(x; a, b) \, dx, \tag{G13}$$

where $\text{med}(\Delta t)$ is the median duration between observations and ΔT is the duration of the full data set. This helps suppress

values at extremely short or long timescales that might lead to ill-behaved models.[45]

For S_0 and ω_0 we use the priors

$$\log S_0 \omega_0^4 \sim \mathcal{N}(\text{med}(\sigma_m^2), 5) \tag{G14}$$

$$\log \omega_0 \sim \mathcal{N}(0, 5). \tag{G15}$$

G.3. Astrometry Priors

The prior on the Einstein radius θ_E is a lognormal distribution estimated from PopSyCLE for events with $t_E > 50$ or $t_E > 120$ days as

$$\pi(\log_{10}(\theta_E/\text{mas})) \sim \mathcal{N}(-0.2, 0.3) \tag{G16}$$

$$\pi(\log_{10}(\theta_E/\text{mas})) \tilde{} \mathcal{N}(0, 0.5), \tag{G17}$$

respectively. We use the prior from $t_E > 120$ days for OB110462 and $t_E > 50$ days for the other four targets.

The prior on the source parallax π_S is estimated from the population of bulge microlensing events from the PopSyCLE simulation

$$\pi(\pi_S) \sim \mathcal{N}_T(0.1126, 0.0213, -2.9390, 90.0) \text{ mas}, \tag{G18}$$

which corresponds to source distances ranging from 0.5 to 20 kpc.

The priors on the source proper motion $\mu_{S,E}$ and $\mu_{S,N}$ are uniform distributions

$$\pi(\mu_{S,E}) \sim \mathcal{U}(\overline{\mu}_{S,E} - f\sigma_{\overline{\mu}_{S,E}}, \overline{\mu}_{S,E} + f\sigma_{\overline{\mu}_{S,E}}) \tag{G19}$$

$$\pi(\mu_{S,N}) \sim \mathcal{U}(\overline{\mu}_{S,N} - f\sigma_{\overline{\mu}_{S,N}}, \overline{\mu}_{S,N} + f\sigma_{\overline{\mu}_{S,N}}), \tag{G20}$$

where $\overline{\mu}_{S,E}, \overline{\mu}_{S,N}$ are the proper motions inferred from assuming straight-line motion (no parallax) from the F814W data, $\sigma_{\overline{\mu}_{S,E}}$, $\sigma_{\overline{\mu}_{S,N}}$ are the uncertainties to that fit, and f is an inflation factor. To allow a wide range of proper motions, we use $f = 100$.

The prior on the source position at t_0, $x_{0_S,E}$ and $x_{0_S,N}$, is

$$\pi(x_{0_S,E}) \sim \mathcal{U}(\min(x_E) - f\sigma_{x_E}, \max(x_E) + f\sigma_{x_E}) \tag{G21}$$

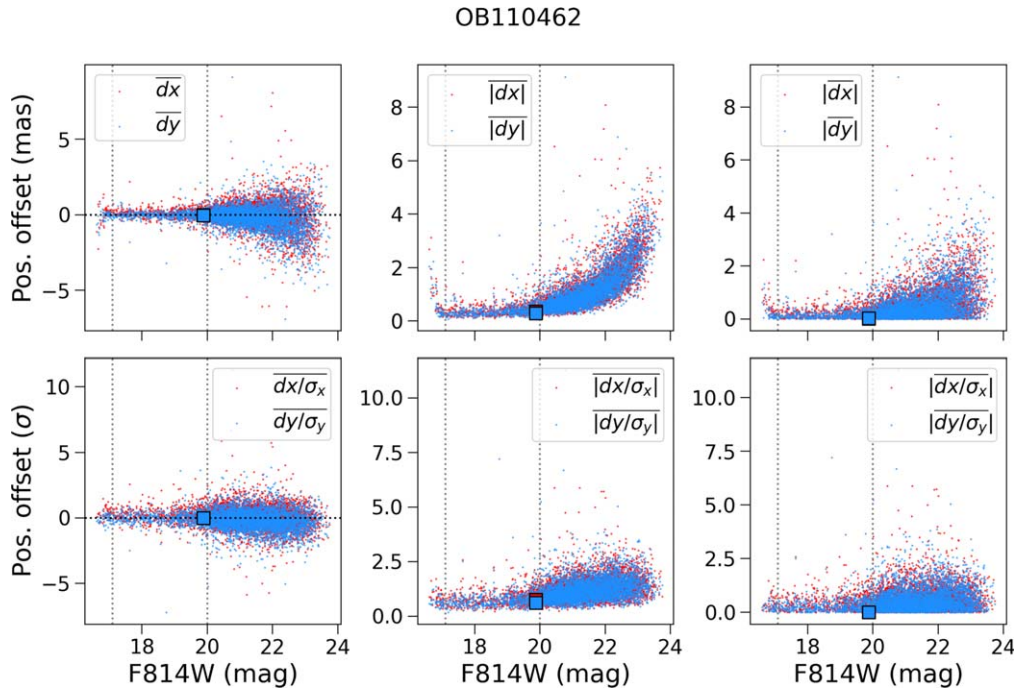$$\pi(x_{0_S,N}) \sim \mathcal{U}(\min(x_N) - f\sigma_{x_N}, \max(x_N) + f\sigma_{x_N}), \tag{G22}$$

where x_E, x_N are the positions in the F814W data of the target, σ_{x_E}, σ_{x_N} is the standard deviation, and f is an inflation factor. We use $f = 5$.

Appendix H
Astrometric Color Analysis

For some stars, the astrometric measurements taken in the F814W and F606W filter are discrepant at the level of the reported uncertainties. We explore this discrepancy specifically for OB110462, but this issue is also seen in OB110037 and reference stars for all targets.

First, we must quantify the discrepancy. We consider several ways to measure the total offset between the astrometry of the two filters across all epochs. $\overline{dx}$ is the average of the offsets in R.A. across all epochs for a particular star and can be thought of as measuring the amount of translation between F814W and F606W. $\overline{|dx|}$ is the average of the magnitude of the offsets in R. A. across all epochs for a particular star and can be thought of as measuring the absolute amount of translation between F814W and F606W. $|\overline{dx}|$ is the absolute value of the average of the magnitude of the offsets in R.A. across all epochs for a

---

[44] $|u_0| = 1.5$ corresponds to a brightening of no more than around 0.1 mag. When selecting microlensing events, those with a brightening less than 0.1 mag are generally excluded in survey samples to prevent contamination from low-amplitude variables (e.g., Mróz et al. 2019).

[45] See betanalpha.github.io/assets/case_studies/Gaussian_processes.

Figure 26. Difference in astrometry between observations taken in F814W vs. F606W for stars in the OB110462 images, aggregated across all epochs. Definitions of $\overline{dx}$, $|\overline{dx}|$, and $\overline{|dx|}$ are given in the text of Appendix H. The squares mark OB110462. The dashed lines indicate the magnitude range of the reference stars in the OB110462 images.

particular star and can be thought of as measuring the total amount of deviation between F814W and F606W. Note that $\overline{|dx|}$ is distinct from $|\overline{dx}|$. The definitions for $\overline{dy}$, $\overline{|dy|}$, and $|\overline{dy}|$ are analogous, except they are the offsets in decl. We also consider these quantities in units of sigma, where the differences in each epoch dx_i and dy_i are normalized by the positional uncertainties $\sigma_{x,i}$ and $\sigma_{y,i}$.

In Figure 26, we show the distributions of these quantities as a function of magnitude for stars within $30''$ of OB110462. While not falling in the bulk of the distribution, OB110462 is not an extreme outlier. Considering how large the variation in positional differences is, especially for fainter stars, OB110462 seems well within the other positions. For this reason, we assume that the positional differences are a systematic we can correct empirically. We apply a constant positional offset to the F606W OB110462 observations to match the positions of the F814W observations as described in Section 4.2.5. However, further investigation to determine whether the source of the filter-dependent astrometry of OB110462 and other stars may

actually be astrophysical is worth pursuing, as are more observational programs to study filter dependence on astrometry.

Appendix I
Directly Confronting the Photometry and Astrometry Tension

To try to elucidate the tension between the photometry and astrometry, we fit the OGLE photometry alone and separately fit the HST astrometry alone. The results are shown in Figure 27. The HST astrometry alone does not have very much constraining power—the uncertainties on parameters such as t_0, t_E, and u_0 are so wide that the fit itself is not useful. However, the results are consistent with those of the EW fit. The OGLE photometry has much more constraining power but alone cannot constrain the lens mass. The results are consistent with those of the DW fit.
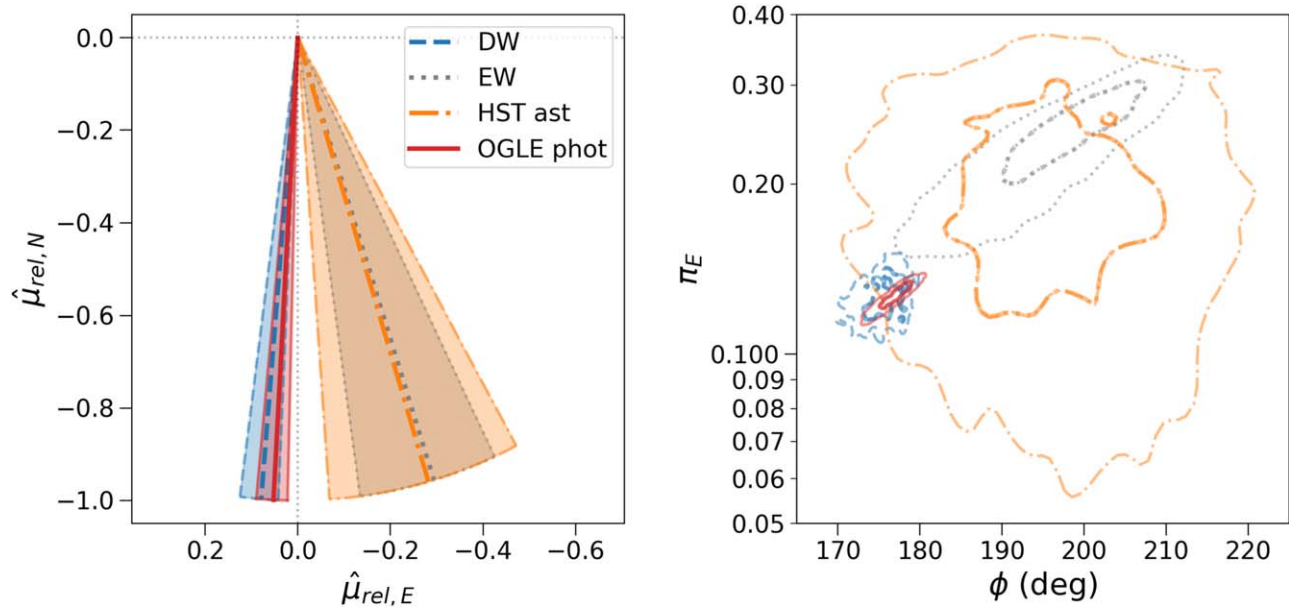
Figure 27. Left: comparison of the source−lens relative proper motion inferred from the photometry and astrometry using the default weighted likelihood (DW), the photometry and astrometry using the equal weighted likelihood (EW), from the HST astrometry alone (HST ast), and from the OGLE photometry alone (OGLE phot). The median is shown as the thick line; the shaded region denotes the 1σ uncertainties. Right: 1σ and 2σ contours of π_E and direction of the source−lens relative proper motion ϕ, for the four fits presented in the left panel. The EW fit is consistent with the fit to the HST astrometry, although the astrometry alone has very little constraining power. The DW and OGLE phot fits are consistent with each other, as expected.

ORCID iDs

Casey Y. Lam https://orcid.org/0000-0002-6406-1924
Jessica R. Lu https://orcid.org/0000-0001-9611-0009
Andrzej Udalski https://orcid.org/0000-0001-5207-5619
David P. Bennett https://orcid.org/0000-0001-8043-8413
Jan Skowron https://orcid.org/0000-0002-2335-1730
Przemek Mróz https://orcid.org/0000-0001-7016-1692
Radek Poleski https://orcid.org/0000-0002-9245-6368
Michał K. Szymański https://orcid.org/0000-0002-0548-8995
Szymon Kozłowski https://orcid.org/0000-0003-4084-880X
Paweł Pietrukowicz https://orcid.org/0000-0002-2339-5899
Igor Soszyński https://orcid.org/0000-0002-7777-0842
Krzysztof Ulaczyk https://orcid.org/0000-0001-6364-408X
Łukasz Wyrzykowski https://orcid.org/0000-0002-9658-6151
Nicholas J. Rattenbury https://orcid.org/0000-0001-5069-319X
Matthew W. Hosek, Jr. https://orcid.org/0000-0003-2874-1196
Clément Ranc https://orcid.org/0000-0003-2388-4534
Natasha S. Abrams https://orcid.org/0000-0002-0287-3783
Shrihan Agarwal https://orcid.org/0000-0002-2350-4610
Sam Rose https://orcid.org/0000-0003-4725-4481
Sean K. Terry https://orcid.org/0000-0002-5029-3257

References

Abbott, B. P., Abbott, R., Abbott, T. D., et al. 2017, ApJL, 851, L16
Abbott, B. P., Abbott, R., Abbott, T. D., et al. 2020a, ApJL, 892, L3
Abbott, R., Abbott, T. D., Abraham, S., et al. 2020b, ApJL, 896, L44
Abdurrahman, F. N., Stephens, H. F., & Lu, J. R. 2021, ApJ, 912, 146
Agol, E., & Kamionkowski, M. 2002, MNRAS, 334, 553
Anderson, J. 2016, Empirical Models for the WFC3/IR PSF, Instrument Science Report,, WFC3 2016-12
Anderson, J. 2021, Table-based CTE Corrections for flt-FormatWFC3/UVIS, Instrument Science Report,, WFC3 2021-13
Anderson, J., Baggett, S., & Kuhn, B. 2021, Updating the WFC3/UVIS CTE Model and Mitigation Strategies, Instrument Science Report,, 2021-9

Anderson, J., & King, I. R. 2006, PSFs, Photometry, and Astronomy for the ACS/WFC, Instrument Science Report, ACS 2006-01
Anderson, J., Sarajedini, A., Bedin, L. R., et al. 2008, AJ, 135, 2055
Astropy Collaboration, Price-Whelan, A. M., Sipőcz, B. M., et al. 2018, AJ, 156, 123
Astropy Collaboration, Robitaille, T. P., Tollerud, E. J., et al. 2013, A&A, 558, A33
Bailyn, C. D., Jain, R. K., Coppi, P., & Orosz, J. A. 1998, ApJ, 499, 367
Baraffe, I., Homeier, D., Allard, F., & Chabrier, G. 2015, A&A, 577, A42
Batista, V., Beaulieu, J. P., Bennett, D. P., et al. 2015, ApJ, 808, 170
Bellini, A., Anderson, J., & Bedin, L. R. 2011, PASP, 123, 622
Bellini, A., Libralato, M., Bedin, L. R., et al. 2018, ApJ, 853, 86
Bennett, D. P., Becker, A. C., Quinn, J. L., et al. 2002, ApJ, 579, 639
Bennett, D. P., Bhattacharya, A., Anderson, J., et al. 2015, ApJ, 808, 169
Bond, I. A., Abe, F., Dodd, R. J., et al. 2001, MNRAS, 327, 868
Bond, I. A., Bennett, D. P., Sumi, T., et al. 2017, MNRAS, 469, 2434
Buchner, J., Georgakakis, A., Nandra, K., et al. 2014, A&A, 564, A125
Castelli, F., & Kurucz, R. L. 1994, A&A, 281, 817
Choi, J., Dotter, A., Conroy, C., et al. 2016, ApJ, 823, 102
Damineli, A., Almeida, L. A., Blum, R. D., et al. 2016, MNRAS, 463, 2653
Eddington, A. S. 1919, Obs, 42, 119
El-Badry, K., Seeburger, R., Jayasinghe, T., et al. 2022, MNRAS, 512, 5620
Evans, I. N., Allen, C., Anderson, C. S., et al. 2019a, AAS Meeting, 233, 379.01
Evans, I. N., Allen, C., Anderson, C. S., et al. 2019b, AAS/High Energy Astrophysics Division, 17, 114.01
Evans, P. A., Page, K. L., Osborne, J. P., et al. 2020, ApJS, 247, 54
Evans, T. M., Aigrain, S., Gibson, N., et al. 2015, MNRAS, 451, 680
Fabricius, C., Luri, X., Arenou, F., et al. 2021, A&A, 649, A5
Farr, W. M., Sravan, N., Cantrell, A., et al. 2011, ApJ, 741, 103
Feroz, F., Hobson, M. P., & Bridges, M. 2009, MNRAS, 398, 1601
Foreman-Mackey, D., Agol, E., Ambikasaran, S., & Angus, R. 2017, AJ, 154, 220
Gaia Collaboration, Brown, A. G. A., Vallenari, A., et al. 2021, A&A, 649, A1
Gaia Collaboration, Prusti, T., de Bruijne, J. H. J., et al. 2016, A&A, 595, A1
Gennaro, M. E. A. 2018, WFC3 Data Handbook, Version 4.0 (Baltimore, MD: STScI)
Gibson, N. P., Aigrain, S., Barstow, J. K., et al. 2013, MNRAS, 428, 3680
Gilbertson, C., Ford, E. B., Jones, D. E., & Stenning, D. C. 2020, ApJ, 905, 155
Golovich, N., Dawson, W., Bartolić, F., et al. 2022, ApJS, 260, 2
Gould, A. 2004, ApJ, 606, 319

Green, G. 2018, JOSS, 3, 695

Groth, E. J. 1986, AJ, 91, 1244

Hearnshaw, J. B., Abe, F., Bond, I. A., et al. 2006, in The 9th Asian-Pacific Regional IAU Meeting, ed. W. Sutantyo et al. (Bandung: Institut Teknologi Bandung Press), 272

Hog, E., Novikov, I. D., & Polnarev, A. G. 1995, A&A, 294, 287

Hosek, M. W., Jr, Lu, J. R., Anderson, J., et al. 2015, ApJ, 813, 27

Hosek, M. W. J, Lu, J. R., Lam, C. Y., et al. 2020, AJ, 160, 143

Hunter, J. D. 2007, CSE, 9, 90

Husser, T.-O., Wende-von Berg, S., Dreizler, S., et al. 2013, A&A, 553, A6

Jonker, P. G., Kaur, K., Stone, N., & Torres, M. A. P. 2021, ApJ, 921, 131

Kains, N., Calamida, A., Sahu, K. C., et al. 2017, ApJ, 843, 145

Koester, D. 2010, MmSAI, 81, 921

Kreidberg, L., Bailyn, C. D., Farr, W. M., & Kalogera, V. 2012, ApJ, 757, 36

Kroupa, P. 2001, MNRAS, 322, 231

Kuhn, B., & Anderson, J. 2021, WFC3/UVIS: New FLC External CTE Monitoring 2009-2020, Instrument Science Report , WFC3 2021-6

Lam, C., & Lu, J. R. 2021, HST Proposal, 29, 16760

Lam, C. Y., Lu, J. R., Hosek, M. W. J, Dawson, W. A., & Golovich, N. R. 2020, ApJ, 889, 31

Lam, C. Y., Lu, J. R., Udalski, A., et al. 2022, ApJL, 933, L23

Li, S. S., Zang, W., Udalski, A., et al. 2019, MNRAS, 488, 3308

Lindegren, L., Bastian, U., Biermann, M., et al. 2021a, A&A, 649, A4

Lindegren, L., Klioner, S. A., Hernández, J., et al. 2021b, A&A, 649, A2

Lu, J. R., Sinukoff, E., Ofek, E. O., Udalski, A., & Kozlowski, S. 2016, ApJ, 830, 41

Luri, X., Brown, A. G. A., Sarro, L. M., et al. 2018, A&A, 616, A9

Maeda, Y., Kubota, A., Kobayashi, Y., et al. 2005, ApJL, 631, L65

Manchester, R. N., Hobbs, G. B., Teoh, A., & Hobbs, M. 2005, AJ, 129, 1993

Mao, S., Smith, M. C., Woźniak, P., et al. 2002, MNRAS, 329, 349

Marshall, D. J., Robin, A. C., Reylé, C., Schultheis, M., & Picaud, S. 2006, A&A, 453, 635

McGill, P., Everall, A., Boubert, D., & Smith, L. C. 2020, MNRAS, 498, L6

Miyamoto, M., & Yoshii, Y. 1995, AJ, 110, 1427

Mróz, P., Udalski, A., Skowron, J., et al. 2019, ApJS, 244, 29

Nucita, A. A., De Paolis, F., Ingrosso, G., et al. 2006, ApJ, 651, 1092

Özel, F., Psaltis, D., Narayan, R., & McClintock, J. E. 2010, ApJ, 725, 1918

Paczynski, B. 1986, ApJ, 304, 1

Park, B. G., DePoy, D. L., Gaudi, B. S., et al. 2004, ApJ, 609, 166

Penny, M. T., Gaudi, B. S., Kerins, E., et al. 2019, ApJS, 241, 3

Poindexter, S., Afonso, C., Bennett, D. P., et al. 2005, ApJ, 633, 914

Rasmussen, C. E., & Williams, C. K. I. 2006, Gaussian Processes for Machine Learning (Cambridge, MA: MIT Press)

Robin, A. C., Reylé, C., Derrière, S., & Picaud, S. 2003, A&A, 409, 523

Rowan, D. M., Stanek, K. Z., Jayasinghe, T., et al. 2021, MNRAS, 507, 104

Rybicki, K. A., Wyrzykowski, Ł., Klencki, J., et al. 2018, MNRAS, 476, 2013

Rybizki, J., Green, G. M., Rix, H.-W., et al. 2022, MNRAS, 510, 2597

Sabbi, E., Lennon, D. J., Anderson, J., et al. 2016, ApJS, 222, 11

Sahu, K. 2009, HST Proposal, 17, 11707

Sahu, K. 2012, HST Proposal, 20, 12986

Sahu, K. 2017, HST Proposal, 25, 15318

Sahu, K. C., Anderson, J., Casertano, S., et al. 2017, Sci, 356, 1046

Sarmiento, M. H., Arévalo, M., Arviset, C., et al. 2019, in ASP Conf. Ser. 521, Astronomical Data Analysis Software and Systems XXVI, ed. M. Molinaro, K. Shortridge, & F. Pasian (San Francisco, CA: ASP), 104

Sharma, S., Bland-Hawthorn, J., Johnston, K. V., & Binney, J. 2011, ApJ, 730, 3

Skilling, J. 2004, in AIP Conf. Proc. 735, Bayesian Inference and Maximum Entropy Methods in Science and Engineering: 24th International Workshop on Bayesian Inference and Maximum Entropy Methods in Science and Engineering, ed. R. Fischer, R. Preuss, & U. V. Toussaint (Melville, NY: AIP), 395

Skowron, J., Udalski, A., Kozłowski, S., et al. 2016, AcA, 66, 1

Speagle, J. S. 2020, MNRAS, 493, 3132

Spergel, D., Gehrels, N., Baltay, C., et al. 2015, arXiv:1503.03757

Sumi, T. 2008, in Proc. of Science 054, The Manchester Microlensing Conf., ed. E. Kerins et al. (Trieste: SISSA), 25

Thompson, T. A., Kochanek, C. S., Stanek, K. Z., et al. 2019, Sci, 366, 637

Udalski, A., Szymański, M. K., & Szymański, G. 2015, AcA, 65, 1

van der Walt, S., Colbert, S. C., & Varoquaux, G. 2011, CSE, 13, 22

van Leeuwen, F., de Bruijne, J., Babusiaux, C., et al. 2021, Gaia EDR3 Documentation, (European Space Agency), https://gea.esac.esa.int/archive/documentation/GEDR3/index.html

Virtanen, P., Gommers, R., Oliphant, T. E., et al. 2020, NatMe, 17, 261

Walker, M. A. 1995, ApJ, 453, 37

Wang, Y. H. 1993, Statistica Sinica, 3, 295

WFIRST Astrometry Working Group, Sanderson, R. E., Bellini, A., et al. 2019, JATIS, 5, 044005

Wiktorowicz, G., Lu, Y., Wyrzykowski, Ł., et al. 2020, ApJ, 905, 134

Wozniak, P. R. 2000, AcA, 50, 421

Wyrzykowski, Ł., Kostrzewa-Rutkowska, Z., Skowron, J., et al. 2016, MNRAS, 458, 3012

Yalinewich, A., Beniamini, P., Hotokezaka, K., & Zhu, W. 2018, MNRAS, 481, 930

Yamaguchi, M. S., Kawanaka, N., Bulik, T., & Piran, T. 2018, ApJ, 861, 21

Zurlo, A., Gratton, R., Mesa, D., et al. 2018, MNRAS, 480, 236